Temporal Characterization of SASE FEL pulses at FLASH

Dissertation
zur Erlangung des Doktorgrades
an der Fakultät für Mathematik, Informatik und Naturwissenschaften
Fachbereich Physik
der Universität Hamburg

vorgelegt von
Mahdi Mohammadi Bidhendi

Hamburg
2025

Gutachter/innen der Dissertation:	Dr. Ulrike Frühling Priv.-Doz. Dr. Tim Laarmann
Zusammensetzung der Prüfungskommission:	Dr. Ulrike Frühling Priv.-Doz. Dr. Tim Laarmann Prof. Dr. Tais Gorkhover Prof. Dr. Markus Ilchen Prof. Dr. Daniela Pfannkuche
Vorsitzende der Prüfungskommission:	Prof. Dr. Daniela Pfannkuche
Datum der Disputation:	15.07.2025
Vorsitzender des Fach-Promotionsausschusses PHYSIK:	Prof. Dr. Wolfgang J. Parak
Leiter des Fachbereichs PHYSIK:	Prof. Dr. Markus Drescher
Dekan der Fakultät MIN:	Prof. Dr.-Ing. Norbert Ritter

Abstract

At Free-Electron Lasers (FELs) based on Self-Amplified Spontaneous Emission (SASE), the radiation properties such as pulse duration, arrival time, energy and spectrum fluctuate from shot to shot. To accurately interpret the experimental data on a single-shot basis, dedicated diagnostic tools for each parameter are essential. One such technique is terahertz (THz) streaking, which enables single-shot characterization of the temporal properties of SASE FEL pulses. This thesis presents the design, implementation, and experimental validation of the FL21 beamline, a dedicated photon diagnostics beamline at the Free-electron LASer in Hamburg (FLASH) for extreme ultraviolet (XUV) pulse characterization using THz streaking. The results confirm the feasibility of using this setup for systematic long-term studies of SASE FEL pulse properties with high temporal resolution.

Another key focus of this work is the measurement and characterization of a possible frequency chirp of SASE XUV pulses, frequency chirp refers to a variation in frequency along the pulse. Using two independent methods, THz streaking, which directly measures the linear frequency chirp, and electron bunch energy observation through a transverse deflecting structure (PolariX TDS), a good agreement between both approaches was demonstrated across various FEL settings. By comparing XUV pulse profiles reconstructed from PolariX TDS and THz streaking, the strengths and limitations of each approach in the determination of the pulse shape were identified. The complementary nature of these techniques enables more accurate pulse characterization, particularly in complex phase space scenarios.

A comprehensive investigation of the fundamental and third harmonic FEL radiation properties throughout the amplification process was conducted using experimental measurements and FEL simulations. Variations in pulse duration, energy, and shot-to-shot fluctuations across different wavelengths were examined. The experimental results exhibit good agreement with the chirped three-dimensional time-dependent FEL simulation, confirming the existence of frequency chirp in FEL pulses. These insights enhance our understanding of the properties of FEL fundamental and harmonic radiation, paving the way for future FEL experiments.

Kurzbeschreibung

Bei Freie-Elektronen-Lasern (FELs), die auf selbstverstärkter spontaner Emission (SASE) basieren, schwanken die Strahlungseigenschaften wie Pulsdauer, Ankunftszeit, Energie und Spektrum von Puls zu Puls. Um experimentelle Daten auf Einzelpulsbasis präzise auszuwerten, sind spezialisierte Diagnosetools für jeden dieser Parameter unerlässlich. Hierfür eignet sich zum Beispiel das Terahertz (THz) Streaking, das eine Einzelpuls-Charakterisierung der zeitlichen Eigenschaften von SASE-FEL-Pulsen ermöglicht. Diese Arbeit stellt das Design, die Implementierung und die experimentelle Validierung der FL21-Beamline vor – einer speziellen Photonen-Diagnosestrahllinie am Freie-Elektronen-Laser in Hamburg (FLASH) zur Charakterisierung von extrem-ultravioletten (XUV) Pulsen mittels THz-Streaking. Unsere Ergebnisse bestätigen die Nützlichkeit dieses Aufbaus für systematische Langzeitstudien der SASE-FEL-Pulseigenschaften mit hoher zeitlicher Auflösung.

Ein weiterer zentraler Fokus dieser Arbeit ist die Messung und Charakterisierung eines möglichen Frequenz-Chirps der SASE-XUV-Pulse. Der Frequenz-Chirp bezeichnet eine Veränderung der Frequenz während des Pulses. Mithilfe zweier unabhängiger Methoden – THz-Streaking, das den Frequenzchirp direkt misst, und der Beobachtung der Elektronenenergie durch eine transversale Ablenkstruktur (PolariX TDS) – konnte eine starke Übereinstimmung beider Ansätze über verschiedene FEL-Einstellungen hinweg nachgewiesen werden. Durch den Vergleich der aus PolariX TDS und THz-Streaking rekonstruierten XUV-Pulsprofile wurden die Stärken und Einschränkungen der jeweiligen Methoden zur Pulsformbestimmung identifiziert. Die komplementäre Natur dieser Techniken ermöglicht eine genauere Charakterisierung der Pulse, insbesondere in komplexen Phasenraumszenarien.

Eine umfassende Untersuchung der fundamentalen und dritten harmonischen FEL-Strahlungseigenschaften während des Verstärkungsprozesses wurde anhand experimenteller Messungen und FEL-Simulationen durchgeführt. Variationen in Pulsdauer, Energie und Puls-zu-Puls-Fluktuationen über verschiedene Wellenlängen hinweg wurden analysiert. Unsere experimentellen Ergebnisse zeigen eine gute Übereinstimmung mit einer gechirpten dreidimensionalen zeitabhängigen FEL-Simulation und bestätigen das Vorhandensein eines Frequenzchirps in den FEL-Pulsen. Diese Erkenntnisse verbessern das Verständnis der Eigenschaften von fundamentaler und harmonischer FEL-Strahlung und ebnen den Weg für zukünftige FEL-Experimente.

Publications

The following publications are presented in chronological order as part of this cumulative thesis. My contributions to each are detailed below.

- A.1 **FEL Pulse Duration Evolution along Undulators at FLASH**, Applied Sciences, 12(14), 7048 (2022).

  Contributions: I conducted the experiment in collaboration with a team of researchers, contributing to its execution and data acquisition. Under the supervision of S. Düsterer, I analyzed the pulse duration data and compared it with the simulation provided by M. Yurkov. I was responsible for preparing the manuscript and coordinating the review process.

- A.2 **Free-electron laser temporal diagnostic beamline FL21 at FLASH**, Optics Express, 31(12), 19146–19158 (2023).

  Contributions: I conducted the experiment in collaboration with a team of researchers, contributing to its execution and data acquisition. I analyzed the cutting mirror measurements under the supervision of S. Düsterer. I was a main contributor to the manuscript preparation process, including writing, reviewing and submission.

- A.3 **Determination of the XUV frequency chirp at the free-electron laser FLASH by THz streaking and electron beam diagnostic**, Photonics 11, 1153 (2024).

  Contributions: I conducted the experiment in collaboration with a team of researchers, contributing to its execution and data acquisition. I analyzed the chirp measurement data and contributed to the overall data analysis under the supervision of S. Düsterer. I prepared the manuscript and coordinated the review and submission process.

- A.4 **Characterization of free-electron laser third harmonic radiation at FLASH**, Optics Express (2025).

  Contributions: I conducted the experiment in collaboration with a team of researchers, contributing to its execution and data acquisition. Under the supervision of S. Düsterer, I analyzed the harmonic measurement data and compared it with the simulation provided by M. Yurkov. I prepared the manuscript and coordinated the review and submission process.

- A.5 **Single-shot temporal characterization with the transverse deflecting structure PolariX and THz streaking at FLASH**, SRI proceedings (2025).

  Contributions: I participated in the experiment, contributing to its execution and data collection. I was involved in the manuscript review process.

To the Ongoing Battle for Women, Life, Freedom

Table of Contents

Chapter 1

Introduction

In the mid-1970s, John Madey and his colleagues pioneered the development of the first Free-Electron Laser (FEL) operating in the infrared spectrum [1]. Since this groundbreaking achievement, FELs have become transformative tools in the generation of high-intensity, short-wavelength light, enabling advancements across numerous scientific fields. The establishment of the first soft X-ray FEL in Hamburg, known as FLASH [2], in 2005, marked the beginning of a global expansion in soft and hard X-ray FEL facilities, including LCLS [3], SCSS [4], SACLA [5], FERMI [6], European XFEL [7], SwissFEL [8], PAL-XFEL [9], and SXFEL [10].

X-ray FEL facilities have revolutionized the study of light-matter interactions, providing unprecedented insights into ultrafast processes in atoms [11, 12], molecules [13–15], clusters [16–18], and nanoparticles [19]. These capabilities extend to non-linear spectroscopy [20, 21] and single-shot imaging of individual particles [22], and investigations of ultrafast dynamics in solid-state targets [23], enabling novel insights into the dynamics of matter on extremely short timescales. The advancements in these areas have revolutionized our understanding of fundamental processes across a wide range of scientific fields.

Currently, most X-ray FELs operate based on self-amplified spontaneous emission (SASE). FLASH as a SASE FEL is operated by amplifying spontaneous emission from electron bunches traveling through an undulator, a series of magnets that cause the electrons to oscillate and emit radiation. Seeded FELs use either an external laser to initiate the emission process [24] or employ internal monochromators or filters to refine the spectral bandwidth of the SASE output (known as self-seeding [25]). Unlike seeded

and self-seeded FEL, the SASE FEL relies entirely on the intrinsic properties of the electron bunches for amplification. As a result, it generates a highly intense yet fluctuating output, with shot-to-shot variability caused by the randomness of the initial spontaneous emission [26, 27]. FLASH exemplifies these characteristics, making it both a powerful and complex tool for experiments. Its fluctuating nature presents challenges for precise measurements but also enables unique studies of ultrafast dynamics.

The precise temporal characterization of SASE FEL pulses is crucial for optimizing FEL performance and ensuring the reliability of experimental results. Various techniques have been developed to characterize the temporal properties of SASE FEL pulses, including electron bunch and photon pulse characterization techniques [28]. For electron bunch diagnostics, notable methods include the Transverse Deflecting RF Structure (TDS) [29, 30], bunch shape reconstruction by terahertz spectroscopy [31, 32], and bunch compression monitors [33]. For photon pulse duration measurement, techniques such as extreme ultraviolet (XUV) autocorrelation in the gas phase [34, 35], autocorrelation in semiconductors [36–38], cross-correlation with terahertz pulses [39–41], and angular streaking [42, 43] are commonly used. The terahertz streaking technique was implemented for the temporal characterization of XUV pulses at FLASH first with undulator-based THz [39] and later on with laser-based THz [44]. In addition, as a complementary diagnostic, an X-Band Transverse Deflection Structure (PolariX TDS) has also been installed at FLASH2 for electron bunch diagnostics. Positioned downstream of the undulators, PolariX TDS allows both the characterization of electron bunch properties and the study of the SASE process in electron bunches.

This thesis focuses on the temporal characterization of SASE FEL pulses at FLASH using the THz streaking and PolariX TDS. The following chapter will provide a detailed theoretical background on SASE FEL pulse generation and the THz streaking technique. In chapter 3, technical details of the beamline dedicated to photon diagnostics at FLASH, and the experimental setup of the THz streaking and PolariX TDS are explained. The results of the temporal characterization studies are shown in chapter 4. Chapter 5 concludes the scientific results presented in this PhD thesis and provides an outlook for possible future studies.

Chapter 2

Theoritical Background

FELs are advanced light sources that can deliver coherent radiation across a wide range of wavelengths, including XUV and X-ray regions. This chapter presents an overview of the fundamental principles of SASE FELs and the THz streaking technique used for characterizing SASE FEL pulses.

2.1 Free-Electron Lasers

Unlike conventional lasers that rely on atomic or molecular transitions, FELs generate radiation by sending the accelerated electrons through a magnetic structure known as an undulator, which consists of a periodic arrangement of dipole magnets with alternating polarity. This process causes the electrons to oscillate and emit radiation. In the XUV and X-ray regime, where high-reflective optics are unavailable, high-gain FELs are the only solution. In this scheme, amplification occurs in a single pass through a long undulator or a series of shorter undulators. Self-Amplified Spontaneous Emission (SASE) and external seeding are two prominent approaches for high-gain FELs. Most FELs worldwide rely on the SASE process to produce radiation [45, 46]. In the next chapter, the theory of the SASE process and its characteristics are explained.

2.1.1 Self-Amplified Spontaneous Emission (SASE)

In a SASE FEL, a relativistic electron beam is sent through an undulator, a periodic magnetic structure that forces the electrons into oscillatory motion, as shown in Fig. 2.1. As a result, the electrons emit spontaneous radiation at a resonant wavelength. Initially, this radiation is weak and incoherent, but as the electrons continue traveling through

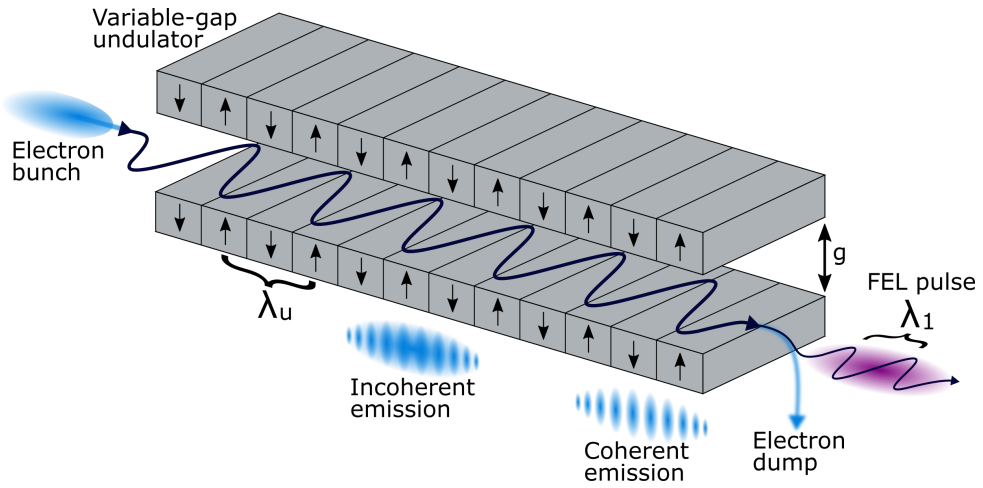

Figure 2.1: Schematic of a planar variable-gap undulator. The electron bunch enters the undulator from the left and oscillates due to the periodic magnetic field of the undulator with a period λ_u. As the electron bunch travels through the undulator, microbunches begin to form, achieving coherence and emitting radiation at the resonant wavelength λ_r. g denotes the undulator gap. Adjusting the gap modifies the magnetic field strength, which in turn alters the radiation wavelength. Figure adapted from [47].

the undulator, they interact with the copropagating radiation field. Depending on the relative phase between the electron bunch and the light wave, the electrons lose energy to the light wave or gain energy from it. The electrons that gain energy from the field are more rigid to the undulator's magnetic field than those losing energy to the field, leading to a modulation in their longitudinal velocity. This, in turn, results in periodic density modulations with a periodicity of one resonant wavelength. These structures are called microbunches [47].

As the electron bunch travels through the first few undulator modules, microbunching develops within the beam, causing the electrons to radiate coherently. This coherent emission leads to an exponential increase in the radiation power. Therefore, this phase is referred to as the exponential gain regime or the so-called linear regime, as the radiation power grows exponentially and is represented as linear when plotted on a logarithmic scale, as shown in Fig. 2.2. A higher degree of microbunching within the electron bunch enhances the coherence of the emitted radiation. The process continues until the radiation intensity and microbunching reach saturation, marking the onset of the saturation regime [47]. At this stage, the electron beam's energy depletion and the growing slippage between the radiation and the electron bunch constrain further amplification. Achieving strong microbunching and efficient amplification requires precise control of the electron bunch

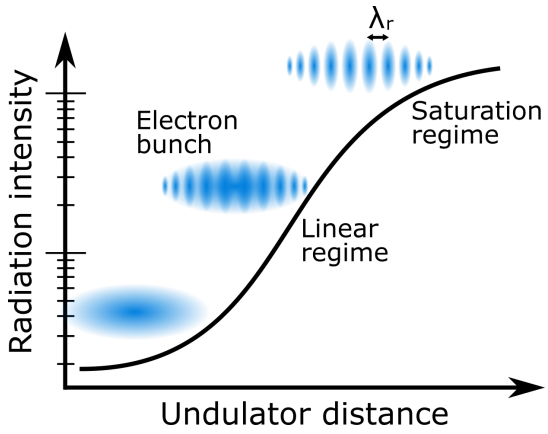

Figure 2.2: Schematic illustration showing the progression of the average SASE FEL radiation intensity (log. scale), as it amplifies along the undulator. The interaction between the electron bunch and the electromagnetic wave induces periodic modulations in longitudinal density at the resonant wavelength λ_r. The microbunching process is illustrated at three positions along the undulator. The coherent emission of electrons within the same microbunch and the coherence between different microbunches lead to the exponential growth of radiation power in the linear regime. As the FEL process progresses towards the end of the undulator, saturation is reached. Figure adapted from [2].

and extended interaction regions, which is why XUV and X-ray FEL facilities employ long linear accelerators (LINACs). For the theoretical description presented here, a one-dimensional (1D) FEL model is used, which assumes the amplification of a plane wave by an infinitely wide electron beam with no energy chirp [48].

For fundamental radiation, the amplification process originates from shot noise in the electron beam. When an electron beam enters the undulator, its radiation has both longitudinal and transverse modes. The number of longitudinal modes is determined by fluctuations in the radiation pulse energy filtered through a pinhole and decreases during the amplification process as temporal coherence improves. As the beam propagates, the transverse mode selection process occurs, and fluctuations in radiation energy begin to grow. The number of modes represents the total count of both longitudinal and transverse modes present in the radiation pulse. The electrons traveling through a planar undulator experience a magnetic field aligned in the vertical y-direction. The field strength varies sinusoidally along the propagation direction (z-direction) as follows [47, 49]:

$$B_y(z) = B_0 \sin\left(\frac{2\pi}{\lambda_u} z\right), \tag{2.1}$$

where B_0 is the magnetic pole field, and λ_u is the period of the magnetic arrangement of

the undulator. When a relativistic electron enters the undulator, it undergoes periodic oscillations in the horizontal x-direction, causing it to emit spontaneous radiation at the resonance wavelength:

$$\lambda_r = \frac{\lambda_u}{2\gamma_0^2}\Big(1 + \frac{K_0^2}{2}\Big), \tag{2.2}$$

where

$$K_0 = \frac{eB_0\lambda_u}{2\pi m_e c} \tag{2.3}$$

is the dimensionless undulator strength parameter, γ_0 is the electron energy in units of the rest energy mc^2, m_e is the electron mass, and c is the speed of light in vacuum. Eq. 2.2 shows that the wavelength of the emitted radiation can be adjusted by modifying either the energy of the electron bunch or the magnetic field strength, particularly in the case of a variable-gap undulator configuration.

The electromagnetic wave traveling forward co-propagates with the electron bunch, allowing for energy exchange between the two. In the undulator, the co-propagating radiation overtakes the electrons by a distance of λ_1 per undulator period, where

$$\lambda_1 = \lambda_r(\Phi = 0) = \frac{\lambda_u}{2\gamma_0^2}\Big(1 + \frac{K_0^2}{2}\Big) = \frac{2\pi c}{\omega_1} \tag{2.4}$$

is the resonant wavelength in the forward direction, ω_1 is the fundamental undulator frequency. The radiation in the forward direction also contains higher harmonics with the wavelengths

$$\lambda_m = \frac{\lambda_1}{m}, \quad m = 1, 2, 3, ... \tag{2.5}$$

Due to the periodic nature of the system, a sustained interaction with the radiation field is established. The relative phase between the electrons and the plane wave determines whether the electrons gain or lose energy from the radiation field. Consequently, microbunches form as the energy distribution of the electron bunch becomes periodically modulated at the resonant wavelength λ_r. Microbunching amplifies the initial spontaneous emission, leading to an exponential growth of radiation intensity and the formation of highly intense photon pulses. Based on the 1D FEL model, the distance over which the radiation power grows by a factor of e in the linear regime is described by the power gain length [47, 50]:

$$L_g \approx \frac{\lambda_u}{4\pi\sqrt{3}\rho}, \tag{2.6}$$

where ρ is the dimensionless FEL Pierce parameter and is on the order of $10^{-4} - 10^{-3}$ for X-ray FELs. The emitted power grows exponentially with the undulator length z:

$$P(z) \propto exp\left(\frac{z}{L_G}\right). \tag{2.7}$$

This rapid growth persists until the electron beam's energy is sufficiently depleted, causing the radiation power to reach its maximum in the saturation regime

$$P_{sat} = \rho I_e \frac{W}{e}, \tag{2.8}$$

where I_e is the bunch peak current and W is the relativistic electron energy. The distance at which the saturation regime begins is called the saturation length. The saturation power is reached at the saturation length z_{sat}:

$$z_{sat} \simeq \frac{\lambda_u}{4\pi\rho}\left(3 + \frac{\ln N_c}{\sqrt{3}}\right) \tag{2.9}$$

where N_c is the number of cooperating electrons.

SASE FEL pulses consist of individual, independent intensity spikes (also referred to as longitudinal modes) that are temporally coherent. Their positions and peak heights vary from pulse to pulse, with each spike having a duration determined by the coherence time. The coherence time quantifies the temporal range over which the electrons radiate coherently. In the 1D model, the coherence time at saturation can be written as

$$\tau_c \simeq \frac{1}{\rho\omega}\sqrt{\frac{\pi \ln N_c}{18}}, \tag{2.10}$$

where ω is the radiation frequency. The coherence time increases at a rate of $\sqrt{z}$ in the linear regime, reaches a maximum value just before saturation, and then drops drastically [48, 51, 52]. A practical estimate for the coherence time can be made based on the observation that in SASE FELs operating in the XUV and X-ray wavelength range, saturation is typically reached after approximately 10 field gain lengths. The field gain length is a key parameter in FEL optimization, providing a reliable estimate of the undulator length required to achieve saturation [53]. Thus, the coherence time τ_c relates to the saturation length as:

$$\tau_c \simeq \lambda z_{sat}/(2\sqrt{\pi} c \lambda_u). \tag{2.11}$$

The duration of the radiation pulse is mainly determined by the length of the lasing fraction of the electron bunch. At the start of the amplification process, the shape of

the radiation pulse follows the longitudinal current profile of the electron bunch. In the exponential high-gain regime, power amplification and beam bunching are more pronounced for regions of higher current, leading to a reduction in the duration of the radiation pulse as the electron bunch propagates through the undulator. For the number of modes $M \gtrsim 2$, the root mean square (rms) electron pulse length τ_{el} and the minimum radiation pulse length τ_{ph}^{min} in full width at half maximum (FWHM) at the end of the exponential gain regime are given by [54]:

$$\tau_{ph}^{min} \simeq \tau_{el} \simeq \frac{M\lambda}{5\rho} \simeq \frac{M\lambda z_{sat}}{5c\lambda_W}. \tag{2.12}$$

As the amplification approaches saturation, the tails of the electron bunch increasingly contribute to the radiation power. Beam bunching continues to grow, leading to an overall increase in radiation pulse duration. The contribution of the tail to the lasing results in the same relative radiation pulse lengthening. At the saturation point, the pulse duration from a non-chirped electron bunch is about 1.4 longer than the minimum pulse for the linear regime given by Eq. 2.12, and it increases further up to about a factor of 2 in the deep saturation regime.

2.1.2 Radiation Characteristics of SASE FELs

The SASE process relies on the intrinsic properties of the electron bunch. One major characteristic of SASE FELs is the presence of pulse-to-pulse fluctuations in the emitted radiation, which stem from the shot noise in the electron bunch that initiates the FEL process. As the electron bunch travels through the first part of the undulator, it spontaneously emits radiation due to the accelerated motion of electrons in the magnetic field. The spontaneous emission is inherently random and uncorrelated between pulses due to the initial random charge density distribution. This randomness profoundly impacts the radiation characteristics, which are best understood through the principles of statistical optics [52].

The statistical properties of the fundamental radiation follow Gaussian statistics up to the undulator length of $z \simeq 0.75 z_{sat}$, where z_{sat} is the saturation length. Within this range, the probability distribution of the instantaneous radiation pulse energy W follows a negative exponential distribution:

$$p(W) = \frac{1}{\langle W \rangle} \exp\left(-\frac{W}{\langle W \rangle}\right), \tag{2.13}$$

and any integral of the radiation intensity such as radiation power P or radiation pulse energy E, exhibits fluctuations that follow a gamma distribution:

$$p(E) = \frac{M^M}{\Gamma(M)} \left(\frac{E}{\langle E \rangle} \right)^{M-1} \frac{1}{\langle E \rangle} \exp\left(-M \frac{E}{\langle E \rangle} \right), \tag{2.14}$$

where $M = 1/\sigma_E^2$ can be interpreted as the average number of degrees of freedom or modes (longitudinal and transverse) in the radiation pulse, $\sigma_E^2 = \langle (E - \langle E \rangle)^2 \rangle / \langle E \rangle^2$ is the relative dispersion of the radiation energy, and $\Gamma(M)$ is the gamma function [48, 52].

As shown in Eq. 2.5, the radiation also contains higher harmonics. This harmonic content arises from the evolution of the electron beam's density modulation during the amplification process. In the linear regime, the electron beam develops a sinusoidal density modulation at the fundamental wavelength, resulting primarily in fundamental radiation. As the interaction progresses into the nonlinear regime, this modulation becomes increasingly non-sinusoidal, forming sharp microbunches separated by the fundamental wavelength. These narrow bunches contain higher-order Fourier components, which give rise to coherent harmonic emission. The stronger the bunching, the more intense the harmonic content. This microbunching subsequently leads to enhanced nonlinear harmonic growth and can become the dominant mechanism for harmonic generation [55, 56].

The statistical properties of harmonic radiation in a SASE FEL differ significantly from the fundamental. The intensity of a higher harmonic generated through the nonlinear harmonic generation mechanism results from a nonlinear transformation of the fundamental intensity. This transformation for the nth harmonic is given by $z = W^n$. Thus, the negative exponential distribution in Eq. 2.13 transforms to [57, 58]:

$$p(z) = \frac{z}{n\langle W \rangle} z^{(1-n)/n} \exp(-z^{1/n}/\langle W \rangle). \tag{2.15}$$

Due to the symmetry of planar undulators, on-axis radiation at even harmonics is strongly suppressed. This suppression occurs because the contributions of neighboring periods are out of phase, leading to destructive interference [47, 59, 60]. In contrast, odd harmonics can still be efficiently generated. In the nonlinear regime near the saturation point, the probability distributions of the fundamental and the 3rd harmonic change significantly from those in the linear regime. As shown in Fig. 1 b) in A.4, the 3rd harmonic radiation exhibits much noisier behavior at saturation, with instantaneous intensities following a nearly negative exponential distribution, while the fluctuations of the fundamental begin to stabilize. [58].

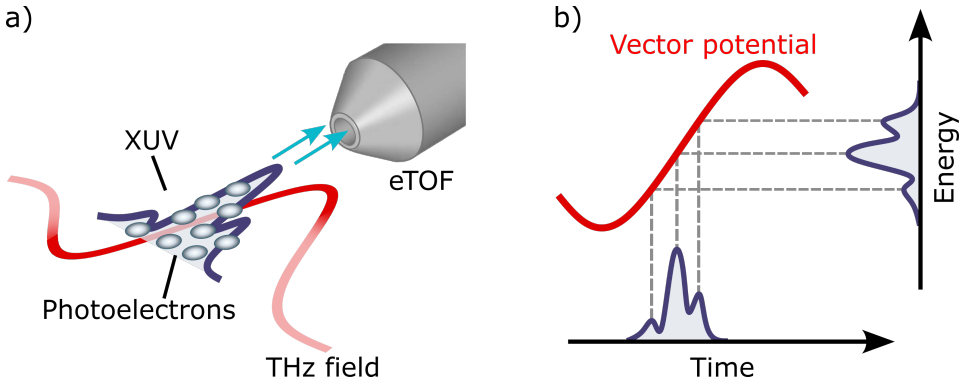

Figure 2.3: a) Schematic representation of the THz streaking method. A noble gas target is photoionized by an XUV pulse, creating photoelectrons with identical temporal structure. The kinetic energy of the photoelectrons is modified by the THz field and then measured by an eTOF. b) The photoemission is probed at the zero-crossing of the THz field's vector potential, where the initial momentum distribution is symmetrically broadened around the central energy, resulting in the maximum broadening of the photoelectron spectrum. Consequently, the vector potential maps the XUV time structure onto changes in electron momentum.

The one-dimensional model provides a framework for studying the ideal mechanism of amplification. It describes the physics of pulse length effects and the temporal properties of the radiation while involving a minimal number of parameters. However, for a more quantitative description of real experiments, a three-dimensional model is required to account for effects such as diffraction and betatron motion. Additionally, the detailed structure of the electron bunch (e.g., energy chirp) can play a crucial role in interpreting experimental results. Therefore, the analysis of short pulse effects is extended using three-dimensional, time-dependent simulations performed with the FAST code [48, 56, 61].

2.2 Terahertz Streaking Spectroscopy

Among various methods available for characterizing XUV FEL pulses, streaking spectroscopy has been selected as the preferred approach for the temporal characterization of SASE FEL pulses at FLASH [62, 63]. The streaking method has been a crucial technique for time-resolved measurements in the attosecond regime, where it was first developed to study the dynamics of ultrashort light pulses [64, 65]. Streaking techniques were later adapted for FELs, where the streaking wavelength was extended by over an order of magnitude, making them essential for characterizing the temporal structure of SASE FEL pulses. The streaking method relies on the interaction between photoelectrons generated

by an ultrashort photon pulse and a rapidly changing electromagnetic field. One key requirement for this method is that the oscillation period of the streaking field must be significantly longer than the photon pulse being measured.

In the case of FLASH, which generates pulses from a few fs to $\sim$ 300 fs, the streaking field must have periods corresponding to frequencies in the terahertz (THz) range to fulfill this condition. By utilizing a THz field with the appropriate frequency range, it becomes possible to accurately map the temporal structure of the XUV pulses onto the energy distribution of the photoelectrons.

In the THz streaking technique, illustrated in Fig. 2.3 a), the process begins with the interaction of the XUV pulse with noble gas atoms, producing an electron wavepacket that contains the temporal characteristics of the original XUV pulse. The kinetic energy of these photoelectrons is then modulated by a co-propagating THz field, creating a "streaked" energy spectrum that encodes the temporal structure of the XUV pulse. In this process, the vector potential of the THz field directly maps the temporal structure of the XUV pulse onto the energy modulation of the photoelectrons, as illustrated in Fig. 2.3 b). The kinetic energy of the streaked photoelectrons is then measured by an electron time-of-flight (eTOF) spectrometer, which determines the electron energy based on their flight time to the detector. This enables the extraction of the temporal information embedded in the photoelectron spectrum.

To better understand the underlying principles of the streaking process, a classical description is often employed. The following section explains the classical description of the streaking process, detailing the modification of photoelectron kinetic energy by the THz field, the relationship between the THz vector potential and energy shifts, and how these measurements enable a precise temporal reconstruction of the XUV pulse.

2.2.1 Classical Description

Streaking measurements can be understood through a classical framework describing the photoionization process induced by XUV light in the presence of a strong electromagnetic field [66]. In the streaking process, the XUV pulse hits the atoms of a noble gas, causing ionization and releasing photoelectrons. The ejected photoelectrons are then accelerated by the streaking field. The kinetic energy of the emitted photoelectrons can be written as follows

$$W_0 = \frac{m_e v_0^2}{2} = \hbar\omega_{XUV} - E_I, \tag{2.16}$$

where m_e is the electron mass, v_0 is the electron's initial velocity at the instant of ionization, $\hbar = \frac{h}{2\pi}$ is the reduced Planck constant, ω_{XUV} is the angular frequency of the incoming XUV pulse, and E_I is the ionization energy.

The fundamental principles describing the behavior of electrons emitted from free atoms under short soft X-ray pulses and an intense, linearly polarized light field have been developed for attosecond metrology [66]. The mathematical description remains unchanged when using a THz field as the streaking field. The electric field of the streaking field is

$$E_{\mathrm{THz}} = E_0(t)\cos\left(\omega_{\mathrm{THz}}t + \phi\right) \tag{2.17}$$

where t represents time, $E_0(t)$ is the time-dependent amplitude of the THz pulse, ω_{THz} is the angular frequency of the THz pulse, and ϕ is its phase at the moment of ionization. The vector potential of the THz field in the Coulomb gauge can be written as

$$A_{\mathrm{THz}}(t) = \frac{-E_0(t)}{\omega_{\mathrm{THz}}}\sin\left(\omega_{\mathrm{THz}}t + \phi\right). \tag{2.18}$$

The time-dependent momentum of electrons in the THz field can be written as

$$\vec{p}(t) = e\Big[\vec{A}_{\mathrm{THz}}(t_i) - \vec{A}_{\mathrm{THz}}(t)\Big] + m_e\vec{v}_0 \tag{2.19}$$

where e is the electron charge, and $A_{\mathrm{THz}}(t_i)$ is the vector potential of the THz field at the time of ionization t_i. From Eq. 2.19, the momentum change of electrons due to the THz field is given by

$$\Delta\vec{p}(t) = \vec{p}_f - \vec{p}(t_0) = e\vec{A}_{\mathrm{THz}}(t_0). \tag{2.20}$$

To evaluate the temporal resolution, it is convenient to convert Eq. 2.20 into the change of the kinetic energy of electrons in the presence of the THz field [66]:

$$W_{kin} = W_0 + 2U_p\cos(2\theta)sin^2(\Phi_i) \pm \alpha\sqrt{8W_0U_p}cos(\theta)sin(\phi_i), \tag{2.21}$$

where $U_p = \frac{e^2E_0^2(t_i)}{4m_e\omega_{\mathrm{THz}}^2}$ represents the ponderomotive potential of the THz field at the time of ionization, θ is the angle between the THz polarization and the direction along which the electrons are detected, $\alpha = \sqrt{1 - \left(\frac{2U_p}{W_0}\right)sin^2(\theta)sin^2(\Phi_i)}$ is a correction factor that can be approximated as 1 when $U_p \ll W_0$. The last term in Eq. 2.21 is positive unless when $U_p > W_0/2$, where some of the photoelectrons are accelerated in the reverse direction, opposite to $\vec{v}_0$. Under typical condition of $U_p \ll W_0$, the second term can be neglected, simplifying the Eq. 2.21 to the following approximation:

$$W_{kin} \approx W_0 + \alpha\sqrt{8W_0U_p}cos(\theta)sin(\phi_i). \tag{2.22}$$

For an observation angle perpendicular to the THz field polarization direction ($\theta = \phi/2$), where the deflection is maximized, the final kinetic energy is

$$W_{kin\perp} \approx W_0, \tag{2.23}$$

indicating that the final kinetic energy, measured perpendicular to the polarization of the THz field, is approximately equal to the initial unperturbed kinetic energy. For an observation along the polarization plane of the THz field ($\theta = 0$), the final kinetic energy is

$$W_{kin\parallel} \approx W_0 + \sqrt{8W_0U_p}sin(\phi_i). \tag{2.24}$$

At the time of ionization, near the zero-crossing of the vector potential (where $\omega_{\mathrm{THz}}t$ is small), the change in the kinetic energy of the photoelectrons measured along the polarization of the THz pulse can be expressed as

$$\Delta W_{kin\parallel} \approx e\sqrt{\frac{2W_0}{m_e}}\frac{E_0(t_i)}{\omega_{\mathrm{THz}}}sin(\phi_i) \approx -e\sqrt{\frac{2W_0}{m_e}}A_{\mathrm{THz}}(t_i), \tag{2.25}$$

which indicates that

$$\Delta W_{kin\parallel} \propto -A_{\mathrm{THz}}(t_i). \tag{2.26}$$

Therefore, the magnitude of the change in kinetic energy measured parallel to the polarization plane of the streaking field is directly proportional to the THz vector potential at the time of ionization. This enables the measured kinetic energies to be directly mapped onto the time domain, allowing for a precise temporal reconstruction of the XUV pulse, as detailed in the next section.

2.2.2 Reconstruction of FEL Pulses

To reconstruct the temporal profile of FEL pulses, we assume the pulse has a Gaussian shape in the time domain and its frequency remains constant along the pulse (no chirp). For such a Gaussian XUV pulse we can determine the pulse duration analytically. The electric field of a Fourier-limited XUV pulse with a Gaussian pulse envelope can be expressed as [66]:

$$E_{XUV}(t) = E_0e^{-at^2}e^{i(\omega_0t)}, \tag{2.27}$$

where E_0 is the amplitude of the pulse envelope, a is related to the rms duration of the pulse ($\tau_{XUV} = \frac{1}{2\sqrt{a}}$), and ω_0 is the central (carrier) angular frequency of the pulse. The spectral bandwidth of the streaked pulse can be written as [63]:

$$\sigma_{streak} = \sqrt{\sigma_{0,XUV}^2 + s^2\tau_{XUV}^2}, \tag{2.28}$$

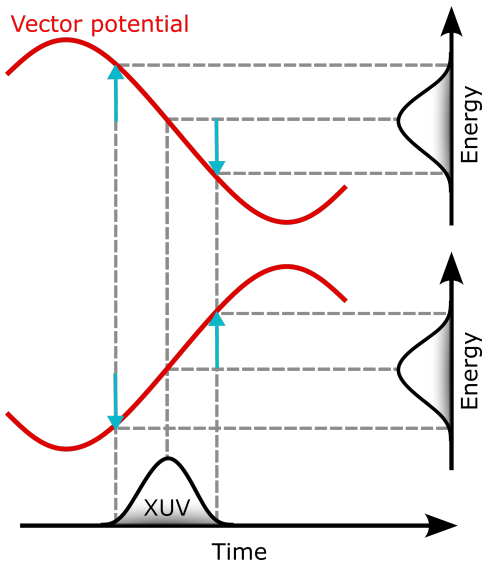

Figure 2.4: A schematic illustration of the streaking process for photoelectrons released through the photoionization of a noble gas by an XUV pulse. The red curves represent the vector potential of the streaking field that is temporally and spatially overlapped with the XUV pulse. The streaked spectrum of the photoelectrons is plotted on the vertical axis. In the upper panel, photoelectrons are streaked with the negative slope of the vector potential, while in the lower panel, they are streaked with the opposite sign. The measured spectra on the vertical axis show identical spectral broadening and are symmetrically distributed around the initial central energy, leading to the maximum broadening of the photoelectron spectrum on both sides of the streaking field.

where $s = \partial W_{kin\parallel}/\partial t$, known as the streaking speed, is determined by the slope of the linear part of the vector potential around the zero-crossing. The streaking speed links the XUV pulse's temporal structure to the photoelectron energy modulation. To determine the XUV pulse duration τ_{XUV} from Eq. 2.28, it is necessary to measure the unstreaked width $\sigma_{0,XUV}$ as it represents the instrument function, along with the streaked widths σ_{streak}. With these measurements, resulting equation can be solved to extract the pulse duration as below:

$$\tau_{XUV} = \frac{\sqrt{\sigma_{streak}^2 - \sigma_0^2}}{s}. \tag{2.29}$$

Figure 2.4 illustrates how the temporal information of the XUV pulse is mapped onto the kinetic energy of photoelectrons. This mapping principle also enables the reconstruction of FEL pulses with a linear chirp, as explained in the following section.

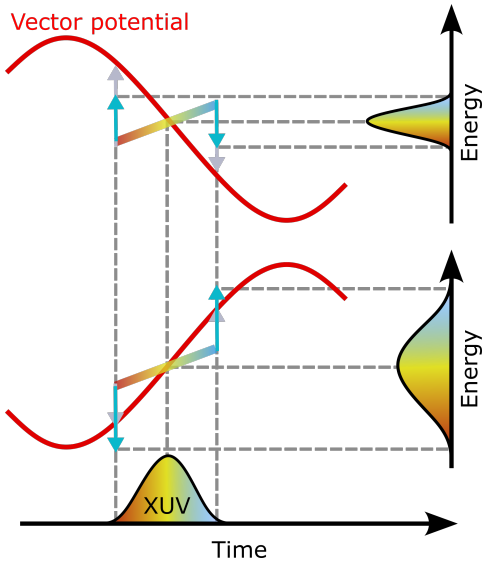

Figure 2.5: Schematic illustration of the streaking process for a linearly chirped pulse. A negatively chirped pulse is streaked by the vector potential of the THz field, modifying the kinetic energy of the photoelectrons, which is then measured by two eTOFs. The blue arrows indicate the energy upshift and downshift of chirped photoelectrons due to their interaction with the vector potential, while the gray arrows represent the corresponding shifts for a non-chirped pulse. The broadening of the photoelectron spectrum measured by each eTOF depends on the direction of the streaking field. In the lower case, higher-energy electrons at the head of the XUV pulse are further accelerated, while lower-energy electrons at the tail of the pulse are decelerated, resulting in a broader streaked spectrum. In the upper case, the opposite occurs, resulting in a narrower streaked spectrum. The linear chirp can then be determined by analyzing the difference between the two measured spectra. Figure adapted from [67].

2.2.3 Reconstruction of Linearly Chriped FEL Pulses

Chirp refers to the variation of a pulse's instantaneous frequency over time. To accurately reconstruct the temporal profile of FEL pulses with frequency chirp, we assume a constant linear chirp in the XUV pulse and neglect higher-order contributions. A linear chirp means that the frequency components of the pulse change linearly over time, causing different parts to have different frequencies.

In an XUV pulse with a negative chirp as shown in Fig. 2.5, higher frequencies appear earlier, while in a positively chirped pulse, higher frequencies appear later. This linear frequency modulation can be expressed analytically. For a Gaussian XUV pulse with linear chirp, the electric field can be expressed as [68]:

$$E_{XUV}(t) = E_0 e^{-at^2} e^{i\Phi(t)}, \quad \text{where} \quad \Phi(t) = \omega_0 t + c_\phi t^2, \tag{2.30}$$

and c_ϕ is the linear chirp parameter that describes the linear variation of the instantaneous frequency. The instantaneous frequency is given by $\frac{d\Phi(t)}{dt} = \omega_0 + 2c_\phi t$. Therefore, the change of instantaneous energy chirp c_E is given by $E = E_0 + c_E t$, where $c_E = 2c_\phi$. The pulse duration can be analytically estimated from the measured up-streaked as well as down-streaked, and non-streaked spectra [39, 40]. The spectral bandwidth of the streaked pulse can be written as

$$\sigma_\pm = \sqrt{\sigma_{0,XUV}^2 + \tau_{XUV}^2(s_\pm^2 \pm 4c_\phi s_\pm)}. \tag{2.31}$$

The sign $\pm$ is determined by the slope of the vector potential of the streaking field A_{THz}. This sign depends on the direction from which the streaking is observed. To determine the XUV pulse duration τ_{XUV} and chirp c_E from Eq. 2.31, it is necessary to measure the unstreaked width $\sigma_{0,XUV}$ along with the streaked widths $\sigma_\pm$ for both sides of the vector potential. Due to the presence of linear chirp, the spectral broadening differs between the up-streaked and down-streaked spectra. With these measurements, the two resulting equations can be solved to simultaneously extract the pulse duration and chirp as below [68, 69]:

$$\tau_{XUV} = \sqrt{\frac{(\sigma_+^2 - \sigma_0^2)s_- + (\sigma_-^2 - \sigma_0^2)s_+}{(s_+ + s_-)s_+ s_-}}, \tag{2.32}$$

$$c_\phi = \frac{(\sigma_+^2 - \sigma_0^2)s_-^2 - (\sigma_-^2 - \sigma_0^2)s_+^2}{4s_+ s_-(s_+ + s_-)\tau_{XUV}^2}. \tag{2.33}$$

Since $c_E = 2c_\phi$, from Eq. 2.33, the energy chirp is given by

$$c_E = \frac{(\sigma_+^2 - \sigma_0^2)s_-^2 - (\sigma_-^2 - \sigma_0^2)s_+^2}{2s_+ s_-(s_+ + s_-)\tau_{XUV}^2}. \tag{2.34}$$

A detailed explanation of the measurement process is provided in the next chapter.

Chapter 3

Experimental Setup

This chapter provides an overview of the experimental infrastructure and techniques employed in this thesis. First, the technical details of FLASH are presented, including the diagnostic beamline (FL21) used to characterize the properties of SASE XUV pulses. Then the THz streaking setup is introduced, which facilitates precise temporal measurements of XUV pulses by analyzing the photoelectron energy spectrum in the presence of a THz field. Finally, the PolariX transverse deflecting structure setup is presented, a crucial tool for electron beam diagnostics.

3.1 Free-Electron Laser in Hamburg (FLASH)

The Free-Electron LASer in Hamburg (FLASH) began operation in 2005, marking a significant advancement in the development of high-intensity, XUV and soft X-ray radiation sources [2]. FLASH is a SASE FEL that produces XUV radiation during a single pass of an electron beam through a long undulator. It provides an exceptionally bright and ultrashort source of coherent XUV light. FLASH with a peak brilliance of up to 10^{30} photons/(s mrad^2 mm^2) per 0.1 % bandwidth, exceeds the capabilities of 3rd generation synchrotron light sources by several orders of magnitude in terms of peak brilliance [2, 70, 71].

In 2014, FLASH was upgraded to support two parallel FEL lines, expanding its operational capacity. Alongside the original FLASH1 undulator system, which consists of six undulators with a 27 mm period, a peak magnetic field of 0.47 T, and a fixed gap of 12 mm, a second undulator line called FLASH2 was commissioned in a separate

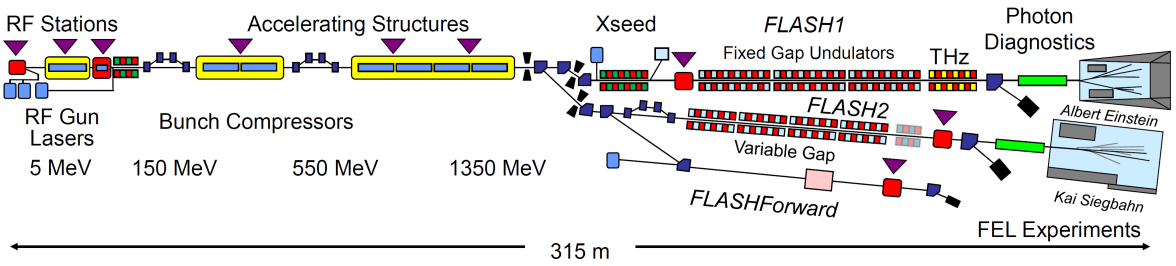

Figure 3.1: Schematic layout of FLASH facility. From left to right: injector laser, linear accelerator (LINAC), undulator and experimental halls of FLASH1 and FLASH2. The electron bunch is generated via the injector laser and then accelerated to relativistic energies. The accelerated electron bunch train is then split and sent to FLASH1 and FLASH2 undulators where photon pulses are generated. Figure from [82].

tunnel [72]. FLASH2 is equipped with twelve variable-gap undulators with a period of 31 mm, providing greater flexibility in wavelength tuning. This upgrade also included a new experimental hall that currently hosts three user endstations. With this upgrade, FLASH transformed into a multi-user facility, allowing for the simultaneous operation of both FEL beams and almost doubling its user capacity [72–75].

As illustrated in Fig. 3.1, the electrons are generated via the photoelectric effect as the injector laser hits the Cs_2Te cathode [76]. FLASH operates at a 10 Hz repetition rate, producing electron bunches in bursts. Each burst contains a train with a maximum of 800 bunches, lasting up to 800 µs, with an internal bunch repetition rate of up to 1 MHz [72]. The generated electrons are then accelerated to relativistic energies in the superconducting linear accelerator (linac) [77]. Between the first and the second stage of the acceleration, bunch compressors are installed to reduce the electron bunch length to approximately 100 fs [78]. Afterward, an electron kicker behind the FLASH accelerator splits the 800 µs burst into two parts, one sent straight to FLASH1 and the other kicked into FLASH2 [72, 79]. The variable-gap undulators of FLASH2 provide users with the flexibility to select beam parameters, such as bunch spacing, pulse length, and a wide range of wavelengths at a fixed accelerator energy, with minimal dependence on FLASH1's parameters [79–81].

3.2 Diagnostic Beamline at FLASH

For temporal diagnostics of XUV pulses at FLASH2, the FL21 beamline was designed, built and put into operation [83]. In A.2, the technical details of the FL21 beamline are

presented. The beamline consists of a flat cutting mirror that splits the FEL beam, a focusing mirror with a 1.5 m focal distance, a laser-based THz source, a THz streaking setup, and a direct beamline branch for additional diagnostics.

For a homogeneous THz streaking field, the FEL beam diameter in the THz streaking setup must be significantly smaller than the THz focal diameter. To achieve the highest streaking fields and ensure good temporal resolution, the THz beam is focused near the diffraction limit, resulting in a beam diameter of approximately 1 mm FWHM, as measured with a THz camera. This is considerably smaller than the unfocused FEL beam diameter in the experimental hall, which ranges from 3–10 mm FWHM. Therefore, integrating the setup directly into the main beamline is not feasible without first focusing the FEL beam. To address this, a cutting mirror is implemented to extract a fraction of the FEL beam and send it into the THz streaking setup while allowing the remaining beam to continue along the main beamline. This enables parasitic pulse duration measurements without disrupting operations at the direct beamline branch. The cutting mirror is mounted in an ultra-high vacuum (UHV) 160 CF cube on a three-axis motorized manipulator. As shown in Fig. 2 in A.2, the lower edge of the cutting mirror is cut at an 85° angle to prevent reflections from the bottom surface and to allow the gold coating to extend almost to the edge (<0.1 mm). A specialized mechanical mount partially encloses the mirror, leaving the lower part free to avoid blocking the transmitted beam. The vertical movement of the mirror allows a fraction of the FEL beam to be reflected into the streaking chamber, while the unaffected fraction continues along the straight path.

The reflected beam then reaches the focusing mirror, installed in a UHV 160 CF cube mounted on a motorized support with three translational axes and three angular degrees of freedom for precise alignment. Both the cutting mirror and focusing mirror are gold-coated to accommodate a wavelength range of approximately 7–50 nm. Each mirror measures 150 x 15 mm, providing a horizontal clear aperture of about 10.7 mm at a grazing incidence angle of 4°. The toroidal focusing mirror focuses the beam to a spot size of 100–200 µm FWHM, depending on the FEL parameters. The focus position is aligned with the interaction point of the THz streaking setup. The focal spot size does not change significantly when varying the fraction of the beam reflected by the cutting mirror. Upstream of the focusing mirror, a motorized CF40 manipulator holds a Ce:YAG crystal screen ($20 \times 20 \times 0.2$ mm) monitored by a CCD camera to observe the FEL beam shape. This manipulator also contains four thin metal filters made of different

materials for adjusting the pulse energy entering the streaking setup independently of the uncut FEL beam. Additionally, another Ce:YAG crystal screen with a CCD camera on a pneumatic mover is installed between the focusing mirror and the streaking setup.

In the next chapter, a detailed explanation of the THz streaking setup will be provided, including the measurement process and data analysis methods used to extract the pulse duration, arrival time and chirp.

3.3 Terahertz Streaking Setup

The THz streaking setup consists of two main stages: the THz generation and the interaction chamber. The THz radiation is generated through optical rectification in a $LiNbO_3$ crystal, where the tilted pulse front (TPF) of the pump ensures efficient phase-matching between the group velocity of the pump pulse and the phase velocity of the generated THz pulse. This is achieved by tilting the intensity front of the pump pulse relative to its phase front, allowing the THz pulse to propagate parallel to the tilted front [84, 85]. The pump is a tabletop infrared (IR) laser operating at 1030 nm with 8 nm bandwidth, a pulse energy of 3.5 mJ and a pulse duration of 1 ps at a repetition rate of 10 Hz, which is optically synchronized with the FLASH main laser oscillator [83]. As shown in Fig. 3.2, the pulse front of the IR laser is tilted by a diffractive grating with 1500 grooves/mm and imaged using a 4f telescope system composed of two lenses with focal lengths of f1 =200 mm and f2 = 125 mm. This setup directs the IR pulse onto the $LiNbO_3$ crystal, satisfying the phase-matching condition for optical rectification. The outcome is a single-cycle THz pulse with an almost linear slope of about 600 fs, linearly polarized in the vertical direction, centered at 0.7 THz, with a pulse energy of 3.5 µJ. This results in an electric field with a strength of up to 150 kV/cm [62].

The THz pulse then propagates toward the UHV interaction chamber. The beam is first reflected by a flat gold-coated mirror onto a parabolic mirror (PM1) with a focal length of 152.4 mm that collimates it. PM1 and a second flat mirror together form a periscope, which rotates the polarization into the horizontal direction and guides the beam downwards. The collimated THz beam then enters the interaction chamber through a 5 mm thick Zeonex 480 vacuum window, which has a clear aperture of 50 mm. The chamber is equipped with a parabolic mirror (PM2) with a focal length of 101.6 mm, which focuses the THz beam and ensures collinear overlap with the FEL beam in the interaction region. The FEL pulse enters the interaction chamber by passing through a

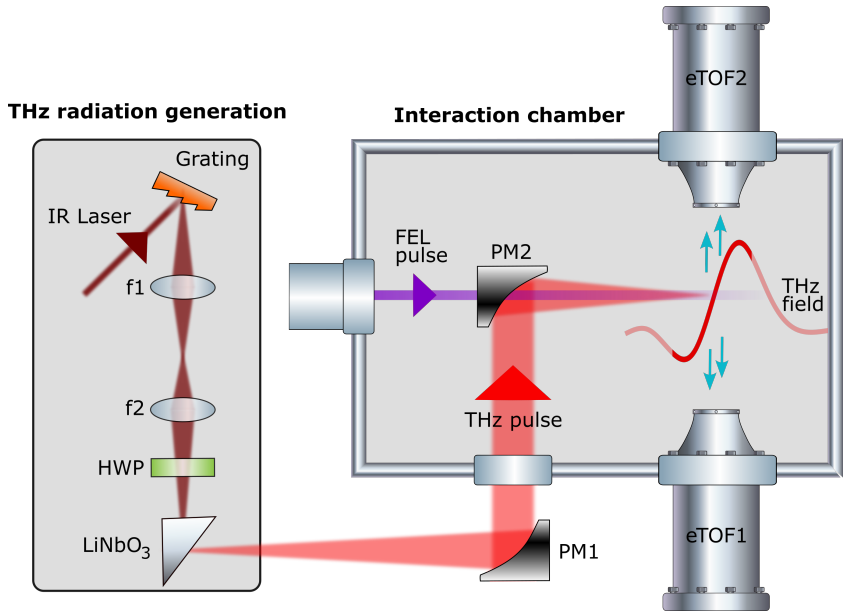

Figure 3.2: Schematic illustration of the THz streaking setup, showing both the THz generation stage and the interaction chamber. In the THz generation stage, the pulse from the IR laser is tilted via diffractive grating and then imaged onto the $LiNbO_3$ crystal using a $4f$ system ($f1$ and $f2$) to generate THz radiation. A half-wave plate (HWP) is placed before the crystal to adjust the polarization of the IR pulse for optimal THz generation. The generated THz pulse is collimated and directed to the interaction chamber via a parabolic mirror (PM1) and then focused into the interaction region via a second parabolic mirror (PM2). The FEL pulse passes through a hole in the PM2 and overlaps with the THz pulse.

3 mm hole in PM2. The interaction region is monitored by three eTOF spectrometers (Kaesdorf ETF). eTOF1 and eTOF2 are positioned on opposite sides of the interaction point in the same plane as the linear polarization of both the THz and XUV pulses, enabling chirp measurements. eTOF3 is installed upstream of the interaction region, perpendicular to the THz field polarization plane, and thus measures the unstreaked photoelectron spectrum. Each eTOF is mounted on a three-axis manipulator, enabling precise positioning relative to the interaction region [83].

A gas needle, adjustable in the x-y-z directions, introduces noble gas atoms (typically neon) into the interaction region, where they are photoionized by the FEL pulse, generating photoelectrons. These photoelectrons then interact with the incoming THz pulse. Depending on the relative phase between the THz and FEL pulses, some photoelectrons are accelerated, while others are decelerated. This interaction modifies the kinetic energy of the photoelectrons, which is subsequently measured by eTOF1 and eTOF2. The high

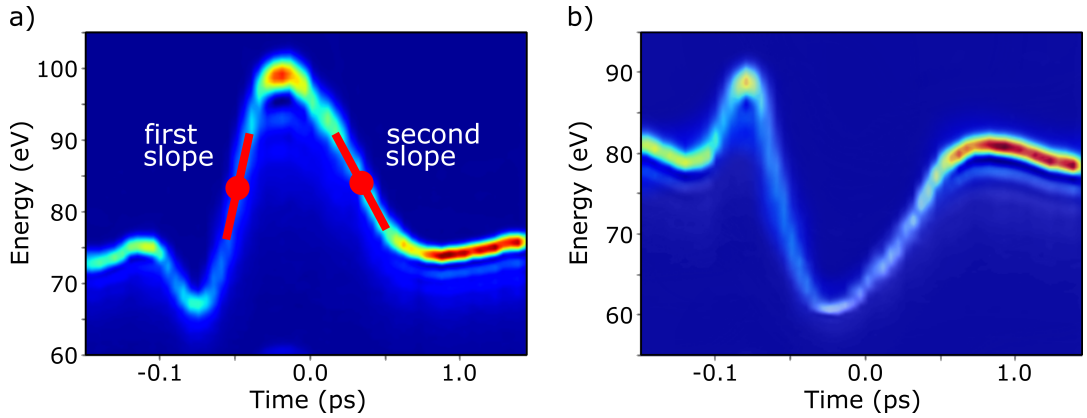

Figure 3.3: THz streaking trace (delay scan) for neon 2p photoelectrons ionized by 13 nm XUV pulses, simultaneously measured by a) eTOF1 and b) eTOF2. Streaking can be performed on either the first or second slope of the THz field, indicated by red lines. The zero-crossing points are marked with red dots. Figure from A.2.

intensity of FEL radiation can induce space-charge effects in the interaction region. During photoionization, the accumulated positive charge of ions decelerates photoelectrons, causing additional broadening of the photoelectron spectrum [86]. To mitigate space-charge effects, experimental parameters such as gas pressure and FEL intensity can be adjusted.

By varying the delay between the THz pulse and the XUV pulse, the kinetic energy of the photoelectrons as a function of the delay is measured using eTOF1 and eTOF2, as shown in Fig. 3.3 a) and b). The resulting trace, commonly referred to as the "streaking trace," is proportional to the vector potential A_{streak} of the THz field [40], as previously discussed in the theory chapter. Since the THz field is polarized within the plane of the two eTOFs, one eTOF records an energy upshift, while the other detects a corresponding downshift.

After measuring the streaking trace, the delay between the THz and FEL pulses is set to the middle of the linear part of the slope (shown as red dots in Fig 3.3 a)) to achieve maximum broadening. At these optimal points, both the streaked and unstreaked spectra are measured. The pulse duration can then be calculated using Eq. 2.29. In addition to pulse duration, the technique also enables the precise measurement of the XUV pulse arrival time. The streaking process induces a shift in the mean photoelectron energy that is directly proportional to the arrival time difference between the XUV pulse and the THz field, allowing for accurate determination of the XUV pulse arrival time. FLASH typically operates in burst mode, generating several hundred XUV pulses per burst, with

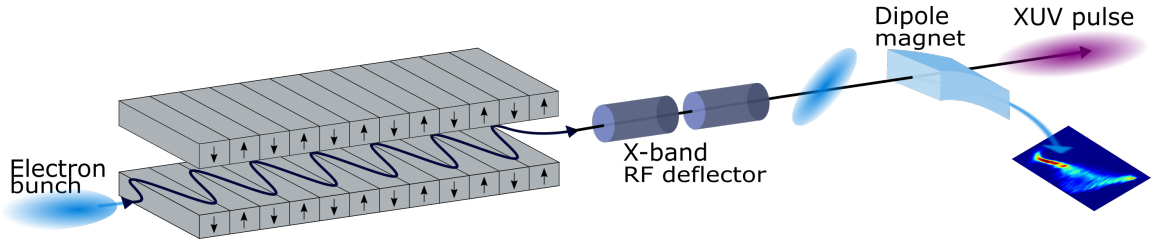

Figure 3.4: Schematic layout of PolariX TDS installed downstream of the undulator. The setup includes an X-band RF deflector which introduces a transverse kick to the electron bunch, and a dipole magnet that disperses the bunch vertically. The dispersed bunch is then projected onto a screen. Figure adapted from [88].

pulse separations of up to 1 µs and a burst repetition rate of 10 Hz. The THz source also operates at a 10 Hz repetition rate, allowing us to streak only a single FEL pulse per burst. For the standard analysis, the second FEL pulse produced only 1 µs later than the streaked one is taken as the unstreaked spectrum. For pulse durations longer than 50 fs, the streaked spectra are sufficiently broader than the unstreaked ones, allowing the use of the second FEL pulse as the reference. The pulse-to-pulse fluctuations of the unstreaked spectra are sufficiently small to not impact the analysis. However, for pulses shorter than 50 fs, the broadening introduced by THz streaking is relatively small. In this case, the reference spectrum should be recorded with eTOF3 from the same SASE FEL pulse, prior to its interaction with the THz field.

THz streaking enables precise measurements of pulse duration and arrival time over a wide range of wavelengths and pulse energies. In addition, FLASH is equipped with a transverse deflecting structure (PolariX TDS) to characterize the longitudinal properties of electron bunches [30, 87]. The next chapter explains its capabilities and applications in detail.

3.4 PolariX TDS Setup

PolariX TDS consists of an X-band RF deflector and a dipole magnet that acts as an energy spectrometer. PolariX is installed downstream of the undulators at FLASH2, therefore it enables detailed studies of the impact of SASE on electron bunches. As shown in Fig. 3.4, PolariX operates by passing an electron bunch through an X-band RF deflector. This deflector introduces a transverse kick to the electrons based on their longitudinal position within the bunch, similar to the effect of streaking. As a result, the longitudinal current distribution of the electron bunch is mapped onto its transverse

profile. The bunch is then energetically dispersed via the dipole magnet. When the TDS streaks the beam perpendicular to the dipole's bending plane, the resulting configuration allows for direct visualization of the longitudinal phase-space distribution. This improves the optimization of longitudinal bunch parameters [30].

The electrons in the lasing region of the bunch lose energy, transferring it to the XUV pulse, which results in a lower mean energy that can be seen in the phase space image captured by PolariX. Additionally, the SASE process increases the energy spread. By analyzing the phase space image and comparing it to a reference measurement obtained under non-lasing conditions, the shape, length, and frequency chirp of the XUV photon pulses can be inferred [88]. Further details on the analysis procedure are provided in A.3 and A.5.

Chapter 4

Experimental Results

This chapter presents a general overview of the scientific contributions of this thesis. A more detailed explanation of the scientific contributions and findings is provided in the publications included in Appendix A. Throughout the text, they are referenced as A.1, A.2, A.3, A.4 and A.5.

4.1 Arrival Time Measurement of FEL Pulses with THz Streaking

In time-resolved pump-probe experiments utilizing FELs, precise synchronization between the external laser and the FEL pulse is essential. Accurate measurement of the electron bunch arrival time facilitates data sorting and correction, thereby enhancing the temporal resolution. At FLASH, Bunch Arrival-Time Monitors (BAMs) are used to perform these measurements. Using an electro-optical technique, the BAM determines the arrival time of each individual electron bunch [89]. The closest BAM to the experiment endstations is located approximately 200 meters upstream, just downstream of the second bunch compressor. Over this 200-meter distance between the BAM and the experiment endstation, trajectory jitter, synchronization uncertainties, and the intrinsic timing jitter of SASE pulse generation can limit the accuracy of predicting the XUV arrival time based on upstream BAM measurements.

Although the THz streaking setup was initially designed for XUV pulse duration measurements, it also enables precise determination of the XUV arrival time relative to the THz field. This motivates a dedicated experimental investigation of the correlation

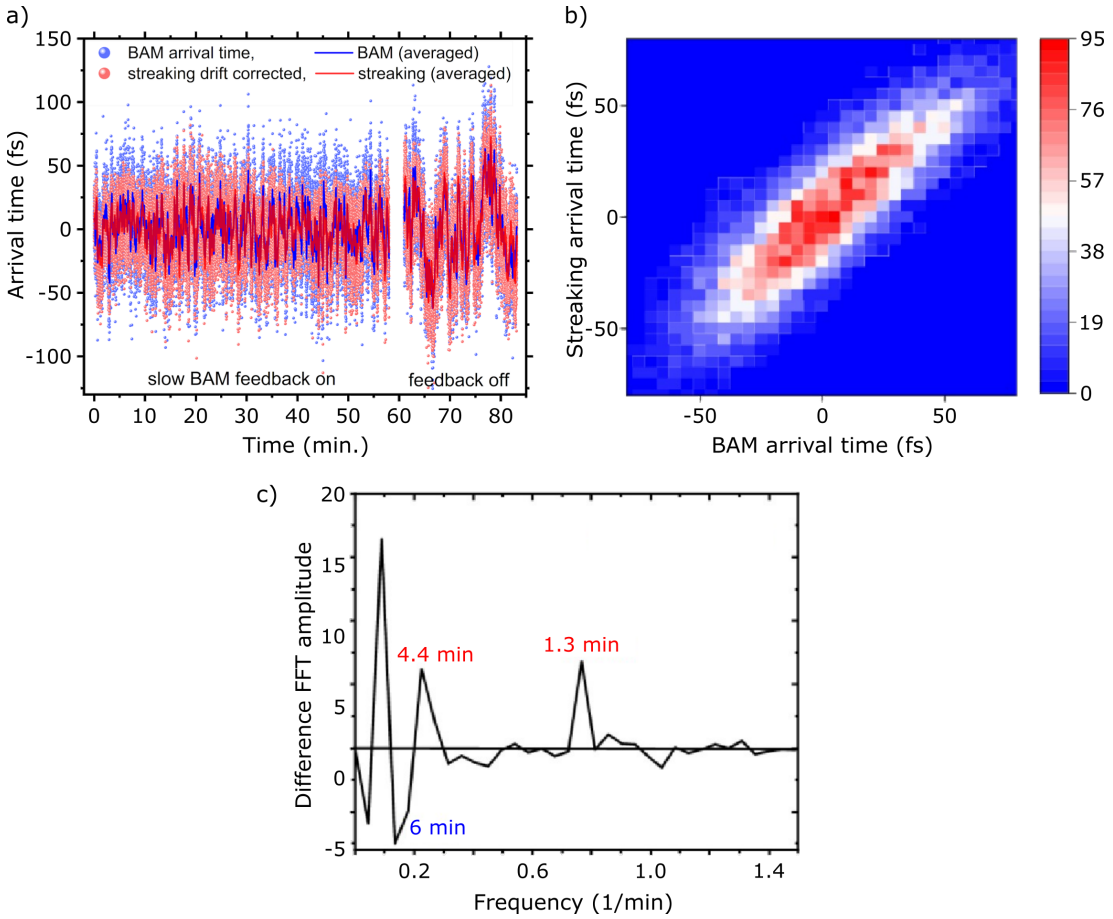

Figure 4.1: a) Arrival time measurements were conducted over 80 minutes using THz streaking and BAM simultaneously. The arrival time of individual XUV photon pulses (red dots) and electron bunches (blue dots) are displayed. The red and blue lines represent a 10-second average, showing the arrival time drifts. During the first 60 minutes of the measurement, the "slow BAM feedback" was actively applied to stabilize the arrival time of the accelerator. For the final 20 minutes, the feedback was switched off, illustrating the impact on the stability of the arrival time. b) Correlation plot of the arrival times measured with the BAM and THz streaking without feedback stabilization. The correlation width is 13 fs rms. c) Difference of the Fourier transforms (FFTs) of arrival time data from BAM and THz streaking (without drift correction), highlighting the individual sources of timing deviation. Positive peaks correspond to deviations originating from the THz streaking setup, while negative peaks are associated with BAM. Figure from A.2.

between the BAM signals and the THz streaking measurements. The streaking process causes a shift in the mean photoelectron energy, which is directly proportional to the arrival time difference between the XUV pulse and the THz field. Since the IR laser generating the THz field is synchronized to the FLASH master laser oscillator (MLO) with a temporal precision of 5 fs rms, the XUV arrival time can be compared to the

electron bunch arrival time measured by the BAM. This can help evaluate the reliability of BAM measurements for experimental endstations. By directly comparing the XUV arrival time measured via THz streaking with the electron bunch arrival time from BAM, we can evaluate drifts caused by each technique and potential offsets between the two methods. Such a comparison provides insight into the accuracy and stability of BAM over long distances and helps quantify its limitations.

Figure 4.1 a) presents long-term arrival time measurements from THz streaking and BAM. As explained in A.2, the XUV arrival time determined via THz streaking achieves a precision of 5–10 fs rms, depending on the FEL settings . BAM, on the other hand, measures the bunch arrival time with a precision of 5 fs rms. These measurements, based on approximately 50,000 FEL pulses, show strong agreement between the arrival time obtained from THz streaking and BAM, confirming the reliability of BAM measurements for experiment endstations despite the 200-meter separation between the two diagnostics. As illustrated in Figure 4.1 b), the comparison reveals a strong correlation between XUV and electron arrival times, with deviations of only 6 fs rms (10-second averages) and 12–13 fs rms for single-shot analysis.

Additionally, a fast Fourier transform (FFT) analysis was performed on the arrival time measurements from both methods. This analysis helps differentiate frequencies that originate from the accelerator and appear in both techniques, from those present only in THz streaking or BAM. As shown in 4.1 c), the difference in the Fourier transform analysis of the two techniques reveals distinct frequencies that contribute to the drifts in the THz streaking data, likely due to the regulation cycles of the chiller for the IR laser amplifier. These insights highlight the value of the THz streaking setup not only for arrival time measurements but also for diagnosing timing drifts within the accelerator and BAM. This capability enhances the accuracy of timing diagnostics, ensuring better synchronization for high-precision experiments.

As mentioned earlier, the primary purpose of the THz streaking technique is to measure the duration of XUV pulses. The next chapter will explain the concept and test measurements that enable the parasitic measurement of pulse duration in more detail.

4.2 Parasitic Pulse Duration Measurement of SASE XUV Pulses

In the optical and X-ray regimes, obtaining a portion of a beam using a beamsplitter is relatively straightforward. However, in the XUV range, no suitable beamsplitters exist due to material limitations and absorption effects. This presents several challenges, one example is the implementation of a delay unit in pump-probe experiments [90] or conducting a parasitic measurement of the pulse duration. To overcome this limitation, an alternative approach known as the cutting mirror is used. Instead of partially transmitting and reflecting the beam, as a beamsplitter would, the cutting mirror intercepts a portion of the beam while allowing the rest to propagate freely.

As explained in Chapter 3.2, the FL21 beamline is equipped with a cutting mirror that can reflect a variable fraction of the FEL beam to the streaking setup, enabling the near-parasitic measurement of the XUV pulse duration while allowing the remaining beam to be utilized for another experiment. The feasibility of this parasitic scheme was investigated by cutting and sending varying fractions of the FEL beam to the streaking setup across different wavelengths, measuring the pulse durations. This scheme, discussed in detail in A.2, shows that approximately 1 µJ of the FEL pulse energy is sufficient for standard THz streaking measurements. This energy level ensures an accurate determination of the pulse duration with an estimated accuracy of ±20% and arrival time with a few femtosecond precision, without inducing space-charge effects [63].

Pulse duration measurements were conducted with different cutting ratios. Data were collected during multiple campaigns, covering wavelengths from 10 nm to 34 nm, pulse energies between 20 µJ and 300 µJ, and pulse durations from 50 fs to 300 fs FWHM, for beam fractions ranging from 4% up to the full beam. To ensure consistent experimental conditions, the streaking setup remained unchanged during cutting mirror experiments, while a gas attenuator [91] was adjusted to maintain a constant number of photoelectrons for all cutting ratios.

The results presented in Fig. 4.2 confirm that the average pulse duration can be reliably determined using as little as 4% of the FEL beam. The measurements showed no clear dependence of the measured pulse duration on the fraction of the FEL beam used. Minor variations in the average pulse duration were observed, likely due to drifts in FEL parameters over the extended measurement period, as setting up the measurement

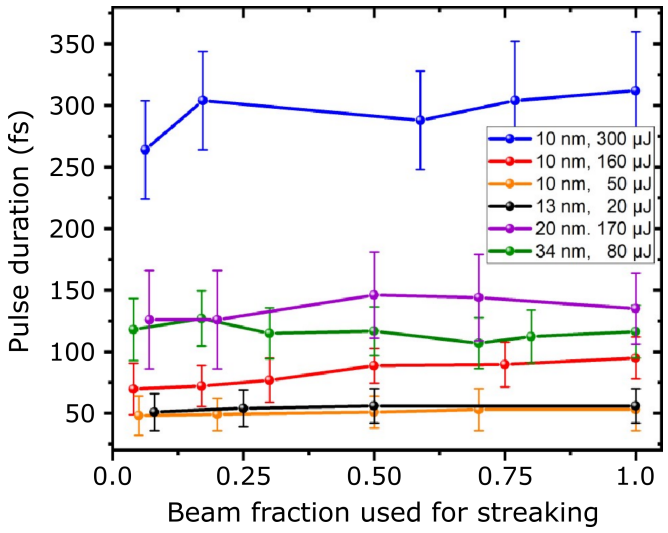

Figure 4.2: By partially inserting the cutting mirror into the FEL beam, only a fraction of the beam is used for pulse duration measurements. The average pulse duration over several thousand FEL pulses (points) and the rms width of the pulse duration distribution (error bars) for various FEL settings are displayed. The results indicate no significant difference between pulse durations measured using 4% of the FEL beam and those measured with larger fractions. Figure from A.2.

for a specific cutting fraction takes several minutes to half an hour. Pulse duration measurements using different fractions of the FEL pulse show that the concept of using a cutting mirror allows a near-parasitic temporal diagnostic at FEL facilities. The experimental results demonstrate that it is possible to reliably determine the average pulse duration using only a small fraction of the FEL beam, while the rest can be used for an experiment.

Beyond pulse duration measurements, the THz streaking setup also captures the XUV pulse shape, providing insight into its temporal structure. Similarly, PolariX TDS serves as another diagnostic tool at FLASH2, enabling the reconstruction of the XUV pulse shape from analyzed PolariX images. In the next chapter, we present and compare the XUV pulse shape measurements obtained using THz streaking and PolariX TDS.

4.3 Temporal Shape of SASE XUV Pulses

The temporal profile of SASE XUV pulses is investigated using THz streaking and PolariX TDS simultaneously and is presented in A.5. While THz streaking directly analyzes XUV pulses by mapping their temporal structure into the energy distribution of emitted

photoelectrons, the PolariX TDS measures the energy distribution of the electron bunch downstream of the undulator to reconstruct the XUV pulse shape indirectly. A laser heater [92, 93] was used in different configurations to manipulate the electron bunch, thereby affecting the resulting XUV pulse profile. These configurations varied in both the undulator wavelength and the laser heater parameters. The wavelength was increased from the first to the second configuration, while in the third configuration, overheating with the laser heater was applied. To enhance temporal features for comparison, a beam setup with nonlinear compression was employed, generating an electron bunch with two current spikes. The TDS analysis employed both center of mass (COM) and root mean square (RMS) methods to reconstruct pulse profiles [88]. Approximately 3000 lasing-on and 2000 lasing-off samples were collected at an electron beam energy of 965 MeV across all configurations.

In setup1, the undulator was tuned for a wavelength of 11 nm. As shown in Fig. 2 in A.5, inaccuracies in TDS reconstruction were observed, particularly around the second current spike at 320 fs due to mismatches in the lasing-off reference. Meanwhile, THz streaking did not detect a second XUV pulse. By increasing the wavelength to 17 nm, in setup2, the mean FEL pulse energy increased to ∼280 µJ, and the lasing-on data exhibited a larger energy spread. In this configuration, both the COM and RMS methods confirmed the presence of two XUV pulses. The THz streaking results closely matched the COM-based TDS profiles. In setup3, the laser heater was maximized to overheat the electron bunch and suppress the weaker XUV pulse, reducing the mean FEL pulse energy to ∼90 µJ. The COM and RMS methods showed a minor signal for the second pulse, whereas THz streaking did not detect a second peak. The incorrect secondary pulse observed in TDS analysis was likely due to artifacts introduced by strong variations in low-energy electron densities and rapid changes in electron bunch chirp.

By combining TDS analysis and THz streaking, we investigated the laser heater's ability to manipulate the electron bunch and suppress one of two XUV pulses. While TDS provides femtosecond resolution, its accuracy is limited by shot-to-shot variations in the electron bunch energy arising from the acceleration process, as well as sensitivity to energy chirp and laser heater effects. THz streaking, though limited in temporal resolution, offers direct XUV intensity measurements and helps resolve TDS discrepancies. In addition to the temporal intensity variations along the FEL pulse, another key degree of freedom is the variation in electron energy over the bunch, i.e., the energy chirp. In the following chapter, we extend our investigation by studying the impact of chirp on FEL pulses using

PolariX TDS and THz streaking.

4.4 Influence of XUV Chirp on FEL Pulses

While analyzing the pulse shape using THz streaking and PolariX TDS, several FEL settings exhibited an energy chirp in the PolariX images. A chirped electron bunch leads to a broader bandwidth in the emitted XUV pulse, which can be advantageous for various applications. In absorption spectroscopy [8, 94, 95] and X-ray crystallography [96], a broader spectrum enables the simultaneous coverage of a wider range of spectral lines or diffraction patterns within a single FEL pulse, minimizing the need for time-consuming wavelength scans. Beyond spectral broadening, chirped FEL pulses also offer control over ultrafast dynamics. In femtochemistry, chirp can be deliberately applied to control reaction pathways by selectively enhancing or suppressing specific transitions [97–99]. Additionally, chirp plays a crucial role in pulse shaping for strong-field quantum control, enabling precise manipulation of ultrafast electronic dynamics [100].

An example of a bunch with energy chirp is illustrated in Fig. 4.3 a). In FELs, chirp typically arises from the time-energy correlation in the electron bunch, which translates into a time-dependent shift in the frequency of the emitted XUV pulse. Different parameters can result in a chirp in the SASE FEL pulses, including the acceleration and compression processes in the FEL or due to other beam dynamics within the undulator. This chapter presents the measurement of the energy chirp of the electron bunches and the corresponding chirp in the XUV pulses. Parallel measurements of chirp were performed using PolariX TDS and THz streaking. A detailed comparison of these two diagnostic techniques is provided in A.3, highlighting their respective strengths, limitations, and abilities to characterize XUV chirp.

For chirp measurement using PolariX, it is essential to analyze the electron chirp within the lasing region of the bunch. The energy chirp is extracted from the center-of-gravity curves in the lasing-off condition by performing a linear fit within this region. Subsequently, the electron energy chirp (in MeV/fs) is mapped to the XUV frequency chirp (in meV/fs). An example of an energy chirp measurement using PolariX is shown in Fig. 4.3 b). This analysis becomes challenging for low-energy pulses or when multiple regions of the bunch contribute to lasing. In contrast, THz streaking provides a direct measurement of the linear chirp of the XUV pulse under various assumptions, following the approach described in Sec. 2.2.3.

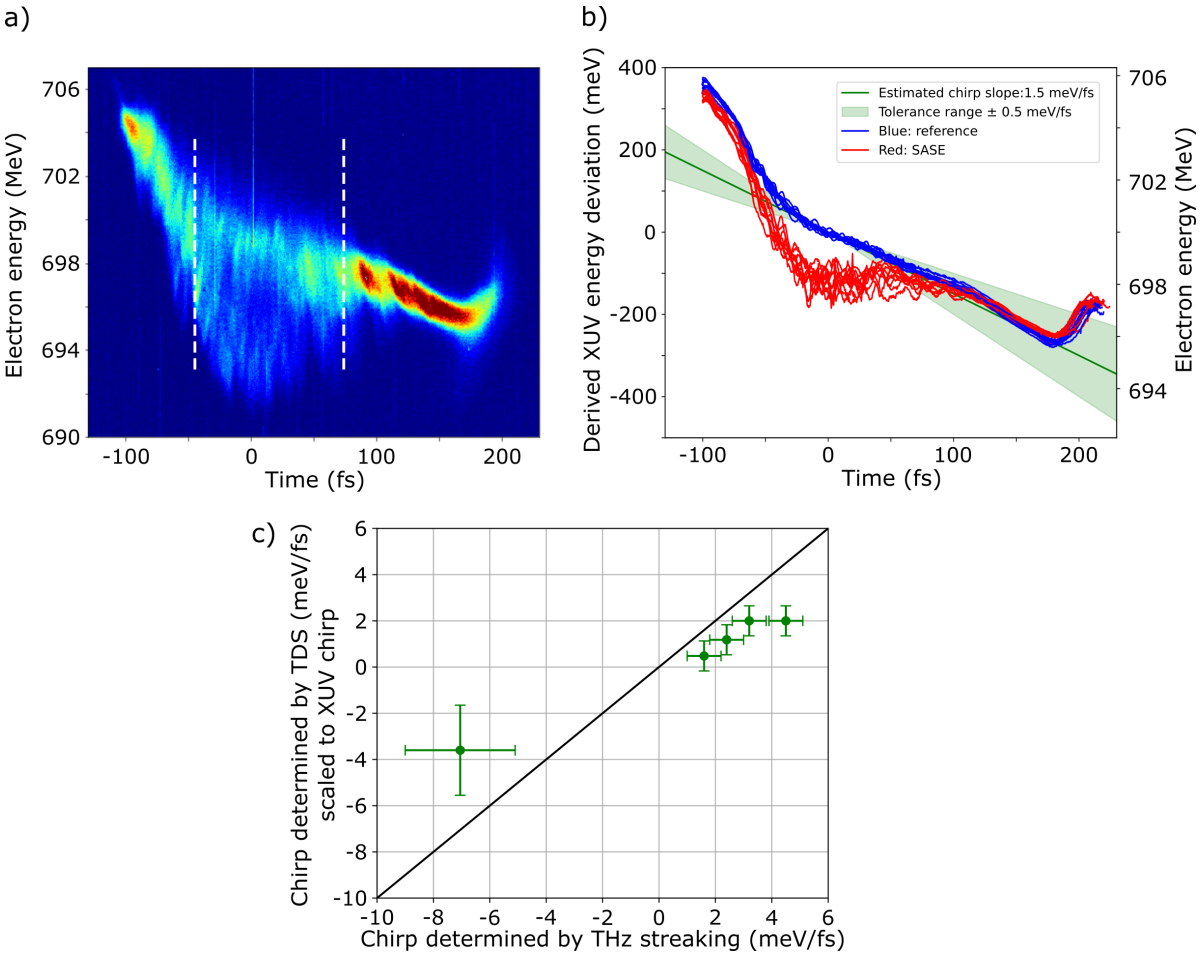

Figure 4.3: a) Single-shot PolariX image showing an electron bunch with a positive energy chirp. The white dashed lines indicate the SASE region. b) Computed center of gravity from multiple PolariX images for the FEL setting shown in (a). Lasing-on (red) and lasing-off (blue) conditions are shown. The green line represents the averaged energy chirp from lasing-off measurements, with the shaded area showing the linear fit variation. c) Comparison of XUV chirp measurements by THz streaking and PolariX TDS. The linear chirp measured with THz streaking agrees with predictions from electron bunch data. Each data point represents the average value of thousands of single-shot measurements with their respective fluctuations taken simultaneously by both methods. Figure from A.3.

Fig. 4.3 c) compares the chirp measurements obtained from both techniques for different FEL settings. A wide range of chirp values, including positive and negative chirps, were measured with XUV pulse durations between 80 and 180 fs and photon energies ranging from 44 to 77 eV. While the results follow a similar overall trend, PolariX seems to systematically underestimate the chirp compared to the values obtained from THz streaking. In A.3, the XUV chirp measured via THz streaking was initially

analyzed based on Ref. [69]. However, that work considered the parameter c_ϕ instead of the instantaneous energy chirp c_E, leading to a missing factor of two in the analysis. This error was identified after the publication of A.3. A corrected plot, based on Eq. 2.34, is presented here, and an erratum for the original paper is currently in preparation. Negative chirps showed larger fluctuations due to a less stable electron bunch configuration, showing the sensitivity of chirp measurements to accelerator settings.

Both THz streaking and PolariX TDS have advantages and limitations in chirp measurement. One limitation of THz streaking is its inability to detect higher-order chirps or complex non-linearities in the pulse structure using the Gaussian fit. Advanced reconstruction approaches can overcome this by extracting higher-order phase information [101]. PolariX TDS had challenges in low-energy settings where identifying the lasing part of the electron bunch was less straightforward. Despite these limitations, the combination of the two techniques proved effective in providing a comprehensive analysis of the chirp characteristics.

As we are able to characterize the chirp of FEL pulses, we now investigate its impact on the amplification process. The next chapter focuses on the single-shot characterization of FEL pulse duration and how chirp affects its evolution during the amplification process. By comparing experimental measurements with simulations, we assess the role of chirp in FLASH pulses. This analysis provides deeper insight into the amplification dynamics and the key factors affecting agreement between experiment and theoretical predictions.

4.5 Characterization of SASE XUV Pulses During the Amplification Process

From the previous chapter, we learned that FEL pulses exhibit a frequency chirp, which we measured using two different techniques. However, to fully understand its impact, we must examine how chirp influences pulse properties through simulations and compare the results with experimental data. In this chapter, we study the evolution of FEL pulses throughout the amplification process and compare the experimental data with simulation results. This analysis provides deeper insights into the underlying physics and helps refine our theoretical models for FEL operation.

As explained in Sec. 2.1.2, the stochastic nature of the SASE process introduces significant fluctuations in the radiation properties, making single-shot characterization of

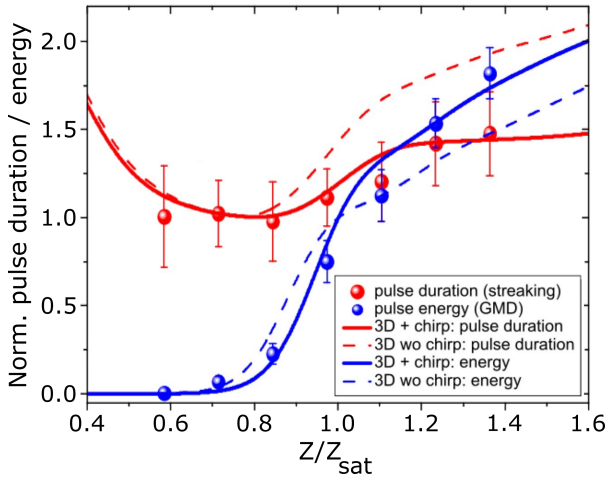

Figure 4.4: Evolution of pulse duration (red circles) and pulse energy (blue circles) of the fundamental radiation (12 nm) along the undulators, with the undulator length normalized by the saturation length (z_{sat}). The pulse energy is normalized to the saturation energy and the pulse duration is normalized to the minimum pulse duration. Experimental data are averaged over thousands of single-pulse measurements and show strong agreement with chirped 3D simulations (solid lines), while unchirped 3D simulations (dashed lines) show a discrepancy. Figures from A.1.

FEL pulses essential. Understanding the evolution of SASE along the amplification process is particularly important for optimizing FEL performance and designing experiments. Therefore, in A.1 we employed terahertz streaking to investigate the temporal properties of SASE XUV pulses. We measured both pulse duration and pulse energy across a wavelength range of 8 to 34 nm, as functions of the undulator length contributing to the lasing process. The undulators were opened sequentially and the conditions were optimized for each setting to record the gain curves over several measurement campaigns, giving insights into the amplification process.

The experimental results were compared with three-dimensional (3D) time-dependent FEL simulations, both with and without energy chirp on the electron bunch. As shown in Fig. 4.4, the experimental data show a continuous increase in pulse energy (blue circles) and a rather small increase in pulse duration (red circles) throughout the amplification process. The chirped 3D simulation (solid lines) showed better agreement with the experimental data compared to the unchirped 3D data. This observation confirmed the presence of XUV chirp in FLASH pulses, which was previously analyzed in Sec. 4.4.

Beyond the fundamental radiation, higher harmonics play a key role in applications requiring shorter wavelengths (higher photon energies). In a SASE FEL with a planar

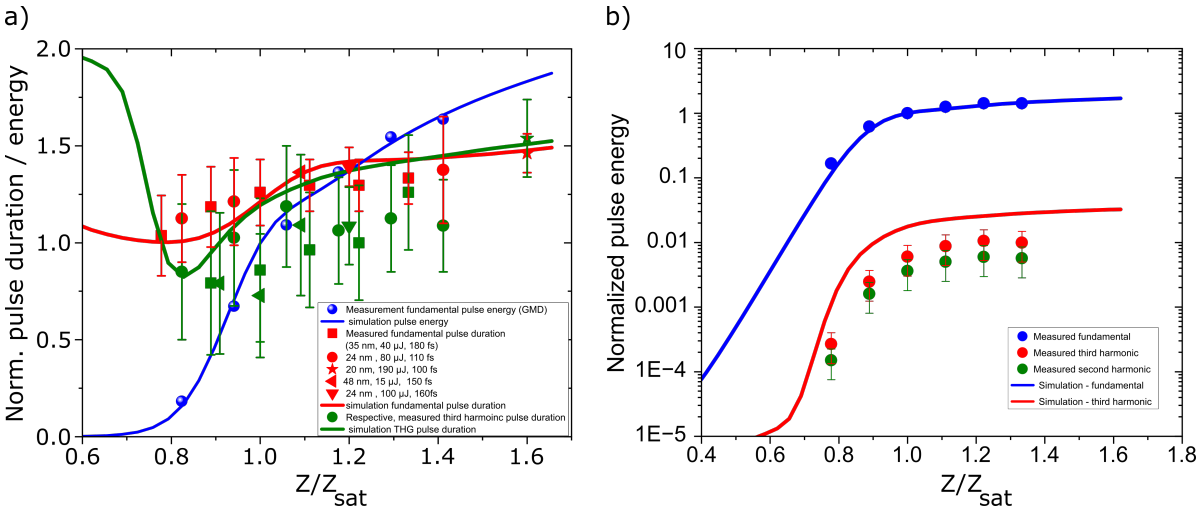

Figure 4.5: a) Evolution of the measured pulse duration for the third harmonic (green) and the fundamental (red) under various FEL settings compared to the chirped 3D FEL simulation (solid lines). b) Evolution of the pulse energy for the fundamental, second, and third harmonics as a function of the undulator length. The energy values are presented on a logarithmic scale, while the undulator length is shown on a linear scale. The energy of the third harmonic rises more quickly than that of the fundamental in the linear regime. In the saturation regime, the growth of pulse energy for both the fundamental and third harmonic becomes more comparable, progressing at a slower rate. Figures from A.4.

undulator, the radiation of the electron beam contains a rich harmonic spectrum. These higher harmonics are generated through the nonlinear interaction between the electron bunch and the undulator radiation, and their properties are strongly influenced by the microbunching dynamics and the energy distribution within the electron bunch. A detailed investigation of the characteristics of the second and third harmonic radiation of FLASH was conducted and presented in A.4. In an ideal scenario for an FEL with a planar undulator and an axisymmetric electron beam, odd harmonics are resonant on-axis and show significant intensities, while even harmonics are largely suppressed due to the inherent symmetry of the system. However, in practical operation, factors such as the finite electron beam size, betatron motion within the undulators, and slight trajectory deviations can lead to the generation of even harmonic radiation. Since these imperfections vary over time and cannot be precisely measured, simulations for the second harmonic were not performed [55, 59, 60, 102].

The evolution of third harmonic radiation during the amplification process was investigated using the same scheme as for the fundamental. The undulators were opened sequentially, with XUV pulse energy and fundamental suppression optimized at each

step. Measurements were performed for various FEL configurations, with fundamental wavelengths from 20 to 48 nm, pulse durations between 100 and 180 fs, and saturation energies ranging from 15 to nearly 200 µJ. As shown in Fig. 4.5 a), the third harmonic measurements were compared with 3D time-dependent simulations that included the energy chirp in the electron bunch.

The experimental data show large variations in third harmonic pulse durations, likely due to the diverse experimental settings across different measurement campaigns. Nevertheless, it follows a trend similar to that observed in the simulations, showing a slight elongation of the pulse duration from the linear regime to deep saturation. However, the measured third harmonic pulse durations are, on average, ∼20% shorter than those of the fundamental and thus slightly shorter than predicted by the simulations. A possible reason is that these measurement were conducted with a standard FEL setup, which is generally not optimized for harmonic emission. Due to limited experimental time, only a few measurements of the second harmonic pulse duration were performed. The results indicated that its pulse duration was comparable to that of the third harmonic and slightly shorter than that of the fundamental.

As shown in Fig. 4.5 b), the energy development of the third harmonic along the undulators follows a rapid increase in the linear gain regime and slower growth in saturation. In comparison, the fundamental has slower growth in the linear regime and then plateaus in the saturation regime. Experimental data align well with the simulation, though absolute harmonic energies are lower than simulations, likely because the standard FEL configuration is not optimized for harmonic emission. The energy of the second harmonic was slightly less than the third harmonic.

The pulse energies of the fundamental XUV radiation produced by FLASH typically range from tens to hundreds of microjoules, while the second and third harmonics contribute 0.2-2% of the fundamental energy, corresponding to nanojoule to low-microjoule levels. Accurate determination of harmonic-to-fundamental energy ratios is challenging due to several influencing factors along the beam path. These include attenuation by the gas attenuator, mirror reflectivity, wavelength-dependent photoionization cross-sections, angular distribution of photoelectrons, and transmission optimization for faster electrons in the electrostatic lens of the eTOF detector. Collectively, these effects result in an uncertainty of approximately ±50% for the energy ratio measurements.

Over multiple FEL configurations and experimental campaigns, the second harmonic

energy ratio was measured to be 0.1-0.6%, while the third harmonic ratio was 0.2-0.6%, with specific setups achieving up to 1% for the third harmonic. Simulations predict a maximum third harmonic contribution of 0.9-1.8%, depending on the undulator parameter K, though this is reduced in practice by the electron beam's energy spread. Despite variations in FEL parameters between 3D chirped simulations and experiments, there is overall good agreement, which supports the findings presented in the previous chapter on XUV chirp. Therefore, the 3D time-dependent FEL simulation provides a reliable framework for understanding both fundamental and harmonic generation dynamics and can serve as a valuable tool for optimizing future FEL experiments across a broad parameter range.

Chapter 5

Conclusion and Outlook

This thesis presented the design, implementation, and experimental validation of the FL21 beamline at FLASH, a dedicated beamline for photon diagnostics with a focus on THz streaking-based XUV pulse characterization. The beamline's dual-branch setup, utilizing a cutting mirror to share XUV radiation, enables both a standalone pulse duration diagnostic and an open port beamline for user experiments. Our results demonstrated the feasibility of utilizing this installation for systematic long-term studies of SASE pulse properties, as well as for on-demand pulse duration measurements to support user experiments.

By comparing reconstructed XUV pulse profiles obtained via PolariX TDS analysis and THz streaking, we identified the strengths and limitations of each approach in measuring the FEL pulse shape. The complementary nature of these techniques allows for more accurate pulse shape determination, particularly in complex phase space scenarios. Our findings also underscored the importance of monitoring lasing-off current profiles with TDS to mitigate drift effects and ensure the reliability of reference measurements.

Another key aspect of this work was the measurement and characterization of the frequency chirp in XUV pulses at FLASH. By employing THz streaking and PolariX TDS simultaneously, we found that both methods follow a similar trend across a wide range of FEL settings, although PolariX seems to systematically underestimate the chirp compared to THz streaking. In addition, our long-term data analysis indicated that frequency chirp is often present in XUV pulses, underlining the necessity of real-time chirp diagnostics, particularly for chirp-sensitive experiments.

Through extensive experimental and simulation studies, we analyzed the evolution of FEL pulse properties throughout the amplification process, comparing with both chirped and unchirped 3D time-dependent FEL simulations. We investigated pulse duration, pulse energy, and their fluctuations across various FEL wavelengths. The results consistently showed that the chirped 3D model provides better agreement with experimental data, capturing key trends in pulse duration and energy evolution throughout the amplification process. The findings confirmed the presence of frequency chirp in FEL pulses and established the chirped 3D model as a reliable tool for future FEL parameter optimization and experimental planning.

Furthermore, we explored the characteristics of the third harmonic radiation at FLASH, showing that its pulse duration is approximately 20% shorter than that of the fundamental, with energy ratios between 0.2% and 0.6%. The measured fluctuations of the third harmonic remained significantly higher than those of the fundamental, aligning with theoretical expectations. These insights enhance our understanding of FEL harmonic properties and their evolution throughout the amplification process, providing valuable guidance for future harmonic-based experiments.

Building on the insights gained in this work, several promising directions for future research emerge. Extending current diagnostics to access even shorter pulse durations will significantly enhance the precision of FEL characterization. Angular streaking facilitates this by enabling single-shot retrieval of both the pulse structure and chirp of few- and sub-femtosecond pulses [42, 43]. A real-time feedback from these diagnostics on pulse duration and XUV chirp could further improve experimental conditions for FEL experiments. Furthermore, advanced reconstruction techniques, such as the method described in Ref. [101], enable the characterization of higher-order chirp. Additionally, expanding the range of investigated FEL parameters, particularly in the context of multi-color operation and higher harmonics, would offer further insights into pulse evolution mechanisms. Moreover, improvements in FEL simulation models based on experimental results will enhance predictive capabilities for optimizing FEL performance.

Appendix A

Peer-Reviewed Publications

A.1 FEL Pulse Duration Evolution along Undulators at FLASH

applied sciences

MDPI

Article

FEL Pulse Duration Evolution along Undulators at FLASH

Mahdi M. Bidhendi *, Ivette J. Bermudez Macias †, Rosen Ivanov †, Mikhail V. Yurkov and Stefan Düsterer *

Deutsches Elektronen-Synchrotron DESY, Notkestr. 85, 22607 Hamburg, Germany; ivette.bermudez@xfel.eu (I.J.B.M.); rosen.ivanov@xfel.eu (R.I.); mikhail.yurkov@desy.de (M.V.Y.)
* Correspondence: mahdi.mohammadi-bidhendi@desy.de (M.M.B.); stefan.duesterer@desy.de (S.D.)
† Current address: European XFEL GmbH, Holzkoppel 4, 22869 Schenefeld, Germany.

Abstract: Self-amplified spontaneous-emission (SASE) free-electron lasers (FELs) deliver ultrashort pulses with femtosecond durations. Due to the fluctuating nature of the radiation properties of SASE FELs, characterizing FEL pulses on a single-shot basis is necessary. Therefore, we use terahertz streaking to characterize the temporal properties of ultrashort extreme ultraviolet pulses from the free-electron laser in Hamburg (FLASH). In this study, pulse duration as well as pulse energy are measured in a wavelength range from 8 to 34 nm as functions of undulators contributing to the lasing process. The results are compared to one-dimensional and three-dimensional, time-dependent FEL simulations.

Keywords: free-electron lasers; temporal diagnostic; XUV pulses; SASE; THz streaking

check for updates

Citation: Bidhendi, M.M.; Bermudez Macias, I.J.; Ivanov, R.; Yurkov, M.V.; Düsterer, S. FEL Pulse Duration Evolution along Undulators at FLASH. *Appl. Sci.* **2022**, *12*, 7048. https://doi.org/10.3390/app12147048

Academic Editor: Luigi Palumbo

Received: 22 June 2022
Accepted: 11 July 2022
Published: 12 July 2022

Publisher's Note: MDPI stays neutral with regard to jurisdictional claims in published maps and institutional affiliations.

1. Introduction

The electron bunches in single-pass, high-gain, free-electron lasers (FEL) propagate through the undulators just once producing the most intense extreme ultraviolet (XUV) and X-ray pulses. The amplification mechanism is the so-called self amplification of spontaneous emission (SASE) resulting in fundamental statistical fluctuations in the radiation properties. The properties of radiation pulse energy and radiation pulse duration have been studied theoretically and experimentally in the last decades for XUV and X-ray ranges [1–4]. It turns out that the pulse energy (i.e., the number of photons in one ultrashort pulse) grows gradually by many orders of magnitude in the amplification process, whereas the pulse duration first decreases in the exponential stage of amplification and then grows by about a factor of two when the amplification process enters the nonlinear regime.

The evolution of the pulse energy along the undulators, the so-called gain curve, has been measured frequently in the past [5–11]. However, to our knowledge, there has been only one study that investigates pulse duration in relation to the number of undulators contributing to the lasing [4]. In this study, however, pulse duration is only estimated by analyzing the spectral fluctuations for one X-ray wavelength. Here, we present a more comprehensive study where we measured the single-shot pulse duration as well as the pulse energy for six different wavelengths at the FLASH2 facility [11]. In addition to the average, we can analyze the single-shot data and provide experimental values for the shot-to-shot fluctuations. To obtain a complete picture of the process, the experimental data are compared with FEL simulations.

2. SASE FEL Amplification Process

The amplification process in SASE FELs develops from the shot noise in the electron beam, passes an exponential stage of amplification, and finally evolves in the nonlinear regime. Figure 1 shows the evolution of the radiation pulse energy and its fluctuations, as well as the evolution of the radiation pulse duration along the undulator. The results are obtained by the time-dependent FEL simulation code FAST using 1D and 3D FEL models [12]. To be specific, we consider the case of an electron beam with a longitudinal

Gaussian profile with an rms duration τ_{el}. Fluctuations in the radiation pulse energy reach a maximum value at the end of the exponential gain regime and subsequently decrease in the nonlinear regime, while the radiation pulse energy continues to grow. In the high-gain exponential regime, the number of modes M in the radiation pulse is defined as the inverse-squared deviation of the radiation pulse energy, $M = 1/\sigma_E^2$, where $\sigma_E^2 = \langle(E_r - \langle E_r\rangle)^2\rangle/\langle E_r\rangle^2$ [2,13]. The saturation point corresponds to the maximum brilliance of the radiation [14,15]. At the same time, the fluctuations in radiation pulse energy decrease by a factor of three with respect to the maximum value. In the framework of the one-dimensional model, the saturation length and coherence time at saturation given by

$$z_{sat} \simeq \frac{\lambda_W}{4\pi\rho}\left(3 + \frac{\ln N_c}{\sqrt{3}}\right), \quad (\tau_c)_{max} \simeq \frac{1}{\rho\omega}\sqrt{\frac{\pi \ln N_c}{18}}, \tag{1}$$

are expressed in terms of the FEL parameter ρ [16] and the number of cooperating electrons $N_c = I/(e\rho\omega)$ [2,13,17]. Here, ω is the radiation frequency, I is the beam current, $-e$ is the charge of the electron, and λ_W is the undulator period.

A practical estimate for the parameter ρ comes from the observation that in the parameter range of SASE FELs operating in the VUV and X-ray wavelength ranges, the number of field gain lengths to reach saturation is about 10 [14]. Thus, the parameter ρ and the coherence time τ_c relate to the saturation length by:

$$\rho \simeq \lambda_W/z_{sat}, \quad \tau_c \simeq \lambda z_{sat}/(2\sqrt{\pi}c\lambda_W). \tag{2}$$

For the number of modes $M \gtrsim 2$, the rms electron pulse length τ_{el} and the minimum radiation pulse length τ_{ph}^{min} given in full-width half-maximum (FWHM) at the end of the exponential gain regime are given by [3,18,19]:

$$\tau_{ph}^{min}(FWHM) \simeq \tau_{el} \simeq \frac{M\lambda}{5\rho} \simeq \frac{M\lambda z_{sat}}{5c\lambda_W}. \tag{3}$$

The minimum radiation pulse duration expressed in terms of coherence time (given in Equation (2)) is

$$\tau_{ph}^{min}(FWHM) \simeq 0.7 \times M \times \tau_c. \tag{4}$$

The radiation pulse duration is mainly defined by the length of the lasing fraction of the electron bunch with some corrections related to the slippage effect. In the beginning of the amplification process, the radiation pulse shape just repeats the longitudinal shape of the electron bunch. In the exponential high-gain regime, the power amplification (and beam bunching) is stronger for higher currents; thus, the radiation pulse duration is reduced as the electron bunch travels along the undulator. When the amplification approaches saturation (full bunching) in the central part of the bunch, the tails of the electron bunch begin to contribute more to the radiation power. Beam bunching continues to grow there and the radiation pulse duration starts to grow as well. The effect of the lasing tails gives the same relative radiation pulse lengthening, as is illustrated in Figure 1. The pulse length at the saturation point is about 1.4 times higher than the minimum pulse for the linear regime given by Equation (2), and it is increased further up to about a factor of two in the deep nonlinear regime. The second effect leading to pulse lengthening is the slippage of the radiation by one radiation wavelength per one undulator period. Evidently, the slippage effect is more pronounced for shorter pulses and longer wavelengths.

The case of "cold" (zero energy spread) and monoenergetic electron bunches has been analyzed in earlier papers in the framework of a 1D FEL model [2,3,19,20]. Using the normalized electron pulse duration $\bar{\tau}_{el} = \rho\omega\tau_{el}$ allows us to describe the simulation results in a universal way for $\bar{\tau}_{el} \gtrsim 2$. The simulation results normalized this way show almost identical behavior for different $\bar{\tau}_{el}$, as illustrated in Figure 1. Note that for $\bar{\tau}_{el} \gtrsim 2$, $\bar{\tau}$ is essentially equal to the number of radiation modes ($\bar{\tau}_{el} \sim M$) [3,19]. The one-dimensional model allows us to describe the physics of pulse length effects and temporal properties of

the radiation in an elegant way involving a minimum number of parameters. However, to describe a real experiment more quantitatively, a three-dimensional model which describes diffraction effects and the effects of betatron motion is needed. In addition, the details of the electron bunch structure (e.g., energy chirp) may be very important for the interpretation of the experimental results. Thus, in this paper we extend the analysis of short pulse effects using the results of three-dimensional, time-dependent simulations carried out with the FAST code. The bold curves in Figure 1 refer to the 3D simulations applying typical FLASH2 experimental conditions: electron energy of 1 GeV, rms energy spread of 0.2 MeV, and rms normalized emittance of 1.4 mm mrad. The lasing fraction of the electron bunch is approximated with a Gaussian distribution of 16 fs rms pulse duration and 1.5 kA peak current, resulting in a radiation wavelength of 13.5 nm. These parameters correspond to the value of $M{\sim}\bar{\tau}_{el} = 5.1$. The results of the simulations are presented with the same normalization procedure as for the 1D case. The first set of simulations refers to the case of a monoenergetic electron beam (bold black curves). We see that the 1D and 3D results for the monoenergetic case are rather similar, starting from the end of the high-gain exponential regime. The difference in the linear regime reflects the spatial mode competition effect which is absent in the 1D model. However, at the end of the high-gain linear regime, the fundamental TEM_{00} FEL mode is significantly larger as compared to other higher spatial modes, and we see a good agreement of the results of the 1D and 3D model.

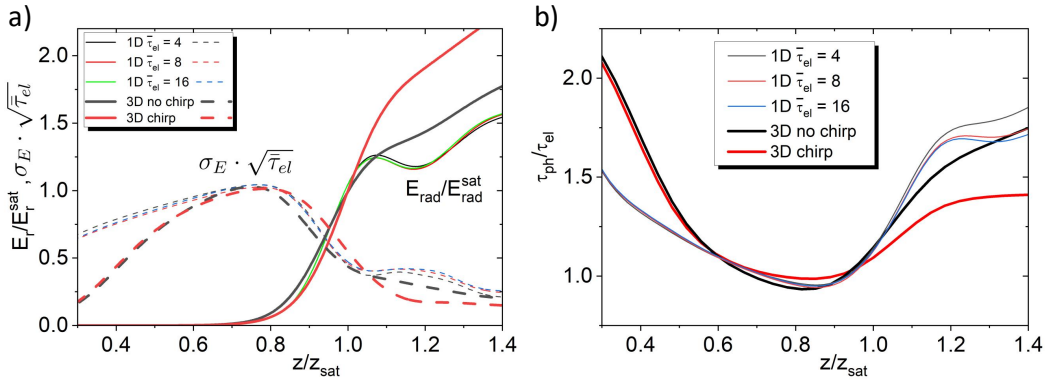

Figure 1. (**a**) Simulated average radiation pulse energy and fluctuations in the radiation pulse energy along the undulator length normalized to the saturation length. The fluctuations are scaled with $\sqrt{\bar{\tau}_{el}}$ to compensate for the pulse duration dependence as described below in the text. (**b**) Simulated evolution of the radiation pulse duration along the undulator length. Thin curves show the result of the 1D model for three different electron pulse lengths $M{\sim}\bar{\tau}_{el} = 4, 8$ and 16. The black bold curve shows the 3D model for the pulse length of $M{\sim}\bar{\tau}_{el} = 5$ without energy chirp, and the bold red curve shows the 3D model including energy chirp.

In the real accelerator, the electron beam is not monoenergetic. The long-pulse, low-current electron beam produced in the electron gun at FLASH is compressed in several stages by a large factor (up to about one hundred), and the peak current is increased correspondingly [21]. To achieve such a large compression, an energy chirp along the electron bunch is applied in the accelerating sections. This energy chirp leads to a bunch compression while the electron bunch moves through dedicated magnetic bunch compressors. An RF-induced energy chirp can be minimized such that it only slightly changes FEL properties with respect to a monoenergetic beam. Still, different kinds of wakefields and collective effects in the electron beam generate an energy chirp along the electron bunch. An example of such an energy chirp induced by the longitudinal space charge field (LSC) is shown in Figure 2 [21]. An important feature of an LSC wake is that the energy of electrons in the lasing fraction of the electron bunch is increased from the tail to the head of the electron bunch. Such a feature leads to a visible increase in the FEL efficiency in the nonlinear regime, which on the other hand leads to an increase in the FEL radiation bandwidth. During the experiments discussed in this paper, the beam formation system

was tuned such that the LSC produced a significant chirp of about 5 MeV peak-to-peak, resulting in an increase in the radiation spectrum bandwidth by about a factor of two with respect to the natural FEL bandwidth. The results of the simulation including the LSC chirped electron beam are shown in Figure 1 as a red bold line. While there is no difference between the chirped and monoenergetic (unchirped) cases in the linear regime, we see visible differences in the postsaturation regime. The pulse duration becomes shorter and the radiation pulse energy grows faster in the chirped case. The explanation of this phenomenon can be found in the positive energy chirp along the lasing fraction of the bunch (see Figure 2). It is well known that a linear energy chirp γ/t along the bunch is equivalent to a linear undulator tapering such that [1]

$$\frac{1}{H_w}\frac{dH_w}{dz} = -\frac{(1+K^2)^2}{2K^2}\frac{1}{\gamma^3}\frac{d\gamma}{cdt}, \tag{5}$$

where H_w is the peak magnetic field and K is the rms value of the undulator parameter. We see that the positive energy chirp is equivalent to an undulator tapering with decreasing field strength along the undulator. It is well known that the application of the undulator tapering with the decreasing field allows one to preserve the synchronism between electrons and the electromagnetic wave, thus increasing the FEL efficiency [13]. With an appropriate optimization of the energy chirp, one can realize conditions which are equivalent to an optimum undulator tapering, when a significant fraction of particles is trapped in the effective ponderomotive potential. The trapped electrons interact stronger with the radiation, and the radiation power grows along the undulator length, while the radiation pulse duration remains nearly constant and the slippage effect is suppressed as well. Of course, an increase in the energy chirp results also in an increase in the radiation bandwidth, as we see from the experimental data.

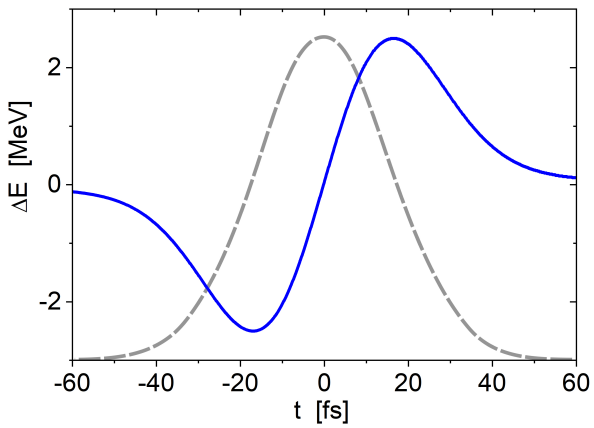

Figure 2. Energy chirp along electron bunch induced by the longitudinal space charge field (blue curve) as it was used for the chirped 3D simulation. The grey dashed curve shows the longitudinal profile of the electron bunch.

In the following sections, we compare experimental results with 3D simulations performed for a chirped electron beam. The energy chirp along the lasing fraction of the bunch was set to 150 keV/fs (Figure 2), leading to a spectral width of about 1% for the XUV pulse, in agreement with several spectral measurements performed at FLASH [5,22–24]. The chirp in the electron bunch leads to a chirp of 30 meV/fs in the 13.5 nm XUV pulse, or, expressed as second-order dispersion, it yields a value of 25 fs^2, which is comparable to the measurements described in Ref. [25], with a second-order dispersion of 50 fs^2, where an exceptionally large bandwidth (i.e., chirp) was requested.

3. FEL Measurements

In order to measure the pulse duration of the XUV FLASH pulses, we used the terahertz streaking technique [26–28]. In short, this method is based on the photoionization of noble gas atoms in the presence of a strong terahertz (THz) field. If the generated electron wave packet is shorter than half the streaking field period, the temporal structure of the wave packet will be mapped onto the kinetic energy distribution of the emitted electrons and can thus be used to determine the XUV pulse duration. The measurements were performed at the dedicated photon diagnostic beamline FL21 in the FLASH2 branch, which is equipped with a permanently installed THz streaking setup [29]. The setup consisted of the interaction chamber containing a time-of-flight spectrometer, a dedicated laser system delivering about 1 ps long pulses at 1030 nm with pulse energy of 3.5 mJ at a repetition rate 10 Hz, and a THz generation setup based on optical rectification using a nonlinear crystal $LiNbO_3$) (for details, see, e.g., [30,31]).

In Ref. [31], it was discussed that there is an optimum number of photoelectrons created in the ionization process by the FEL pulse. One needs sufficiently many electrons to record a single-shot photoelectron spectrum while limiting the number of electrons so that the resulting space charge effects are negligible. For our setup, this leads to an optimum XUV pulse energy in the range of several hundred nJ to few µJ, depending on the wavelength for neon as the target gas ($P_{neon} \sim 5 \times 10^{-7}$ mbar). To ensure the same experimental conditions for all measurements, the streaking setup was left unchanged during the gain curve measurements, while the transmission of a variable XUV attenuator [32] was adapted such that the average number of created photoelectrons was constant for each measured setting. The FEL was operating in the burst mode delivering three pulses (with 1 µs spacing), while the first pulse was streaked by the terahertz field and the second pulse was used as the reference photoelectron spectrum. The actual pulse duration was derived according to the methods described in [31].

FLASH2 is equipped with 12 variable-gap undulator segments, each of 2.5 m length and 31.4 mm period [11]. The pulse duration was measured with the streaking setup while varying the number of undulators contributing to the lasing. The shown data result from 3 different measurement campaigns. In the first one, FLASH2 was set to 3 different wavelengths: 8, 12, and 16 nm with a constant electron bunch energy of 1.00 GeV and an electron bunch charge of 0.19 nC, leading to XUV pulse durations on the order of 100 fs FWHM. For the second campaign, the FLASH2 electron bunch energy was 875 MeV with a bunch charge of 0.2 nC, and the wavelength was set to 10 and 20 nm, leading to XUV pulse durations ranging from 50 to 160 fs FWHM. Besides these two campaigns, the third campaign was performed with a significantly lower electron bunch energy of 434 MeV and an electron bunch charge of 0.2 nC, leading to a wavelength of 34 nm. The experimental results are summarized in Table 1.

Table 1. Main parameters derived from the measurements shown in Figure 3. The values were deduced from scaling the experimental data to the 3D simulation, with z_{sat} as saturation length in "number of undulators" with a maximum number of undulators of 12 at FLASH2, $\tau_{ph}^{min}(FWHM)$ as minimum pulse duration, and E_{sat} as the saturation pulse energy. In order to compare the experimental data to the 1D simulation, the normalized electron pulse duration $\bar{\tau}_{el}$ (equivalent to the number of modes M) was determined for all measured wavelengths using Equation (4), and the coherence time at saturation τ_c^{sat} (FWHM) was taken from Refs. [19,33].

Wavelength	Electron Bunch Energy	z_{sat}	$\tau_{ph}^{min}(FWHM)$	E_{sat}	$\tau_c^{sat}(FWHM)$	$\bar{\tau}_{el}\|M$
8 nm	1008 MeV	9.4	75 fs	60 µJ	7fs	22
10 nm	875 MeV	8.9	50 fs	39 µJ	8 fs	13
12 nm	1008 MeV	7.7	88 fs	88 µJ	9 fs	16
16 nm	1008 MeV	7.0	105 fs	130 µJ	12 fs	16
20 nm	875 MeV	6.1	95 fs	50 µJ	15 fs	13
34 nm	434 MeV	8.3	77 fs	26 µJ	20 fs	8

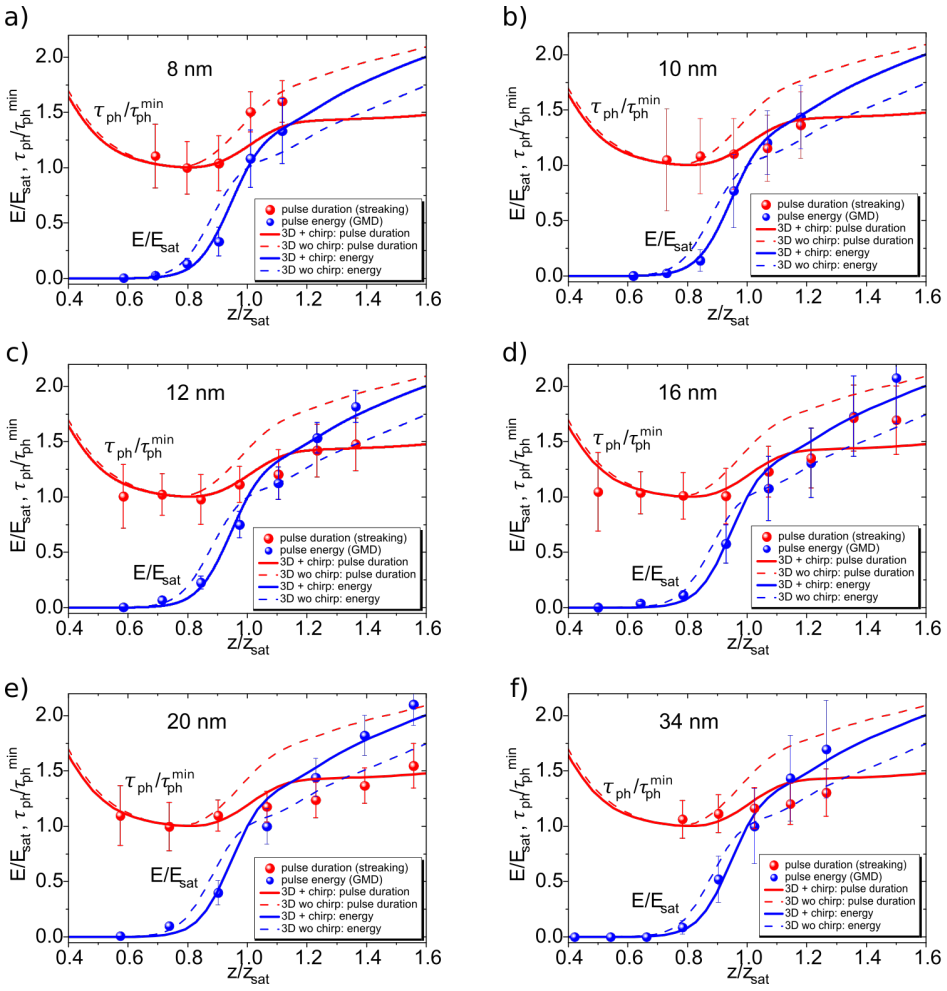

Figure 3. Evolution of the pulse duration (red circles) and pulse energy (blue circles) along the undulators. The actual undulator length z is normalized by the saturation length z_{sat}. The pulse energy is normalized to the saturation energy and the pulse duration to the minimum pulse duration (Equation (4)). The experimental results (shown as points) represent the average over several thousand single pulse measurements and were recorded for FEL wavelengths of 8, 10, 12, 16, 20, and 34 nm and agree very well with the chirped 3D simulations (shown as red and blue solid lines). The 3D simulations without energy chirp (shown as red and blue dashed lines) are showing less agreement with the experimental data. The "error bars" denote not the experimental uncertainty but rather the width of the measured distribution induced by SASE and technical fluctuations to indicate by how much the FEL pulse energy and duration fluctuate during measurement (see also Figure 4).

For all measurements except at 34 nm, the undulators were not tapered (all undulators contributing to the lasing had the same gap settings, i.e., the same K-value), in order to compare the experimental values with the simulations. For each wavelength, the pulse duration was first measured when all 12 undulators were closed (thus, all undulators contributed to the lasing). Afterward, starting with the undulators closest to the experiments, one pair of undulators at a time was opened until no measurable XUV pulse energy could be detected. Since only the downstream undulators were opened, the trajectory in the first (lasing) undulators was kept constant. The resulting shift of the source point of the XUV radiation enlarged the XUV focal spot in the streaking interaction region slightly; however, it was still sufficiently smaller (<300 µm FWHM) as compared to the THz focal spot (∼1 mm FWHM) and did not lead to significant changes for the THz streaking measurements. The energy of the XUV pulses was simultaneously measured with an absolutely calibrated pulse energy detector (GMD) [34] provided by the FLASH photon diagnostic.

4. Discussion

We analyzed the average pulse energies and average pulse durations as well as their respective fluctuations as functions of the number of undulators contributing to the lasing process for six different wavelengths. As a basis, we used the 3D simulation based on the chirped electron bunch. In the first step, the number of undulators was scaled to the undulator coordinate z such that the onset of measurable SASE (>0.5 µJ) coincided with the z range in which the energy gain became visible in the simulated energy gain curve (z/z_{sat}∼0.7). This determined the undulator axis scaling and already fixed the saturation length z_{sat}. It has to be noted that we took into account that the first two undulator segments at FLASH2 hardly contributed to the lasing due to a slight misalignment, and thus for the experimental data we had to count the first two undulators as 0.5 undulators (i.e., subtracting 1.5 from the actual number of closed undulators). The simulation results were not affected by this technical issue. In the second step, the pulse energy was scaled such that the pulse energy at saturation length $z = z_{sat}$ was defined as saturation pulse energy E_{sat} and all energies were normalized by the saturation energy. A similar normalization was applied for the pulse duration. Here, the measured values were scaled to the minimum pulse duration τ_{min} at z/z_{sat}∼0.8. It is important to note that the experimental data have been only rescaled and not fitted to the simulation result.

Figure 3 shows the experimentally measured pulse duration (red spheres) as well as the 3D simulation including chirp (red line) and the 3D simulation without chirp (red dashed lines). The 3D model without chirp predicts a considerable pulse lengthening when the amplification process enters the nonlinear regime (similar to the 1D models shown in Figure 1), while the chirped simulation shows clearly less pulse lengthening. The experimental pulse duration data also do not indicate a strong lengthening of the XUV pulses in saturation and thus show a good agreement with the 3D simulation including chirp. For the pulse energy, we measured a steady increase in saturation and beyond. This behavior is again well represented by the 3D model including chirp, while the 3D model without chirp predicts less energy increase after the saturation point.

The pulse energies as well as the pulse durations were stochastically fluctuating due to the SASE process and fluctuations induced by the acceleration process as well as measurement uncertainties in the actual THz streaking measurement [19], leading to a broad distribution. Example histograms of the fluctuations measured for a specific setting (fixed wavelength and number of undulators) are shown in Figure 4b,d. The rms values of the fluctuations are also used as "error bars" in Figure 3, not denoting the measurement uncertainty but showing the range of the measured values. The actual experimental uncertainty for single-shot measurements was determined to be about ±20% for pulse duration measurements [31] and about ±10% for pulse energy measurements [19]; thus, only a small fraction of the shown "error bars" of the averaged values resulted from measurement uncertainties.

In Figure 4a,c, the normalized fluctuations are presented as functions of z. The fluctuations are not constant along the amplification process and for fewer closed undulators the fluctuations are much larger. Both the 1D and 3D simulations show that for pulse duration and pulse energy the relative fluctuations are largest in the linear regime and are decreasing strongly in the range of z/z_{sat} 0.8 to 1 and only decrease slowly after saturation is reached.

In contrast to the simulated values of the pulse energy and the pulse duration (Figure 1) which are essentially pulse-length-independent, the respective fluctuations are indeed pulse-duration-dependent. We know from Ref. [19] that the fluctuations in pulse duration and pulse energy are inversely proportional to the square root of the number of modes, as is also indicated by the scaling in Figure 1a. Therefore, we expect less fluctuations for longer pulses (i.e., larger numbers of modes), as can be seen in Figure 4a,c. The 1D simulation was calculated for three different mode numbers, while the 3D simulation was only conducted for 5.1 modes, due to the larger computational load. Indeed, the 3D simulation results lay between the 1D simulation for four and eight numbers of modes for the pulse duration fluctuations and in the exponential gain regime for the energy fluctuations. However, it

is important to note that the 3D simulation predicts significantly less energy fluctuations as the 1D simulations in the saturation regime, which we could not verify experimentally due to technical reasons. Since the measured XUV pulse durations were in the range of $\bar{\tau}_{el}$ = 15–20, as shown in Table 1, they have to be compared mainly to the 1D simulation with $\bar{\tau}_{el} = 16$. The experimental values show essentially the same trend as the simulation calculated with, however, significantly higher fluctuations than the simulation predicts for the inherent SASE fluctuations. This observation was already described in [19] and can be attributed to additional fluctuations, including the measurement uncertainties, fluctuations in the energy gain, and compression of the electron bunches (due to acceleration field phase instability).

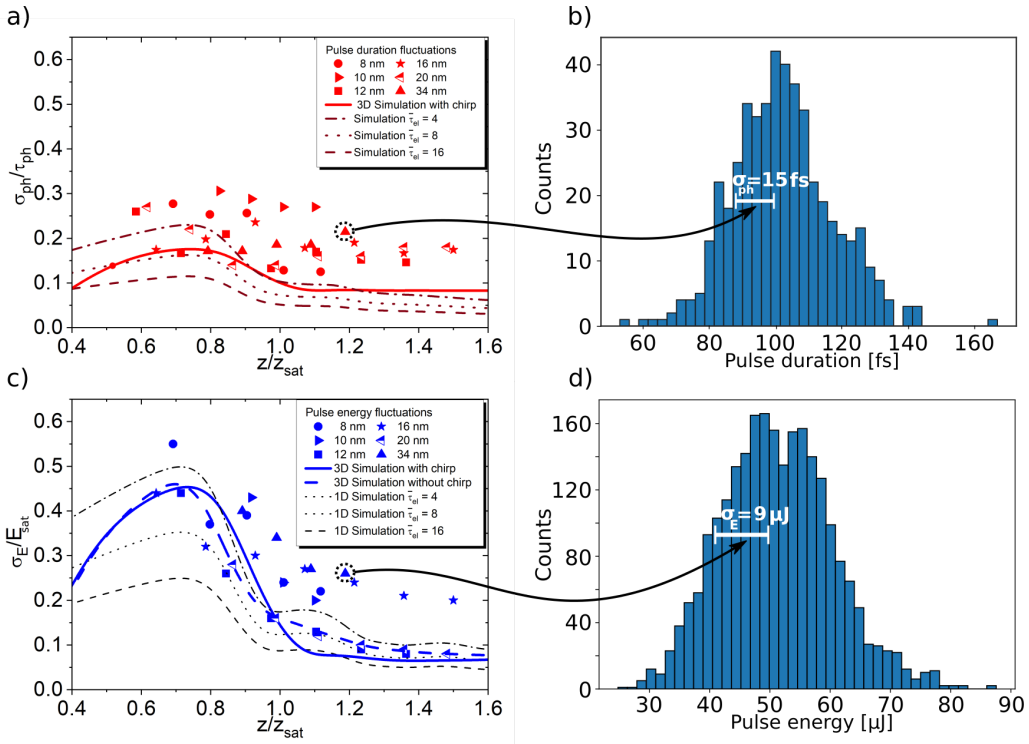

Figure 4. Shown are the fluctuations as functions of the undulator coordinate z for (**a**) the pulse duration and (**c**) the pulse energy. For each setting, several thousand FEL pulses were measured, leading to a broad, Gaussian distribution as shown in (**b**) the pulse duration and (**d**) the pulse energy. The example histograms in (**b**,**d**) are corresponding to the data point shown with the dashed circle. The values for the fluctuations shown are the rms values of the measured pulse energies and pulse durations which are equivalent to the $1/e$ width of the histogram (for the nearly Gaussian distribution). In addition, the theoretically determined values for the fluctuations (only taking the SASE-induced effects into account) are plotted for the chirped and nonchirped 3D simulation and 1D simulation for the cases of $\bar{\tau}_{el}$ = 4, 8, and 16. The fact that the measured fluctuations are larger than the theoretically expected values (only for SASE) can be attributed to measurement uncertainty and additional technical fluctuations in the accelerator, as was discussed in Ref. [19].

An interesting property for experiments is the radiation power (pulse energy divided by the pulse duration). In Figure 5a, we compare how the power scales with z. It turns out that the achievable power of the FEL pulses increases for all experimental settings continuously along the undulators, even in saturation without a hint for a local maximum. The chirped 3D simulation predicts the same behavior and shows a very good agreement with the experimental data. The nonchirped 3D simulation exhibits a similar trend in the linear regime and a small local maximum at the saturation point, which is not reproduced by the experimental data. In contrast, in the 1D simulation, the power reaches a distinct maximum saturation and grows again only for deeply saturated operation. By comparing

the results from the simulation methods, the chirped 3D simulation shows a much better agreement with the experimental data and should be used as a basis for the future prediction of FLASH radiation parameters.

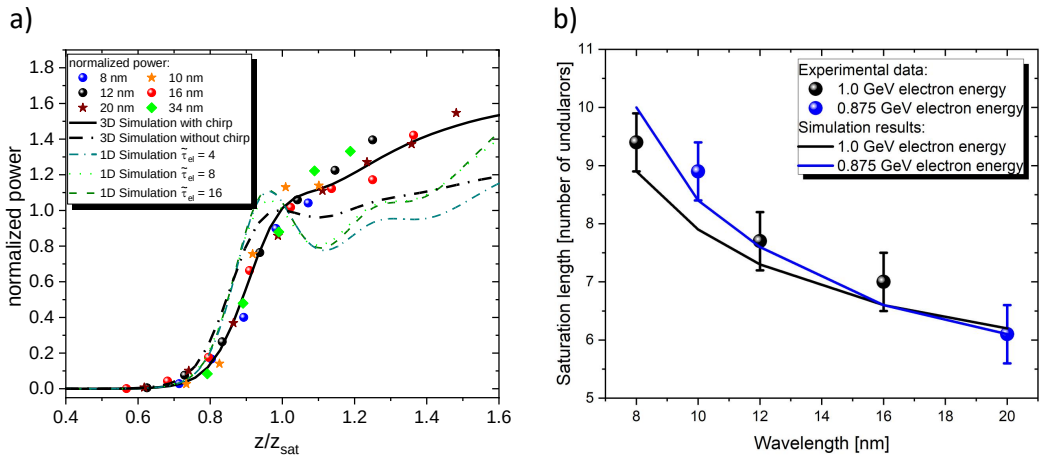

Figure 5. (**a**) Development of the power (pulse energy divided by pulse duration) along the undulators for different pulse durations. The chirped 3D model agrees significantly better with the experimental data as compared to the nonchirped 3D model, while the oscillatory behavior predicted by the 1D model is not reproduced at all. (**b**) The measured as well as the simulated (3D model with chirp) saturation length is plotted as functions of the FEL wavelength for two different FEL setups. Error bars are estimated as ± 0.5 undulators from the analysis. The electron bunch energy for the 34 nm measurement was much smaller than for the other measurements; thus, it is not included in the plot.

Looking at Figure 5, one sees a continuous power increase along the undulator length. However, as pointed out in Refs. [14,15,35], considering the spatial and spectral properties of the FEL beam, it turns out that the maximum brilliance of the radiation is rather achieved in the very beginning of the nonlinear regime. Thus, for experiments that need the highest possible photon densities on the target, it may be beneficial to work close to the saturation point at $z/z_{sat} \sim 1$. Since neither spectral nor spatial measurements have been performed in this study, we cannot test this statement experimentally.

Comparing the FEL parameters (see Table 1) from the data shown in Figure 3, we observed that for the same FEL settings (8 nm, 12 nm, 16 nm and 10 nm, and 20 nm, respectively), the achievable saturation energy E_{sat} increases with longer wavelength [11,36]. The minimal pulse duration ($\tau_{min}(FWHM)$) also increases slightly while the needed number of undulators to achieve saturation (z_{sat}) decreases. Plotting the saturation length as a function of the FEL wavelength together with the results from the chirped 3D simulation (Figure 5b) shows a good agreement. This again points out that the chirped 3D simulation can be used to reliably predict FLASH2 radiation parameters despite the different experimental settings (different electron energies, undulator gaps, and tuning).

5. Conclusions

We investigated FEL pulse duration and pulse energy and their fluctuations as functions of undulator length for six different FEL wavelengths. We compared the simulation results from chirped and nonchirped 3D FEL simulations with 1D FEL simulations. The chirp strengths were chosen such that the typical spectral widths ($\sim$1%) observed at FLASH were matched. Comparing the experimental results measured for different FEL setups with various simulation models, we found a compelling agreement with the chirped 3D model even if the FEL parameters deviated significantly between measurement and simulation. This indicates that the result does not depend strongly on the particular FEL setting. The features predicted by the 1D model and the nonchirped 3D model could not be reproduced.

In contrast, the chirped 3D simulation results describe the behavior of the pulse energy and pulse duration rather accurately for FLASH and can be well used as input for future experiments or comparison to measurements.

Author Contributions: Measurements, M.M.B., S.D., R.I. and I.J.B.M.; Simulation, M.V.Y.; writing—original draft preparation, M.M.B. and S.D.; writing—review and editing, M.M.B., S.D., R.I., I.J.B.M. and M.V.Y. All authors have read and agreed to the published version of the manuscript.

Funding: This research was funded by Deutsche Forschungsgemeinschaft (DFG, German Research Foundation) grant number 491245950.

Institutional Review Board Statement: Not applicable.

Informed Consent Statement: Not applicable.

Data Availability Statement: The data presented in this study are available on request from the corresponding author.

Acknowledgments: We want to acknowledge Franz Kärtner, Mikhail Pergament, Anne-Laure Calendron, Joachim Meier, Martin Kellert, and Simon Reuter for providing and maintaining our regenerative amplifier. We want to thank the DESY Synchronization group (in particular Sebastian Schulz) for providing an excellent synchronization of our laser. We would like to acknowledge Ulrike for useful discussions and suggestions for improving this article. We also thank the FLASH operators, in particular Juliane Rönsch-Schulenburg, for helpful discussions and for fulfilling our special wishes during our beamtimes.

Conflicts of Interest: The authors declare no conflict of interest.

References

1. Saldin, E.L.; Schneidmiller, E.A.; Yurkov, M.V. Self-amplified spontaneous emission FEL with energy-chirped electron beam and its application for generation of attosecond X-ray pulses. *Phys. Rev. ST Accel. Beams* **2006**, *9*, 050702. [CrossRef]
2. Saldin, E.L.; Schneidmiller, E.A.; Yurkov, M.V. Statistical properties of radiation from VUV and X-ray free electron laser. *Opt. Commun.* **1998**, *148*, 383–403. [CrossRef]
3. Behrens, C.; Gerasimova, N.; Gerth, C.; Schmidt, B.; Schneidmiller, E.A.; Serkez, S.; Wesch, S.; Yurkov, M.V. Constraints on photon pulse duration from longitudinal electron beam diagnostics at a soft X-ray free-electron laser. *Phys. Rev. ST Accel. Beams* **2012**, *15*, 030707. [CrossRef]
4. Lutman, A.A.; Ding, Y.; Feng, Y.; Huang, Z.; Messerschmidt, M.; Wu, J.; Krzywinski, J. Femtosecond X-ray free electron laser pulse duration measurement from spectral correlation function. *Phys. Rev. ST Accel. Beams* **2012**, *15*, 030705. [CrossRef]
5. Ackermann, W.A.; Asova, G.; Ayvazyan, V.; Azima, A.; Baboi, N.; Bähr, J.; Balin, V.; Beutner, B.; Brandt, A.; Bolzmann, A.; et al. Operation of a Free Electron Laser in the Wavelength Range from the Extreme Ultraviolet to the Water Window. *Nat. Photonics* **2007**, *1*, 336–342. [CrossRef]
6. Emma, P.; Akre, R.; Arthur, J.; Bionta, R.; Bostedt, C.; Bozek, J.; Brachmann, A.; Bucksbaum, P.; Coffee, R.; Decker, F.J.; et al. First lasing and operation of an ångstrom-wavelength free-electron laser. *Nat. Photonics* **2010**, *4*, 641–647. [CrossRef]
7. Ishikawa, T.; Aoyagi, H.; Asaka, T.; Asano, Y.; Azumi, N.; Bizen, T.; Ego, H.; Fukami, K.; Fukui, T.; Furukawa, Y.; et al. A compact X-ray free-electron laser emitting in the sub-ångström region. *Nat. Photonics* **2012**, *6*, 540–544. [CrossRef]
8. Decking, W.; Abeghyan, S.; Abramian, P.; Abramsky, A.; Aguirre, A.; Albrecht, C.; Alou, P.; Altarelli, M.; Altmann, P.; Amyan, K.; et al. A MHz-repetition-rate hard X-ray free-electron laser driven by a superconducting linear accelerator. *Nat. Photonics* **2020**, *14*, 391–397. [CrossRef]
9. Milne, C.J.; Schietinger, T.; Aiba, M.; Alarcon, A.; Alex, J.; Anghel, A.; Arsov, V.; Beard, C.; Beaud, P.; Bettoni, S.; et al. SwissFEL: The Swiss X-ray Free Electron Laser. *Appl. Sci.* **2017**, *7*, 720. [CrossRef]
10. Ayvazyan, V.; Baboi, N.; Bohnet, I.; Brinkmann, R.; Castellano, M.; Castro, P.; Catani, L.; Choroba, S.; Cianchi, A.; Dohlus, M.; et al. A new powerful source for coherent VUV radiation: Demonstration of exponential growth and saturation at the TTF free-electron laser. *Eur. Phys. J. D* **2002**, *20*, 149–156. [CrossRef]
11. Faatz, B.; Plönjes, E.; Ackermann, S.; Agababyan, A.; Asgekar, V.; Ayvazyan, V.; Baark, S.; Baboi, N.; Balin, V.; Von Bargen, N.; et al. Simultaneous operation of two soft X-ray free-electron lasers driven by one linear accelerator. *New J. Phys.* **2016**, *18*, 062002. [CrossRef]
12. Saldin, E.L.; Schneidmiller, E.A.; Yurkov, M.V. FAST: A three-dimensional time-dependent FEL simulation code. *Nucl. Instrum. Methods Phys. Res. Sect. A Accel. Spectrometers Detect. Assoc. Equip.* **1999**, *429*, 233–237. [CrossRef]
13. Saldin, E.L.; Schneidmiller, E.A.; Yurkov, M.V. *The Physics of Free Electron Lasers*, 3rd ed.; Springer: Berlin, Germany, 1999.
14. Saldin, E.L.; Schneidmiller, E.A.; Yurkov, M.V. Coherence properties of the radiation from X-ray free electron laser. *Opt. Commun.* **2008**, *281*, 1179–1188. [CrossRef]

15. Saldin, E.L.; Schneidmiller, E.A.; Yurkov, M.V. Coherence Properties of the Radiation from X-ray Free Electron Lasers. In Proceedings of the CAS-CERN Accelerator School on Free Electron Lasers and Energy Recovery Linacs, Hamburg, Germany, 31 May–10 June 2018; Volume 1.
16. Bonifacio, R.; Pellegrini, C.; Narducci, L.M. Collective instabilities and high-gain regime in a free electron laser. *Opt. Commun.* **1984**, *50*, 373. [CrossRef]
17. Bonifacio, R.; De Salvo, L.; Pierini, P.; Piovella, N.; Pellegrini, C. Spectrum, temporal structure, and fluctuations in a high-gain free-electron laser starting from noise. *Phys. Rev. Lett.* **1994**, *73*, 70–73. [CrossRef]
18. Schneidmiller, E.A.; Yurkov, M.V. Application of statistical methods for measurements of the coherence properties of the radiation from SASE FEL. In Proceedings of the IPAC2016, Busan, Korea, 8–13 May 2016; p. MOPOW013.
19. Bermudez, I.; Düsterer, S.; Ivanov, I.; Liu, J.; Brenner, G.; Rönsch-Schulenburg, J.; Czwalinna, M.; Yurkov, M. Study of temporal, spectral, arrival time and energy fluctuations of SASE FEL pulses. *Opt. Express* **2021**, *29*, 10491–10508. [CrossRef]
20. Saldin, E.L.; Schneidmiller, E.A.; Yurkov, M.V. Statistical properties of radiation from SASE FEL driven by short electron bunches. *Nucl. Instrum. Methods Phys. Res. Sect. A Accel. Spectrometers Detect. Assoc. Equip.* **2003**, *1–2*, 101–105. [CrossRef]
21. Zagorodnov, I.; Dohlus, M. Semianalytical modeling of multistage bunch compression with collective effects. *Phys. Rev. ST Accel. Beams* **2011**, *14*, 014403. [CrossRef]
22. Mayer, D.; Lever, F.; Picconi, D.; Metje, J.; Alisauskas, S.; Calegari, F.; Düsterer, S.; Ehlert, C.; Feifel, R.; Niebuhr, M.; et al. Following excited-state chemical shifts in molecular ultrafast X-ray photoelectron spectroscopy. *Nat. Commun.* **2022**, *13*, 198. [CrossRef]
23. von Korff, Schmising, C.; Willems, F.; Sharma, S.; Yao, K.; Borchert, M.; Hennecke, M.; Schick, D.; Radu, I.; Strüber, C.; Engel, D.W.; et al. Element-Specific Magnetization Dynamics of Complex Magnetic Systems Probed by Ultrafast Magneto-Optical Spectroscopy. *Appl. Sci.* **2022**, *10*, 7580.
24. Gerth, C.; Brenner, G.; Caselle, M.; Düsterer, S.; Haack, D.; Makowski, D.; Mielczarek, A.; Palutke, S.; Rota, L.; Rybnikov, V.; et al. Linear array detector for online diagnostics of spectral distributions at MHz repetition rates. *J. Synchrotron Rad.* **2019**, *26*, 1514–1522. [CrossRef]
25. Ding, T.; Rebholz, M.; Aufleger, L.; Hartmann, M.; Stooß, V.; Magunia, A.; Birk, P.; Borisova, G.D.; Wachs, D.; da Costa, C.C.; et al. Measuring the frequency chirp of extreme-ultraviolet free-electron laser pulses by transient absorption spectroscopy. *Nat. Commun.* **2021**, *12*, 643. [CrossRef] [PubMed]
26. Frühling, U.; Wiel, M.; Gensch, M.; Gebert, T.; Schütte, B.; Krikunova, M.; Kalms, R.; Budzyn, F.; Grimm, O.; Rossbach, J.; et al. Single-shot terahertz-field-driven X-ray streak camera. *Nat. Photonics* **2009**, *3*, 523–528. [CrossRef]
27. Grguraš, I.; Maier, A.R.; Behrens, C.; Mazza, T.; Kelly, T.J.; Radcliffe, P.; Düsterer, S.; Kazansky, A.K.; Kabachnik, N.M.; Tschentscher, T.; et al. Ultrafast X-ray pulse characterization at free-electron lasers. *Nat. Photonics* **2012**, *6*, 852–857. [CrossRef]
28. Frühling, U. Light field streaking for FELs. *J. Phys. B At. Mol. Opt. Phys.* **2011**, *44*, 243001. [CrossRef]
29. Ivanov, R.; Bermudez, I.; Bidhendi, M.; Brachmanski, M.; Kreis, S.; Bonfigt, S.; Degenhardt, M.; Düsterer, S. Photon diagnostic beamline FL21 at FLASH. *J. Synchrotron Rad.* 2022, *submitted*.
30. Ivanov, R.; Liu, J.; Brenner, G.; Brachmanski, M.; Düsterer, S. FLASH free-electron laser single-shot temporal diagnostic: Terahertz-field-driven streaking. *J. Synchrotron Rad.* **2018**, *25*, 26. [CrossRef]
31. Ivanov, R.; Macias, I.J.; Liu, J.; Brenner, G.; Roensch-Schulenburg, J.; Kurdi, G.; Frühling, U.; Wenig, K.; Walther, S.; Dimitriou, A.; et al. Single-shot temporal characterization of XUV pulses with duration from ∼10 fs to ∼350 fs at FLASH. *J. Phys. B* **2020**, *53*, 184004. [CrossRef]
32. Tiedtke, K.; Azima, A.; Von Bargen, N.; Bittner, L.; Bonfigt, S.; Düsterer, S.; Faatz, B.; Frühling, U.; Gensch, M.; Gerth, C.; et al. The soft X-ray free-electron laser FLASH at DESY: Beamlines, diagnostics and end-stations. *New J. Phys.* **2009**, *11*, 023029. [CrossRef]
33. Roling, S.; Siemer, B.; Wöstmann, M.; Zacharias, H.; Mitzner, R.; Singer, A.; Tiedtke, K.; Vartanyants, I.A. Temporal and spatial coherence properties of free-electron-laser pulses in the extreme ultraviolet regime. *Phys. Rev. ST Accel. Beams* **2011**, *14*, 080701. [CrossRef]
34. Tiedtke, K.; Feldhaus, J.; Hahn, U.; Jastrow, U.; Nunez, T.; Tschentscher, T.; Bobashev, S.V.; Sorokin, A.A.; Hastings, J.B.; Möller, S.; et al. Gas detectors for X-ray lasers. *J. Appl. Phys.* **2008**, *103*, 094511. [CrossRef]
35. Saldin, E.L.; Schneidmiller, E.A.; Yurkov, M.V. Statistical and coherence properties of radiation from X-ray free-electron lasers. *New J. Phys.* **2010**, *12*, 035010. [CrossRef]
36. Faatz, B.; Braune, M.; Hensler, O.; Honkavaara, K.; Kammering, R.; Kuhlmann, M.; Ploenjes, E.; Roensch-Schulenburg, J.; Schneidmiller, E.; Schreiber, S.; et al. The FLASH Facility: Advanced Options for FLASH2 and Future Perspectives. *Appl. Sci.* **2017**, *7*, 1114. [CrossRef]

A.2 Free-Electron Laser Temporal Diagnostic Beamline FL21 at FLASH

Research Article | Vol. 31, No. 12 / 5 Jun 2023 / Optics Express 19146
Optics EXPRESS

Free-electron laser temporal diagnostic beamline FL21 at FLASH

ROSEN IVANOV,[1,2] MAHDI M. BIDHENDI,[1,*] IVETTE J. BERMÚDEZ MACIAS,[1,2] MACIEJ BRACHMANSKI,[1] SVEA KREIS,[1] SUSANNE BONFIGT,[1] MARKUS DEGENHARDT,[1] MARIE-KRISTIN CZWALINNA,[1] MIKHAIL PERGAMENT,[3] MARTIN KELLERT,[3] FRANZ X. KÄRTNER,[3,4] AND STEFAN DÜSTERER[1]

[1]*Deutsches Elektronen-Synchrotron DESY, Notkestr. 85, 22607 Hamburg, Germany*
[2]*Currently with the European XFEL GmbH, Holzkoppel 4, D-22869 Schenefeld, Germany*
[3]*Center for Free-Electron Laser Science CFEL, Deutsches Elektronen-Synchrotron DESY, Notkestr. 85, 22607 Hamburg, Germany*
[4]*Department of Physics, Universität Hamburg, Jungiusstr. 9, 20355 Hamburg, Germany*
[*]*mahdi.mohammadi-bidhendi@desy.de*

Abstract: A beamline for temporal diagnostics of extreme ultraviolet (XUV) femtosecond pulses at the free-electron laser in Hamburg (FLASH) at DESY was designed, built and put into operation. The intense ultra-short XUV pulses of FLASH fluctuate from pulse to pulse due to the underlying FEL operating principle and demand single-shot diagnostics. To cope with this, the new beamline is equipped with a terahertz field-driven streaking setup that enables the determination of single pulse duration and arrival time. The parameters of the beamline and the diagnostic setup as well as some first experimental results will be presented. In addition, concepts for parasitic operation are investigated.

1. Introduction

Free-electron lasers (FELs) working in the extreme ultraviolet (XUV) and X-ray region deliver photon pulses with a duration in the femtosecond (fs) range with unrivaled intensity [1–6]. The majority of X-ray FELs operate in the self-amplified spontaneous emission (SASE) regime, meaning that each pulse is characterized by a unique combination of pulse energy, XUV spectrum, arrival time and pulse duration. The necessity to know the duration and temporal profile of each individual pulse stimulated the development of different methods that are suitable for single-shot temporal characterization. A few years ago, a study was carried out on different temporal diagnostic techniques [7], which led to the decision that field-driven terahertz (THz) streaking fulfills most of the requirements for FLASH compared to other techniques. The THz field-driven streaking technique [8,9] has the potential to deliver single-shot pulse duration information essentially wavelength-independent from XUV to X-rays with a large dynamic range in pulse duration and FEL pulse energy. It can be operated with repetition rates up to several hundred kHz [10] (potentially even MHz) and absorbs only a tiny fraction of the incident photons and can thus be in principle transparent to the XUV beam. In order to investigate the capabilities of THz streaking as well as its limits in more detail and start to establish the technique as a standard diagnostic tool, a dedicated beamline (FL21) was designed, built and commissioned to host permanently a THz streaking setup. Parts of the THz streaking setup described here have already been used in dedicated diagnostic beamlines at FLASH1, exploring the potentials of the technique [11–13]. However, a permanent setup including an own optical laser system generating

#492228 https://doi.org/10.1364/OE.492228
Journal © 2023 Received 11 Apr 2023; revised 8 May 2023; accepted 9 May 2023; published 23 May 2023

Optics EXPRESS

the THz pulses is mandatory to guarantee a stable operation. To allow a parasitic measurement of the pulse duration, a concept has been implemented to extract a small fraction of the FEL beam for the diagnostic setup while the remaining part can still be used by a different experiment.

2. Beamline FL21 at FLASH2

2.1. Concept

To provide a constant THz streaking field and thus reliable data, the FEL beam diameter in the THz streaking setup has to be significantly smaller than the THz focal diameter. In order to achieve the highest streaking fields for good temporal resolution, the THz beam is almost diffraction limited focused to a beam diameter of around 1 mm full width at half maximum (FWHM), which is much smaller than the unfocused FLASH beam (3-10 mm FWHM) in the experimental hall. Thus, it is not possible to install our setup directly in the main beamline without focusing the FEL beam. Our approach is to extract a part of the FEL beam and focus it in order to provide the conditions for a dedicated pulse duration diagnostic. Since there is no standard way to realize a nondestructive XUV beam splitter, we chose a geometry using a "cutting mirror" (moving up-down) that reflects a fraction of the beam to the THz streaking setup while the remaining part of the XUV beam propagates along the beamline similar to concepts used in XUV split and delay units [14–17]. As will be shown in section 4, the temporal properties of the SASE XUV pulse can still be reliably measured, even if only a fraction of the beam is used for the diagnostic.

2.2. Beamline layout

We designed and built the beamline FL21 (scheme in Fig. 1 and details in Fig. 2) consisting of a flat cutting mirror (CM) "splitting" the FEL beam; focusing (toroidal with 1.5m focal distance) mirror (FM); Laser-based THz source, THz streaking setup (TSS) in a laser safety hutch (LSH) and a direct beamline branch for the remaining FEL beam at which additional diagnostics (spectrometer, XUV pulse energy measurement) can be installed for calibration measurements or further developments. Figure 2 presents the detailed drawing of the beamline starting with the Cutting Mirror (CM) mounted in a UHV 160 CF cube on a three-axis motorized manipulator in a 40 CF flange together with an in-vacuum manual two-angle kinematic mount (for pre-alignment). The CM and its mount are designed to cut the XUV beam precisely without parasitic reflections while avoiding unnecessary losses (inset in Fig. 2). For a well-defined cutting edge and to avoid

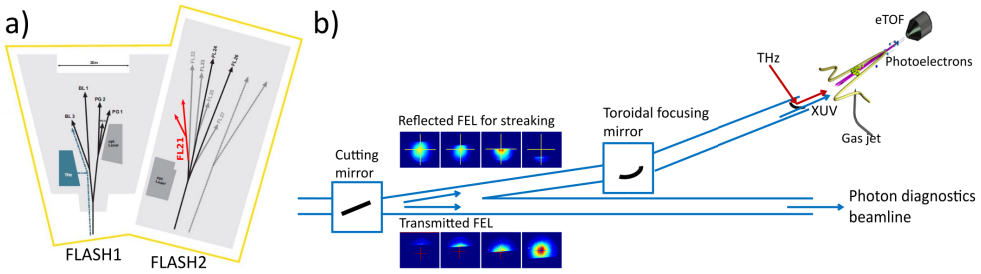

Fig. 1. a) Overview layout of the FLASH1 and FLASH2 experimental halls. The FL21 beamline is indicated in red. b) Top view of the FL21 beamline at FLASH2. The beamline consists of two branches that can share the FEL beam by introducing a cutting mirror. The cutting mirror moves up and down (perpendicular to the shown top view) so that part of the beam can be reflected to the THz streaking setup (upper branch) while the remaining part of the FEL beam propagates straight to an open port beamline dedicated to general photon diagnostic measurements.

Optics EXPRESS

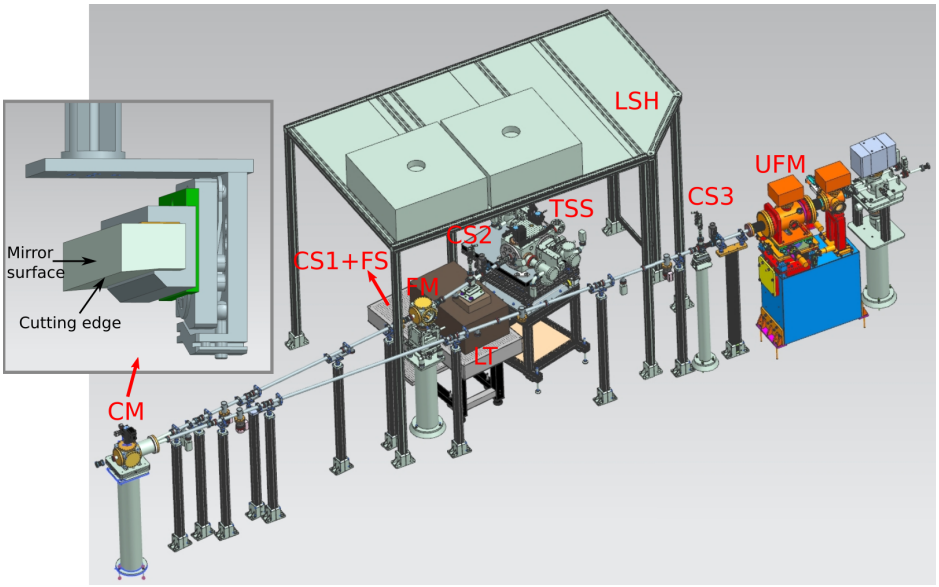

Fig. 2. 3D drawing of the FL21 beamline consisting of a flat cutting mirror (CM), focusing mirror (FM), a laser safety hutch (LSH) for the THz streaking setup (TSS) including a laser-based THz source and a direct beamline branch including a focusing mirror for the remaining FEL beam. The inset shows a drawing of the cutting mirror, showing the specially designed cutting edge and the mirror surface.

reflections on the bottom surface, the lower edge is cut at an angle of 85° thus the mirror can be coated with gold (Au) almost up to the edge (< 0.1 mm). A special mechanical mount had been designed only partially enclosing the mirror such that the lower part remains free to not block the transmitted beam. We did not observe any deformation of the mirror due to the reduced support. Moving the CM vertically we can reflect a fraction of the FEL beam into the THz streaking hutch while the unaffected fraction of the FEL beam propagates on a straight path (outside LSH) and reaches the experimental chamber. The part of the beam that was reflected from CM reaches the focusing mirror (FM) installed in a UHV 160 CF cube mounted on a motorized support that can provide three translational axes and three angle degrees of freedom for alignment. The cutting as well as the focusing mirror are coated with gold (Au) to cover the wavelength range of ~ 7 nm to ~ 50 nm. Both mirrors have a size of 150 x 15 mm, leading to a horizontal "footprint" (clear aperture) of around 10.7 mm at a grazing incidence angle of 4°. The toroidal mirror has a focal distance of 1.5 m and provides a focal spot size of 100 to 200 μm FWHM depending on the FEL parameters. It was verified that the focal spot size does not significantly change for different fractions of the beam reflected by the cutting mirror. The focus position is aligned to be in the interaction point of the THz Streaking setup (TSS). In front (upstream) of the FM chamber a one-axis motorized CF40 manipulator was installed containing a Ce:YAG crystal ($20 \times 20 \times 0.2$ mm) that is monitored by a CCD camera to observe the FEL beam shape (CS1+FS). Additionally, on this manipulator there are four thin metal filters of different materials installed to adjust the pulse energy entering the TSS independently of the straight "uncut" FEL beam. A second CCD camera and Ce:YAG crystal screen (CS2) on a pneumatic mover are installed between FM and TSS. A similar setup CS3 (Ce:YAG screen plus CCD camera) has been installed near the end of the straight branch outside the LSH. Recently, at that position, a focusing mirror (UFM) chamber (previously located at the decommissioned beamline BL2 at FLASH1 [18])

Optics EXPRESS

was installed providing a ~ 20 μm focus (or unfocused beam) dedicated to photon diagnostics measurements.

The initial alignment of all FL21 beamline elements was done using the beamline pilot laser which was aligned with respect to the nominal beam axis of the FEL. With that source and CS1, CS2, CS3 plus an additional TSS interaction point spatial observing system (screen and camera with a variable (up to x12) magnification lens), the beamline elements were aligned and reference beam positions were set. For the FEL operation we use the beamline mirrors located in the FLASH2 accelerator tunnel to align the FEL to our reference positions.

3. Pulse duration diagnostic setup

We first describe the initial setup that was used in several previous measurement campaigns [11–13,19]. In the second part, a recently upgraded version with more electron time-of-flight (eTOF) spectrometers with improved handling is presented.

3.1. Initial setup

The initial pulse duration diagnostic setup consists of an IR laser system, a setup to generate the THz single-cycle pulses and an interaction chamber equipped with an electron spectrometer. The IR laser system, as well as the THz streaking setup (TSS), are placed to confine the laser radiation in a dedicated laser safety hutch (LSH) equipped with a laser interlock system. The actual laser system consists of a commercial oscillator (Onefive ORIGAMI, 1030 nm, 8 nm bandwidth) which is optically synchronized to the FLASH main laser oscillator (MLO) with a sub-10 fs rms jitter [20], and an in-house built regenerative amplifier. The Yb:KYW regenerative amplifier was implemented using a dual-crystal approach to distribute the thermal load and balance the thermal lens in the gain media. The amplifier's dual-crystal cavity enables stable operation over a wide pumping power range and provides a stable output at repetition rates of up to 1000 Hz. Stretching of the seed pulse and compression of the amplified output is accomplished using chirped-volume-Bragg-gratings in the amplifier unit. That ensures the pointing stability of the amplifier's output and makes the design robust and reliable (1030 nm, 3 nm bandwidth 3.5 mJ, 1 ps, 10 Hz) [21]. The single-cycle THz generation based on optical rectification in $LiNbO_3$ utilizing a tilted pulse front (similar to Ref. [11]) was built on the second level of our optical laser table (LT). Here, a diffractive grating with 1500 grooves per mm disperses the IR beam which is imaged by a 4f telescope (focal lengths of 200 mm and 125 mm) onto the $LiNbO_3$ crystal prism. This scheme produces a tilted pulse front satisfying the phase-matching condition for optical rectification and thus efficient THz production with ~ 0.1% THz efficiency [22]. The THz setup is located on a separate small optical breadboard which is connected to the LT and placed near the streaking chamber to minimize the THz optical path in air (~ 55 cm) until it enters the vacuum chamber of the TSS. The THz transport consists of two flat and two 90° off-axis parabolic mirrors (PM). PM1 collimates the THz with a reflective focal length of 6" (152.4mm) and PM2 focuses the THz into the interaction point. PM2 (with focal length of 4" (101.6 mm)) has a 3 mm hole in the middle allowing the FEL beam to overlap collinearly with the THz focus. All THz transport optics are gold coated and only PM2 is located in vacuum. To transmit the THz beam into the TSS a vacuum window consisting of Zeonex 480R polymer is used. The overall THz transport has a clear aperture > 50 mm and a transmission of ~ 90%.

The single-cycle THz pulse has a linear slope of ~ 500 fs (an example shown in Fig. 4), centered at 0.7 THz with a pulse energy of ~ 3 – 4 μJ. The THz generation setup was optimized to produce a high THz field with a steep linear slope (see Fig. 4 a) and d)) in order to increase the streaking resolution for measuring relatively short (<50 fs) SASE FEL pulses. Thus, the THz beam was tightly focused to horizontally 1.2 ± 0.1 mm and vertically 1.5 ± 0.1 mm FWHM (see Fig. 3 c)) observed by a pyroelectric camera (Spiricon Pyrocam III), leading to a field strength of

Optics EXPRESS

up to 150 kV/cm. This focusing geometry leads to a Gouy phase broadening [12,23] of about 15 fs (FWHM) which has to be taken into account for the data analysis.

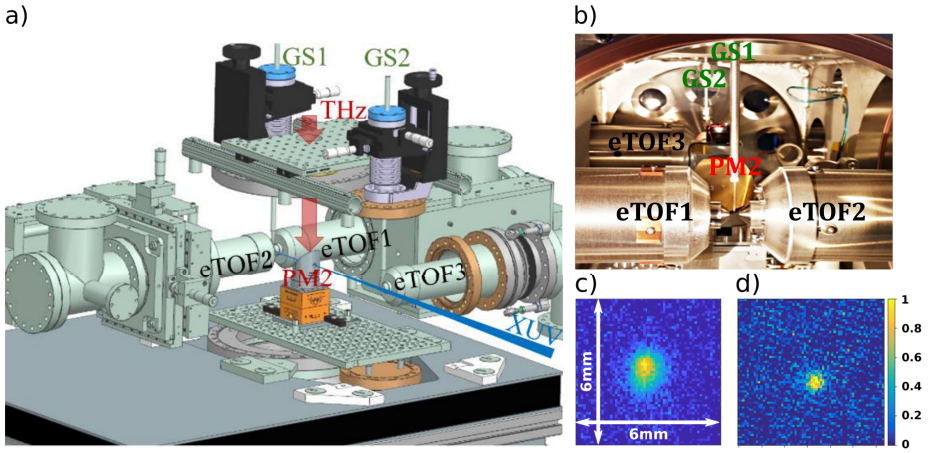

Fig. 3. a) Upgraded THz streaking setup consisting of three eTOFs (vacuum chamber is not visible). b) Picture inside the vacuum chamber showing three eTOFs and two gas sources. c) THz foci measured with a pyroelectric camera. left: initial setup with 1.2 mm x 1.5 mm focus; right: Upgraded setup with 0.9 mm x 0.9 mm focus.

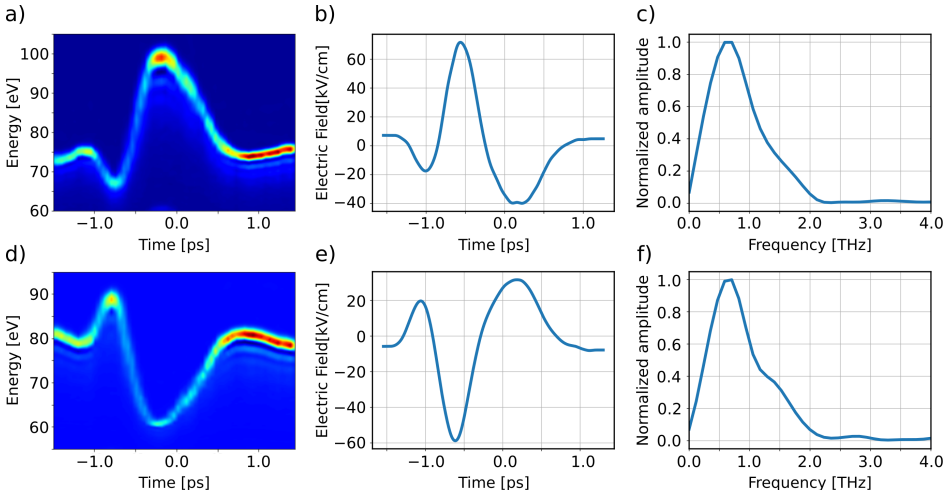

Fig. 4. THz Streaking trace (delay scan) for neon 2p photoelectrons ionized by 13 nm XUV pulses and measured simultaneously by a) eTOF1 and d) eTOF2. The streaking trace is proportional to the vector potential of the THz pulse. The THz electric field was calculated by differentiating the vector potential measured by b) eTOF1 and e) eTOF2. c) and f) show the spectral distribution of the electric field calculated by a Fourier transform for eTOF1 and eTOF2 respectively.

The THz streaking setup (TSS) hosts besides various diagnostics and the gas supply, the THz focusing and the eTOF. The FEL and the THz beam (both with horizontal linear polarization) were overlapped spatially and temporally in the acceptance volume of (~ 0.5 mm^3) of the eTOF (Kaesdorf ETF11) which we define as the interaction point of the TSS. More details on the

Optics EXPRESS

overlap procedure can be found in Ref. [11]. FLASH typically operates in a burst mode, resulting in several hundred XUV pulses with a separation of up to 1 μs with a burst repetition rate of 10 Hz [1]. The THz source on the other hand operates at 10 Hz repetition rate and thus we can only "streak" one FEL pulse in the burst. Using the trigger and synchronization system one can jump easily to different pulses in the FEL burst to successively measure the properties of the pulses along the burst. The advantage of the burst structure is that with the same eTOF one can record for each 10 Hz measurement the "streaked" XUV pulse and "unstreaked" reference pulses that were not altered by the THz field. These "reference pulses" are needed for the analysis, since essentially the pulse duration is encoded in the difference between the streaked and the unstreaked (reference) photoelectron line width (for theoretical explanation see e.g. [8,9,12,23]). Using a second FEL pulse produced only 1 μs later than the streaked one as the reference is a good approach and is used for standard analysis. For pulse durations > 50 fs the widths of the streaked spectra is sufficiently broader than the unstreaked (reference) spectrum and thus one can utilize a different FEL pulse as the reference. The pulse to pulse fluctuation of the unstreaked spectra are sufficiently small. For short pulses < 50 fs the broadening of the streaked pulses is rather small and the reference should be taken from the *same* SASE FEL pulse that is streaked. To be able to acquire such a reference spectrum an additional eTOF located upstream the THz incoupling is needed.

3.2. Upgraded setup

After successful measurements with a streaking setup containing one eTOF, a new chamber containing three eTOFs was build to widen the experimental capabilities. Having two eTOFs in the polarization plane of the THz, but in opposing directions, allows to record simultaneously the streaked photo electron spectra created by the XUV pulse interacting with the same THz field but with opposite sign. This option allows a determination of the resolution of the arrival time measurements (see below) and enables us to characterize statistical errors in the pulse duration measurements as well as the measurement of the single shot chirp of the XUV pulses like discussed in Refs. [8,23].

Recently, such an upgraded THz streaking setup was installed at FL21. The new chamber hosts three eTOF (Fig. 3) and a modified THz incoupling. The new chamber ($310 \times 310 \times 510$ cm) was manufactured from nonmagnetic stainless steel using six 250 CF flanges and additional four 100 CF flanges on its walls. This allows us to mount three eTOFs (side walls), two noble gas sources (top), a THz window (top), a 1000 l/s turbo pump (bottom), several viewports and additional elements. The THz source remained the same, while the THz transport was adapted to the new boundary conditions. The THz is now coupled into the TSS from the top. Essentially the collimating parabola PM1 was changed to a (larger) reflected focal length of 9" (228.6 mm) with 3" clear aperture, leading to a smaller THz focal spot of 0.9±0.1 mm FWHM close to the diffraction limit (Fig. 3). The small focus however increases the Gouy phase induced broadening [12,23] to about 20-25 fs (FWHM), limiting the ability to measure short pulses below 30 fs (FWHM).

Another upgrade enables the remote control of the THz focusing parabola PM2 in the vacuum. The parabola is mounted on top of two motorized goniometers with piezo motors having the center of rotation (± 2.5°) at the position of the hole (for the FEL beam) in the reflective surface (Fig. 3). eTOF1 and eTOF2 are mounted on three-axis UHV 100CF manipulators which enable the precise alignment of the eTOFs to the XUV-THz interaction point. eTOF3 is installed upstream of the interaction region in front of the THz focusing parabola on an adjustable bellow (port aligner). The eTOFs (Kaesdorf ETF11) are differentially pumped by a 300 l/s turbo pump. The gas sources (GS1 and GS2 on Fig. 3) are also supported by three-axis UHV 40CF manipulators and each of them has a motorized gas valve to adjust the gas flow remotely and independently of each other. Typically, a chamber pressure of $1 - 9 \times 10^{-7}$ mbars (for neon) is used for the actual

Optics EXPRESS

measurements. When the gas valves are closed, the pressure of the vacuum chamber is in the 10^{-9} mbar range. The chamber pressure and the FEL pulse energy in the interaction region are adjusted such that enough electrons are created in the acceptance volume of the eTOF to get a sufficiently well-defined eTOF spectrum without leading to space charge effects (for more details see Ref. [12]). Figure 4 a) and d) present "up" and "down" streaked THz delay scans collected with eTOF1 and eTOF2, so-called streaking traces, which are proportional to the THz vector potential. The measurement shows the energy of Ne 2p photoelectrons in eV as a function of the relative delay between the THz and the FEL pulse in ps.

In summary, the upgraded setup allows us to improve and quantify single-shot temporal resolution in the arrival time and pulse duration measurements as well as the evaluation of single-shot chirp measurements. However, since these upgrades are rather recent, the quantification of the improvements that can be gained by using data from the three eTOFs is still explored and will be reported in future publications.

4. Experimental results

4.1. Testing a parasitic measurement scheme

For a standard THz streaking measurement, it is sufficient to reflect and focus only about 1 μJ of the FEL pulse (typically a small fraction of the FEL pulse energy) to the THz streaking setup. This pulse energy allows to determine the pulse duration with typically ± 20% accuracy and the arrival time with few fs accuracy [11,12]. More pulse energy would lead to undesired space charge effects. Thus, the scheme to only use a fraction of the FEL beam (reflected by the cutting mirror introduced above) seems to be applicable for future parasitic operations. It is however a rather complex task to ensure theoretically that the temporal properties of the SASE pulses are comparable throughout the entire beam profile. Most of all if there are more higher-order spatial modes present as is typically the case at FLASH. Thus, we performed several test measurements using different "splitting" ratios to investigate the evolution of the measured pulse duration as a function of the cutting fraction to tackle the problem from the experimental side. For several measurement campaigns we collected experimental data reflecting different fractions of the FEL beam to the THz streaking setup shown in Fig. 5. The parameter range covered the wavelength range from 10 nm to 34 nm, the average pulse energy range of 20 μJ to 300 μJ and the pulse duration range of $\sim$ 50 fs to 300 fs FWHM. In this regime the experimentally measured pulse durations show no clear dependence on the fraction of the FEL beam used.

As pointed out in Ref. [12,19] the number of photoelectrons created in the interaction region has to be within a certain range to get a sufficiently strong signal but no undesired effects like space charge broadening. Thus, to ensure the same experimental conditions for all measurements, the streaking setup was left unchanged during the cutting mirror measurements, while the transmission of a variable XUV attenuator [19] was adapted such that the average number of created photoelectrons was constant for each cutting ratio. The gas attenuator is a 15-meter-long beam pipe filled with noble gases at a pressure of approximately 10^{-2} mbar. The interaction within the attenuator is linear, and no plasma formation occurs. Consequently, no changes in pulse duration are anticipated. To set up the measurement for a certain cutting fraction takes several minutes to half an hour. During this time the FEL parameters may drift and, thus, part of the observed pulse duration variations in Fig. 5 a) may be attributed to these drifts. In addition, it is to note that the error bars shown in Fig. 5 a) are not the measurement uncertainty but the rms width of the measured pulse duration distribution. We also verified that the XUV focal spot stays sufficiently smaller as compared to the THz focus for all cutting ratios.

Thus, we can reliably determine the *average* pulse duration in the measured parameter range by only using about 10 % of the FEL beam or even less. The evaluation shown in Fig. 5 a) considers only the pulse durations averaged over thousands of FEL pulses. To judge if the pulse duration for *single* FEL pulses, determined by measuring only a small fraction of the FEL beam,

Optics EXPRESS

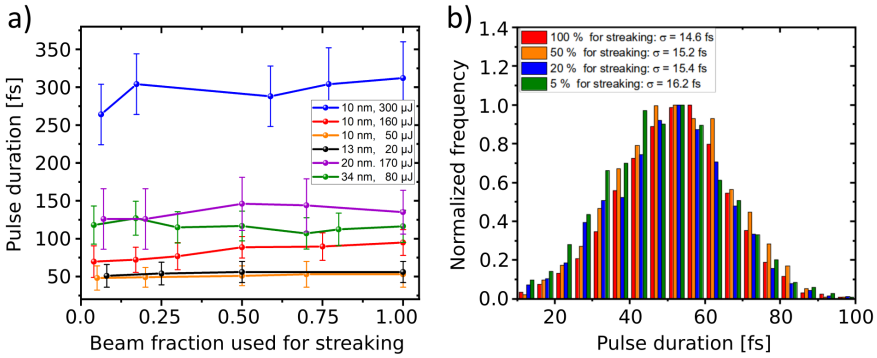

Fig. 5. Inserting the cutting mirror partially into the FEL beam (see Fig. 1) only part of the FEL beam is used for the pulse duration measurement. a) The plot shows the average pulse duration over few 1000 FEL pulses (points) and the rms width of the measured pulse duration distribution as error bars for various different FEL settings. We find no significant difference between the pulse duration determined with 10% of the FEL beam and larger fractions of the FEL beam. The observed small variations of the average pulse duration may also result from changes in the FEL during the lengthy measurement. b) The normalized pulse duration distributions of a few 1000 FEL pulses for several cutting ratio are shown. The histograms display pulse-resolved data from the 10 nm/ 50 fs (orange) measurement in plot a). Since the distribution is almost identical for the different cutting ratios, we infer that the pulse duration for a single FEL pulse measured on a fraction of the FEL beam resembles the pulse duration for the complete beam well. Part of the shown results were presented in [24]

is equivalent with the pulse duration of the complete beam is indeed much more challenging and can not be answered directly with the present setup. However, looking at the pulse duration distribution determined for different cutting ratios as displayed in Fig. 5 b), we do not see a large difference in the shape and width of the distributions. We interpret this as strong indication that also on a single shot basis the assumption that the pulse duration measured in only a fraction of the beam profile holds for the complete pulse is applicable. Here, clearly more experimental as well as simulation effort is needed to explore the approach in more detail and in particular for even shorter (few or single mode beams) FEL pulses.

4.2. Pulse duration measurements for users

Recently, we also started to support FLASH2 users on-demand with information about the FEL pulse temporal characteristics. Here we can provide the average pulse duration, the distribution of the XUV pulse duration and some information about a potential frequency chirp. Such a measurement could be carried out before and after a measurement campaign. Unfortunately, since FL21 has up to now no parasitic cutting mirror in the main beamline (see Fig. 1 a)), the measurement is not online and requires the switching of the entire XUV beam from the user beamline into FL21. Such a measurement usually takes about 2 hours. According to our experience during user beamtimes, when the FEL operates in a stable manner, there are only slight drifts in the pulse duration. It is planned to move the whole streaking setup upstream and incorporate the cutting mirror into the main beamline, such that the THz streaking measurements can be performed online with as little disturbance of the users as possible. A Python-based online analysis tool is developed that provides the temporal properties of the XUV pulses to operators (still in progress).

Optics EXPRESS

4.3. XUV arrival time measurements

The THz streaking setup is primarily designed to measure the XUV pulse duration. However, it can also determine the XUV arrival time with respect to the THz field. Since the IR laser producing the THz is well synchronized to FLASH MLO, we can compare the XUV arrival time to the electron bunch arrival time measured by the bunch arrival time monitor (BAM) [25], located in the acceleration section of the FEL.

For the THz streaking, the change of the mean photoelectron energy of the streaked pulse is proportional to the relative arrival time between the FEL XUV pulse and the THz slope [9,11,20]). The oscillator of the streaking laser is synchronized very well with a remaining jitter of only 5 − 10 fs rms via an optical cross correlator to FLASH MLO [20]. However, slow drifts by environmental changes (mainly temperature and air pressure) are accumulated during the amplification process. The regenerative amplifier [21] adds several tens of meters of path for the IR radiation during the amplification. This path is up to now not temporally stabilized (e.g. by a cross correlation between the amplified pulse and the oscillator) and thus slow temporal drifts of the amplified laser pulse in respect to the oscillator timing are present on a few minute scale. We corrected these slow drifts (± 30 fs) by using the drift stabilized BAM as reference and subtracting the difference between the two arrival time measurements from the streaking signal using a 5-min window averaging.

The electron bunch arrival time is measured by the BAM more than 200m upstream the FL21 endstation after the first accelerator modules at the location of the second bunch compressor (4DBC3) [20,25]. Here, the electron bunch arrival time is measured with an electro-optical method, utilizing directly the laser pulses from the drift-stabilized optical synchronization system, with a precision of typically 5 fs rms and no additional drifts are expected. The information about the electron arrival time is continuously measured for each FEL pulse and is available for user experiments. This data can be used to correct the arrival time during the data analysis and thus improve the temporal resolution of pump-probe experiments [26,27]. Our results emphasize that the arrival time measured by the BAM detectors is indeed extremely well correlated to the arrival time of the XUV photons, despite the large distance between BAM and experimental endstations. In addition, the arrival time information measured by the BAM can be used for a feedback acting on the accelerator to stabilize the electron bunch timing in respect to FLASH MLO [20,28].

Figure 6 presents BAM and THz streaking data from a long-term arrival time measurement for ~ 50000 FEL pulses acquired during ~ 80 minutes. The FEL was operating with 3 electron bunches spaced by 1 μs at a burst repetition rate of 10 Hz. The first bunch was streaked, while the two following pulses served as (unstreaked) reference. The electron bunches had a kinetic energy of 1.1 GeV and a bunch charge of 0.24 nC, resulting in XUV pulses at a wavelength of 10 nm (124 eV) and an average pulse energy of 160 μJ with an average pulse duration of ~ 100 fs (FWHM). The XUV photon (red dots) and electron (blue dots) arrival times are plotted on a shot-to-shot basis as well as 10 sec averaging using a second order Savitzky-Golay filter (red and blue lines) to illustrate the arrival time drifts. The first 60 minutes of the measurement were recorded with a "slow" arrival time feedback activated. Typically, an averaging window of 5 seconds is used in the slow feedback. Here, the arrival time fluctuation within the 60 min period was measured to be 24 fs rms by the BAM and 22 fs rms by the THz streaking. The slight difference may be attributed to the drift correction. For the last 20 minutes the feedback was switched off and one can see larger drifts of the arrival time yielding a larger widths of the arrival time distribution of 34 fs rms for BAM and 33 fs rms measured with the THz streaking. The corresponding histograms of the arrival times are plotted in Fig. 7 a) and d).

Comparing the two measurements by eye shows that the arrival time measured by streaking follows excellently the arrival time measured by the BAM. A comprehensive analysis of the arrival time data shows an rms deviation between the two methods of only 6 fs for the 10-second averaged data and a correlation width for the single shot analysis of 12-13 fs rms for the complete set of

Optics EXPRESS

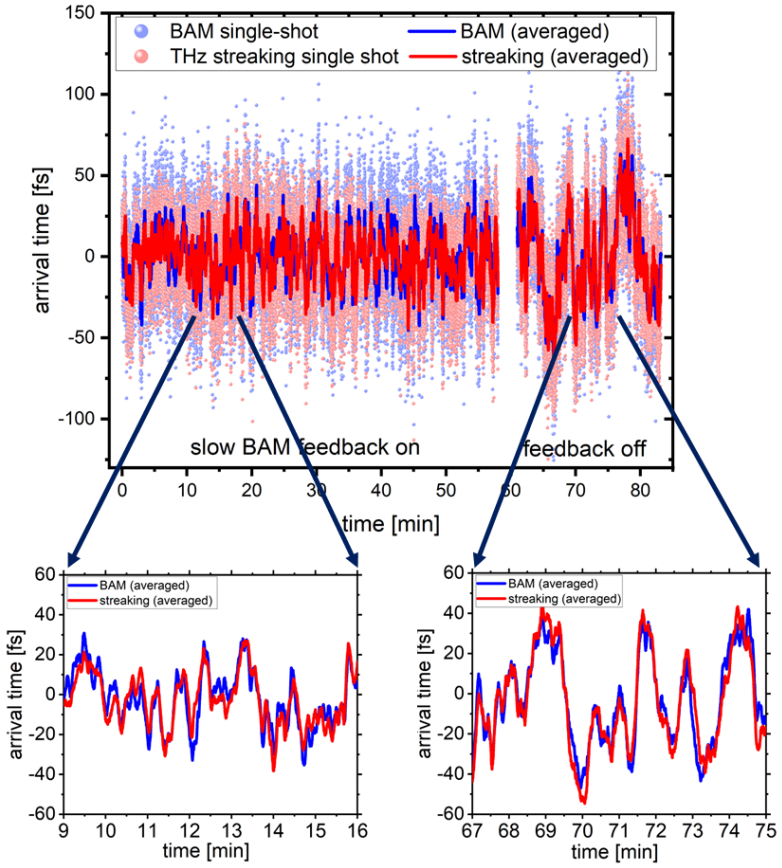

Fig. 6. Long-term measurement of the arrival time of ~ 50000 FEL pulses recorded by THz streaking and BAM. The single pulse arrival time is shown for the XUV photons (red dots) and the electron bunches (blue dots). The red and blue lines indicate a 10-second (100 pulses) averaging to illustrate the arrival time drifts. During the first 60 minutes of the measurement the "slow BAM feedback" is used to correct the arrival time of the accelerator, while for the last 20 minutes the feedback was switched off. The small figures at the bottom reveal in a zoomed view the good agreement of the 10 sec averaged measurement. More analysis is shown in Fig. 7.

data as shown in Fig. 7. This is most of all remarkable since there is a long list of possible jitter sources involved: Oscillator synchronization, THz streaking measurement uncertainty, BAM measurement uncertainty, SASE generation itself which leads to intrinsic timing fluctuations and possibly more unknown jitter sources. An elaborated explanation of measurement uncertainties using THz streaking can be found in [12]. Looking at the jitter budged in detail we can quantify the influence of some sources. For the BAM, the noise level of the measurement is continuously monitored and delivers ~ 5 fs rms measurement uncertainty. For the THz streaking, we have the uncertainty contribution of the synchronization of the laser oscillator with ~ 7 fs rms and the actual THz streaking measurement. Here, we have statistical fluctuations of the line shape (and thus fluctuations of the center of mass) by the limited number of electrons. This, one can estimate by comparing the difference in the arrival time measured by eTOF1 and eTOF2, resulting in an arrival time resolution of the streaking measurement of $5 - 10$ fs rms depending on the FEL settings. In addition FEL wavelength fluctuations and fitting errors account to about 4 fs rms.

Optics EXPRESS

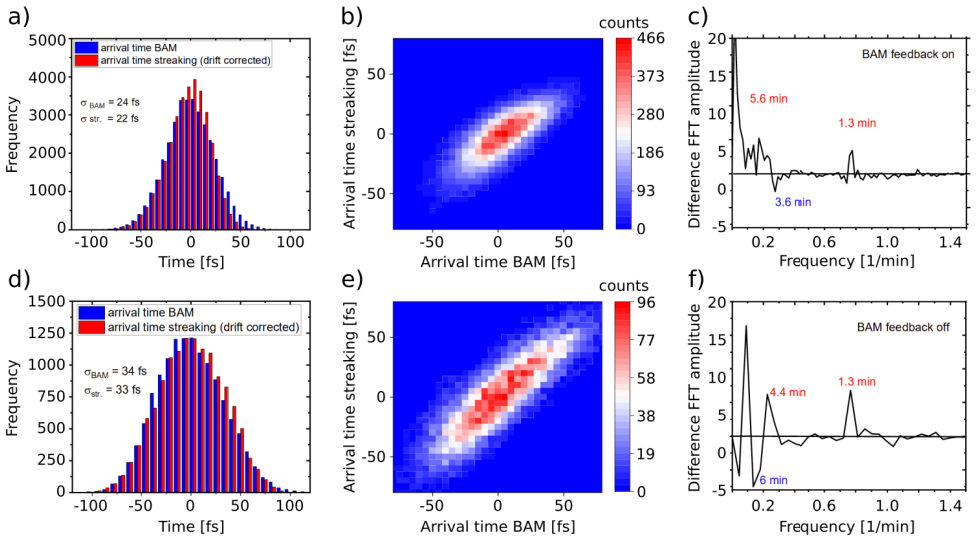

Fig. 7. Analysis of the arrival time data shown in Fig. 6. The upper row (a,b,c) shows the data with the arrival time feedback on, while the feedback was switched off for the lower row (d,e,f). a) and d) show the histograms of the arrival times measured with the BAM (blue) and the THz streaking(red). In addition the rms width of the histograms is displayed. b) and e) show the correlation plots of the arrival times measured with the BAM and THz streaking. The correlation width are only 12 fs rms for feedback on (b) and 13 fs rms (e) for feedback off. Finally, c) and f) present the difference of Fourier transformations (FFTs) of the arrival time data from BAM and THz Streaking (not drift corrected) indicating to individual sources causing the drifts. Positive peaks indicate deviations due to the THz streaking setup and negative are related to the BAM

Finally, the SASE induced arrival time fluctuations are predicted to be on the order of 4 fs rms for the given experimental FEL parameters following the equations in Ref. [13]. Adding up the known uncertainties quadratically according to the propagation of errors (since they result from independent sources) we end up at the measured 12-13 fs rms deviation between THz streaking and BAM, leaving little room for additional unknown jitter sources. Still, the knowledge of the various error sources limiting the arrival time measurements is of great importance to increase the time resolution for pump-probe experiments and will be further tackled by future measurement campaigns.

Besides the fast shot to shot jitter, slower arrival time drifts yield important information as well. To further investigate the temporal drifts, a fast Fourier transform (FFT) of the measurement results of both methods has been performed. Figure 7 c) and f) shows the difference of the FFTs. Thus, positive peaks indicate deviations caused by the THz streaking setup and negative are related to the BAM. Several distinct frequencies can be detected. The peak at 1.3 minutes in the THz streaking measurement can be referred to regulation cycles resulting from the chiller that stabilizes the temperature of the aluminum breadboard of the laser amplifier. What happens at the other peaks is still a subject of discussion. With this example, we want to show that our streaking setup can be used additionally for the characterization of different FEL diagnostics and subsystems.

Optics EXPRESS

5. Conclusion

FL21 at FLASH2, a new beamline for photon diagnostic developments, has been designed, built and commissioned. The beamline consists of two branches that can share the XUV radiation using a cutting mirror. With this mirror one can define the splitting ratio between the THz streaking branch and the straight section used as open port beamline including a focusing mirror. The FL21 THz streaking setup is a stand alone XUV pulse duration diagnostic setup with a dedicated optical laser system, THz generation and a photoelectron eTOF spectrometer chamber. This permanent setup allows long-term systematic studies of temporal properties of SASE radiation for various FEL settings. The well characterized installation also allows pulse duration measurements on rather short notice for user experiments. We showed that there is an excellent correlation between the arrival time measured by BAM (located 200 m upstream the experimental endstations) and the actual arrival time of the XUV photon pulse, highlighting that the BAM measurements can be used to enhance the temporal resolution for user pump-probe experiments. Pulse duration measurements using different fractions of the FEL pulse for the measurement show, that the concept to use a "cutting mirror" allows a virtually parasitic online diagnostic in future. The experimental results support the assumption that the pulse duration measured from a small part of the FEL beam holds for the complete pulse.

In general, a permanently installed, well characterized and easy-to-use pulse duration setup can be used efficiently to determine SASE properties (like the pulse duration along the undulator [19] or Chirp), 2-color operation [29], pulse duration of FEL harmonics, or moreover use the setup to investigate atomic physics e.g. [30,31].

Acknowledgments. We want to acknowledge Anne-Laure Calendron, Joachim Meier, and Simon Reuter (DESY, XFEL) for their support and help regarding the regenerative amplifier. We also want to thank the DESY Synchronization group (in particular Sebastian Schulz) for providing an excellent synchronization of our laser. We would like to acknowledge Kai Tiedke (DESY) for useful discussions and suggestions for improving this article. In addition we acknowledge the help of Luca Poletto and Paolo Miotti (CNR-IFN) for their support in designing the XUV beamline optics. We also thank the FLASH operators for helpful discussions and for fulfilling our special wishes during our beamtimes.

Disclosures. The authors declare no conflicts of interest.

Data Availability. The data presented in this study are available on request from the corresponding authors.

References

1. W. Ackermann, G. Asova, and V. Ayvazyan, *et al.*, "Operation of a free-electron laser from the extreme ultraviolet to the water window," Nat. Photonics **1**(6), 336–342 (2007).
2. P. Emma, R. Akre, and J. Arthur, *et al.*, "First lasing and operation of an ångstrom-wavelength free-electron laser," Nat. Photonics **4**(9), 641–647 (2010).
3. T. Ishikawa, H. Aoyagi, and T. Asaka, *et al.*, "A compact X-ray free-electron laser emitting in the sub-ångström region," Nat. Photonics **6**(8), 540–544 (2012).
4. W. Decking, S. Abeghyan, and P. Abramian, *et al.*, "A MHz-repetition-rate hard X-ray free-electron laser driven by a superconducting linear accelerator," Nat. Photonics **14**(6), 391–397 (2020).
5. C. J. Milne, T. Schietinger, and M. Aiba, *et al.*, "Swissfel: The swiss x-ray free electron laser," Appl. Sci. **7**(7), 720 (2017).
6. I. S. Ko, H.-S. Kang, and H. Heo, *et al.*, "Construction and Commissioning of PAL-XFEL Facility," Appl. Sci. **7**(5), 479 (2017).
7. S. Düsterer, M. Rehders, and A. Al-Shemmary, *et al.*, "Development of experimental techniques for the characterization of ultrashort photon pulses of extreme ultraviolet free-electron lasers," Phys. Rev. Spec. Top.–Accel. Beams **17**(12), 120702 (2014).
8. U. Frühling, M. Wieland, M. Gensch, T. Gebert, B. Schütte, M. Krikunova, R. Kalms, F. Budzyn, O. Grimm, J. Rossbach, E. Plönjes, and M. Drescher, "Single-shot terahertz-field-driven X-ray streak camera," Nat. Photonics **3**(9), 523–528 (2009).
9. I. Grguraš, A. R. Maier, C. Behrens, T. Mazza, T. J. Kelly, P. Radcliffe, S. Düsterer, A. K. Kazansky, N. M. Kabachnik, Th. Tschentscher, J. T. Costello, M. Meyer, M. C. Hoffmann, H. Schlarb, and A. L. Cavalieri, "Ultrafast X-ray pulse characterization at free-electron lasers," Nat. Photonics **6**(12), 852–857 (2012).
10. P. L. Kramer, M. K. R. Windeler, M. K. R. Windeler, K. Mecseki, E. G. Champenois, M. C. Hoffmann, and F. Tavella, "Enabling high repetition rate nonlinear THz science with a kilowatt-class sub-100 fs laser source," Opt. Express **28**(11), 16951–16967 (2020).

Optics EXPRESS

11. R. Ivanov, J. Liu, G. Brenner, M. Brachmanski, and S. Düsterer, "FLASH free-electron laser single-shot temporal diagnostic: terahertz-field-driven streaking," J. Synchrotron Radiat. **25**(1), 26–31 (2018).
12. R. Ivanov, I. J. B. Macias, J. Liu, G. Brenner, J. Roensch-Schulenburg, G. Kurdi, U. Frühling, K. Wenig, S. Walther, A. Dimitriou, M. Drescher, I. P. Sazhina, A. K. Kazansky, N. M. Kabachnik, and S. Düsterer, "Single-shot temporal characterization of XUV pulses with duration from ~10 fs to ~350 fs at FLASH," J. Phys. B: At., Mol. Opt. Phys. **53**(18), 184004 (2020).
13. I. J. B. Macias, S. Düsterer, R. Ivanov, J. Liu, G. Brenner, J. Rönsch-Schulenburg, M. K. Czwalinna, and M. V. Yurkov, "Study of temporal, spectral, arrival time and energy fluctuations of sase fel pulses," Opt. Express **29**(7), 10491–10508 (2021).
14. F. Sorgenfrei, W. F. Schlotter, T. Beeck, M. Nagasono, S. Gieschen, H. Meyer, A. Föhlisch, M. Beye, and W. Wurth, "The extreme ultraviolet split and femtosecond delay unit at the plane grating monochromator beamline PG2 at FLASH," Rev. Sci. Instrum. **81**(4), 043107 (2010).
15. M. Sauppe, D. Rompotis, and B. Erk, *et al.*, "XUV double-pulses with femtosecond to 650ps separation from a multilayer-mirror-based split-and-delay unit at FLASH," J. Synchrotron Radiat. **25**(5), 1517–1528 (2018).
16. M. Wöstmann, R. Mitzner, T. Noll, S. Roling, B. Siemer, F. Siewert, S. Eppenhoff, F. Wahlert, and H. Zacharias, "The XUV split-and-delay unit at beamline BL2 at FLASH," J. Phys. B: At., Mol. Opt. Phys. **46**(16), 164005 (2013).
17. M. Dreimann, F. Wahlert, D. Eckermann, F. Rosenthal, S. Roling, T. Reiker, M. Kuhlmann, S. Toleikis, M. Brachmanski, R. Treusch, E. Plönjes, B. Siemer, and H. Zacharias, "The soft X-ray and XUV split-and-delay unit at beamlines FL23/24 at FLASH2," J. Synchrotron Radiat. **30**(2), 479–489 (2023).
18. A. A. Sorokin, A. Gottwald, A. Hoehl, U. Kroth, H. Schöppe, G. Ulm, M. Richter, S. V. Bobashev, I. V. Domracheva, D. N. Smirnov, K. Tiedtke, S. Düsterer, J. Feldhaus, U. Hahn, U. Jastrow, M. Kuhlmann, T. Nunez, E. Plönjes, and R. Treusch, "Method based on atomic photoionization for spot-size measurement on focused soft x-ray free-electron laser beams," Appl. Phys. Lett. **89**(22), 221114 (2006).
19. M. M. Bidhendi, I. J. Bermudez Macias, R. Ivanov, M. V. Yurkov, and S. Düsterer, "Fel pulse duration evolution along undulators at flash," Appl. Sci. **12**(14), 7048 (2022).
20. S. Schulz, I. Grguraš, C. Behrens, H. Bromberger, J. T. Costello, M. K. Czwalinna, M. Felber, M. C. Hoffmann, M. Ilchen, H. Y. Liu, T. Mazza, M. Meyer, S. Pfeiffer, P. Prędki, S. Schefer, C. Schmidt, U. Wegner, H. Schlarb, and A. L. Cavalieri, "Femtosecond all-optical synchronization of an X-ray free-electron laser," Nat. Commun. **6**(1), 5938 (2015).
21. A.-L. Calendron, H. Çankaya, and F. X. Kärtner, "High-energy khz yb:kyw dual-crystal regenerative amplifier," Opt. Express **22**(20), 24752–24762 (2014).
22. J. Hebling, G. Almási, I. Z. Kozma, and J. Kuhl, "Velocity matching by pulse front tilting for large-area thz-pulse generation," Opt. Express **10**(21), 1161–1166 (2002).
23. U. Frühling, "Light-field streaking for FELs," J. Phys. B: At., Mol. Opt. Phys. **44**(24), 243001 (2011).
24. I. J. Bermudez Macias, "Free electron laser pulse characterization by THz streaking," Doctoral dissertation, University of Hamburg, (2022).
25. A. Angelovski, M. Kuntzsch, M. K. Czwalinna, A. Penirschke, M. Hansli, C. Sydlo, V. Arsov, S. Hunziker, H. Schlarb, M. Gensch, V. Schlott, T. Weiland, and R. Jakoby, "Evaluation of the cone-shaped pickup performance for low charge sub-10 fs arrival-time measurements at free electron laser facilities," Phys. Rev. Spec. Top.–Accel. Beams **18**(1), 012801 (2015).
26. D. Mayer, F. Lever, and M. Gühr, "Data analysis procedures for time-resolved x-ray photoelectron spectroscopy at a SASE free-electron-laser," J. Phys. B: At., Mol. Opt. Phys. **55**(5), 054002 (2022).
27. E. Savelyev, R. Boll, and C. Bomme, *et al.*, "Jitter-correction for IR/UV-XUV pump-probe experiments at the FLASH free-electron laser," New J. Phys. **19**(4), 043009 (2017).
28. B. Lautenschlager, L. Butkowski, M. Czwalinna, B. Dursun, M. Hierholzer, S. Pfeiffer, H. Schlarb, and C. Schmidt, *Arrival Time Stabilization at Flash Using the Bunch Arrival Corrector Cavity (BACCA)* (JACOW Publishing, Geneva, Switzerland, 2021).
29. E. Schneidmiller, I. J. Bermudez Macias, M. Beye, M. Braune, M. K. Czwalinna, S. Düsterer, B. Faatz, R. Ivanov, U. F. Jastrow, M. Kuhlmann, J. Rönsch-Schulenburg, S. Schreiber, A. Sorokin, K. Tiedtke, M. Yurkov, and J. Zemella, "Two-Color Operation of a Soft X-ray FEL with Alternation of Undulator Tunes," Appl. Sci. **13**(1), 67 (2022).
30. I. J. B. Macias, S. Düsterer, R. Ivanov, U. Frühling, and N. M. Kabachnik, "Post-collision interaction effect in THz-assisted Auger decay of noble gas atoms," J. Phys. B: At., Mol. Opt. Phys. **54**(8), 085601 (2021).
31. I. J. B. Macias, I. P. Sazhina, R. Ivanov, S. Düsterer, and N. M. Kabachnik, "Time-dependent post-collision-interaction effects in THz-field-assisted Auger decay," Phys. Rev. A **104**(5), 053102 (2021).

A.3 Determination of the XUV Frequency Chirp at the Free-Electron Laser FLASH via THz Streaking and Electron Beam Diagnostics

photonics

MDPI

Article

Determination of the XUV Frequency Chirp at the Free-Electron Laser FLASH via THz Streaking and Electron Beam Diagnostics

Mahdi M. Bidhendi [1,*], Gesa Goetzke [1], Ivette J. Bermudez Macias [1,†], Rosen Ivanov [1,†], Evgeny A. Schneidmiller [1], Najmeh Mirian [1,‡] and Stefan Düsterer [1]

Deutsches Elektronen-Synchrotron DESY, Notkestr. 85, 22607 Hamburg, Germany; gesa.goetzke@desy.de (G.G.); ivette.bermudez@xfel.eu (I.J.B.M.); rosen.ivanov@xfel.eu (R.I.); evgeny.schneidmiller@desy.de (E.A.S.); mirian81@hzdr.de (N.M.); stefan.duesterer@desy.de (S.D.)

* Correspondence: mahdi.mohammadi-bidhendi@desy.de

† Current address: European XFEL GmbH, Holzkoppel 4, D-22869 Schenefeld, Germany.

‡ Current address: Helmholtz-Zentrum Dresden-Rossendorf, Bautzner Landstr. 400, 01328 Dresden, Germany.

Abstract: Free-electron lasers (FELs) operating in the extreme ultraviolet (XUV) and X-ray regions deliver ultrashort pulses with unprecedented intensity, enabling groundbreaking research across various scientific disciplines. A potential chirp (frequency change within the pulse) of these pulses influences their spectral properties, directly impacting the experimental outcomes and FEL performance. The accurate characterization of the chirp is, therefore, important for optimizing FEL operation and interpreting experimental results. This study presents a comprehensive comparison of two techniques determining the chirp of the XUV pulses at FLASH by directly measuring the XUV pulses with THz streaking and by detecting the chirp of the electron bunches by a Transverse Deflection Structure (PolariX TDS) to infer the XUV chirp. We conducted simultaneous measurements using both techniques at FLASH2 while tuning the FEL to produce various energy chirps on the electron bunch.

Keywords: free-electron lasers; temporal diagnostic; XUV pulses; SASE; THz streaking

Citation: Bidhendi, M.M.; Goetzke, G.; Bermudez Macias, I.J.; Ivanov, R.; Schneidmiller, E.A.; Mirian, N.; Düsterer, S. Determination of the XUV Frequency Chirp at the Free-Electron Laser FLASH via THz Streaking and Electron Beam Diagnostics. *Photonics* **2024**, *1*, 0. https://doi.org/

Received: 5 November 2024
Revised: 4 December 2024
Accepted: 5 December 2024
Published:

1. Introduction

Free-electron lasers (FELs) operating in the extreme ultraviolet (XUV) and X-ray regions deliver photon pulses with femtosecond (fs) durations and unparalleled intensity. These pulses typically range from several hundred femtoseconds down to just a few femtoseconds, with photon counts between 10^{11} and 10^{13} per pulse [1–6]. Most XUV and X-ray FELs operate in the self-amplified spontaneous emission (SASE) regime, resulting in each pulse exhibiting a unique combination of pulse energy, XUV spectrum, arrival time, pulse duration, and chirp. Therefore, it is critical to perform temporal characterization of the pulses on a shot-by-shot basis for proper interpretation of the experimental data.

Traditional photodetectors lack the necessary response time to operate in the few-femtosecond regime, and time–frequency correlation techniques commonly used in the optical domain are difficult to implement due to the small cross-sections in nonlinear processes at X-ray wavelengths. This necessitates the development of advanced methods for single-shot temporal characterization of FEL pulses.

Several diagnostic techniques have been devised to study the temporal properties of FEL pulses [7]. One effective method for single-shot characterization is the THz streaking technique, which is typically used to measure the pulse duration of the XUV pulses [8–10]. However, by extending the technique, one can infer the linear part of the frequency chirp across the XUV pulses [8,11,12].

Another complementary approach involves measuring the longitudinal phase space of the electron bunch, producing the XUV SASE radiation, using an X-Band Transverse Deflection Structure (PolariX TDS) [13,14]. The PolariX TDS, in combination with an

electron beam energy spectrometer, can be used to determine the time–energy distribution of the electron bunches. In addition, the setup allows for determining which part of the electron bunch contributed to the XUV SASE pulse [15] and, thus, allows for estimating a possible frequency chirp of the XUV pulse.

In FEL experiments, usually a potential chirp is not considered as an important parameter, while the analysis of previous THz streaking and TDS data shows that the XUV pulses at FLASH are typically chirped. For many applications, the influence of chirp is rather small, while it can influence other areas noticeably, for example, in femto-chemistry where the chirp can even be used to alter the pathway of the chemical reactions [16–18]. Another consequence of a chirped electron bunch is a broader bandwidth of the XUV pulse. By tilting the electron bunch in the time–energy domain, additional electron energies contribute to the lasing process, leading to a broader XUV spectrum. Looking, e.g., for absorption spectroscopy [19–21] or X-ray crystallography [22], a broad spectrum allows for covering larger ranges of spectral lines or diffraction patterns in a single FEL pulse without lengthy scanning of the FEL wavelength and, thus, speeding up data acquisition. Here, a chirp is rather advantageous.

In this paper, we focus on measuring the linear chirp of the XUV pulses from FLASH2 [23], using THz streaking and PolariX TDS as the only two diagnostic techniques at FLASH, which are potentially able to determine the chirp. Each method offers unique advantages for characterizing the temporal properties of XUV pulses. By comparing these techniques, we aim to provide comprehensive insights into their effectiveness and applicability to optimize the FEL performance and interpret the experimental results.

2. Experimental Techniques

2.1. THz Streaking

To determine the pulse duration and linear part of the chirp of the XUV FEL pulses, we employed the THz streaking technique [8,9]. This method involves using a noble gas target photoionized by the FEL pulses. The resulting photoelectrons carry the temporal and spectral properties of the ionizing XUV radiation. As these photoelectrons propagate through the time-varying electric field of the co-propagating THz radiation, their kinetic energy distribution is influenced by the field. This distribution is then measured by an electron time-of-flight (eTOF) spectrometer.

The momentum component of the photoelectrons changes depending on the time of ionization relative to the THz field. If the electron wave packet is short compared with the period length of the THz field, the temporal structure of the electron wave packet is mapped onto the kinetic energy distribution of the emitted photoelectrons, allowing for the determination of the pulse duration and linear chirp [11].

The THz streaking setup featured an interaction chamber where the XUV and THz beams were focused co-linearly at the interaction point [24]. This point was monitored by two eTOFs positioned opposite each other, perpendicular to the propagation direction of the XUV pulses, as shown in Figure 1a. The second eTOF was installed to allow the simultaneous measurement of photoelectrons created by the XUV FEL pulse interacting with the same THz field, but with opposite momentum shifts. A dedicated laser system provided ∼1 ps long pulses at 1030 nm, with a pulse energy of ∼3.5 mJ and a repetition rate of 10 Hz. These laser pulses generate THz radiation through optical rectification using a nonlinear crystal ($LiNbO_3$). Details can be found in the following references [10,24,25].

By varying the delay between the THz field and the XUV pulse, the photoelectron spectra (often called "streaking trace") are recorded, which represent the vector potential A_{streak} of the THz field [11]. As the THz field is polarized in the plane of the two eTOFs, one eTOF records an upshift in the energy, while the other measures a reduced energy. The streaking traces for both eTOFs are shown in Figure 1b. The "first" slope corresponds to the initial interaction of the THz field with photoelectrons, while the "second" slope follows as the THz field continues interacting with the photoelectrons, as illustrated in Figure 1b. In this setup, the photoelectrons are streaked by a large fraction of the THz pulse.

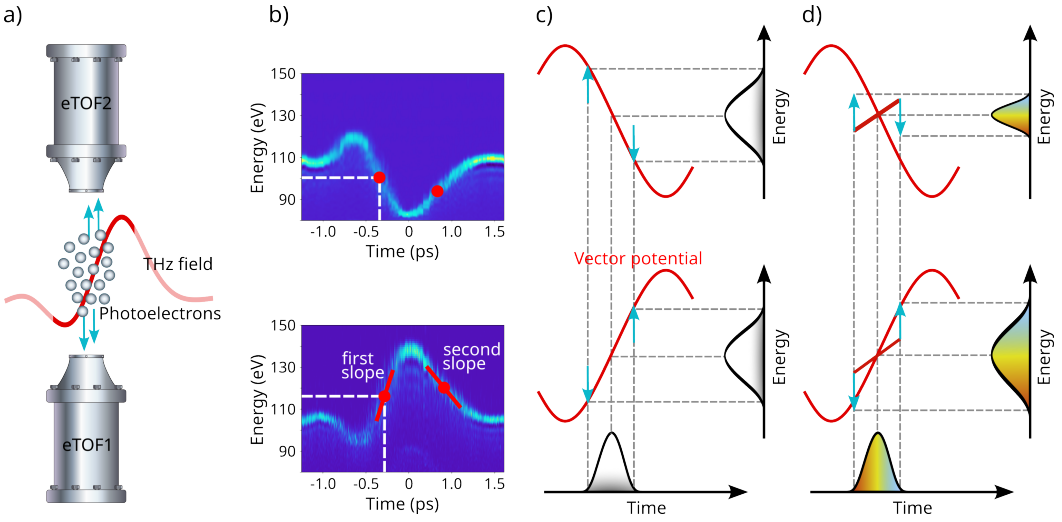

Figure 1. (**a**) Schematic representation of the chirp measurement using the THz streaking setup. Photoelectrons are generated due to the photoionization of gas atoms by the XUV FEL pulse. The kinetic energy of the photoelectrons is modified by the THz field and subsequently measured by eTOF1 and eTOF2. (**b**) The photoelectron spectra (Neon 2p line) for eTOF1 (bottom) and eTOF2 (top) are shown as the a delay scan of the THz field leading to the so-called "streaking trace", which is proportional to the vector potential of the THz field. The red lines show the so-called "first" and "second" slope of the streaking field, and red points indicate the delay value between the FEL and THz pulse of the middle of the linear part of the streaking trace where the streaking data are measured. (**c**) Mapping the temporal information of an unchirped XUV pulse onto the kinetic energy distribution of photoelectrons. The spectral broadening measured by both eTOFs is identical, indicating zero XUV chirp. (**d**) Mapping the temporal information of a negative linearly chirped XUV pulse (higher energy at the head of the pulse represented as blue and lower energy later represented as red) onto the kinetic energy distribution of photoelectrons. For the spectrum measured by eTOF1 (bottom row), the XUV chirp accelerates the fast photoelectrons further and decelerates the slower ones more, resulting in a larger spectral broadening compared with an unchirped XUV pulse. In contrast, for the spectrum measured by eTOF2, the chirp counteracts the streaking field by decelerating the fast photoelectrons and accelerating the slower ones, leading to reduced spectral broadening.

The difference between the up- and down-shifted streaking spectra yields information to determine the linear part of the chirp of the XUV pulse [11]. Setting the delay between the XUV pulse and the streaking field to the center of the linear part of the THz field (red dot in Figure 1b, the slope of A_{streak} is positive for eTOF1 and negative for eTOF2. As illustrated in Figure 1c, the width of the streaked spectrum remains unaffected by the sign of the streaking field for a pulse with no XUV chirp. This results in identical spectral broadening measured by both eTOFs. Thus, the actual pulse duration can easily be determined as $\tau_{XUV} = \sqrt{\sigma_{\text{TOF}}^2 - \sigma_{\text{ref}}^2} \big/ s_{\text{TOF}}$, where σ_{TOF} is the spectral width measured by eTOF1 or eTOF2, σ_{ref} is the spectral width of the unstreaked photoelectrons, and s_{TOF} is the slope of the THz field or the so-called streaking speed, which is calculated by fitting the linear part of the streaking trace as shown in Figure 1b.

In contrast, for a linearly chirped XUV pulse, as shown in Figure 1d the "induced" chirp of the streaking field and the inherent XUV chirp add up or counteract. In the shown case for a negatively chirped XUV pulse (high-energy photoelectrons at the head and low-energy at the tail), the faster electrons generated at the beginning of the pulse are decelerated, while the slower electrons generated at the end of the pulse are accelerated for eTOF2. This causes eTOF2 to measure a streaked spectrum that is narrower than that of an unchirped XUV pulse, whereas eTOF1 records a broader streaked spectrum. This difference can be used to determine a linear approximation of the chirp of XUV pulses, while higher orders of the chirp can unfortunately not be reliably reconstructed with this method. This,

however, also implies that in the case of a chirped XUV pulse, the different broadening of the streaked spectra leads to a more complicated determination of the pulse duration. Under certain conditions, more advanced techniques capable of measuring higher-order chirp can be employed to overcome these limitations, as discussed in [26].

In the streaking trace shown in Figure 1b, we observed that the energy of photoelectrons measured at the center of the linear slopes on eTOF1 and eTOF2 differ slightly (red dots in Figure 1b). In addition, due to the asymmetric shape of the THz field, the streaking speeds at the first and second slope are different. Therefore, the spectral broadening measured on the first and second slopes of the THz field for a single eTOF differs. To account for these differences, the streaking speed and reference width are determined for each eTOF independently, leading to Equations (1) and (2). Assuming that the streaked spectrum maintains a Gaussian shape, the XUV pulse duration can be written as [12]:

$$\tau_{XUV} = \sqrt{\frac{(\sigma_1^2 - \sigma_{\mathrm{ref},1}^2)s_2 + (\sigma_2^2 - \sigma_{\mathrm{ref},2}^2)s_1}{(s_1 + s_2)s_1 s_2}}, \tag{1}$$

where σ_1 and σ_2 are the spectral widths measured by eTOF1 and eTOF2 consecutively, $\sigma_{\mathrm{ref},1}$ and $\sigma_{\mathrm{ref},2}$ are the spectral widths measured in the absence of the streaking field with eTOF1 and eTOF2, respectively. s_1 and s_2 are the streaking speeds measured by eTOF1 and eTOF2, respecitvely. In addition, the difference in the streaked widths can be used to obtain information about the linear part of the XUV chirp:

$$c = \frac{(\sigma_1^2 - \sigma_{\mathrm{ref},1}^2)s_2^2 - (\sigma_2^2 - \sigma_{\mathrm{ref},2}^2)s_1^2}{4s_1 s_2 (s_1 + s_2)\tau_{XUV}^2}. \tag{2}$$

Here, two eTOFs provide the invaluable advantage that the needed two measurements can be acquired simultaneously for each streaked FEL pulse. If only one eTOF is available, one still could obtain an estimate of the chirp and the correct pulse duration, when one measures sequentially the broadening on the first slope and then on the second slope (see Figure 1b and Ref. [12]).

2.2. PolariX TDS

The PolariX TDS [27,28], installed downstream of the undulators at FLASH2, offers direct access to the longitudinal and energy distribution of electron bunches. The setup consists of an X-band RF deflector and a dipole magnet acting as an energy spectrometer. The longitudinal current distribution of the electron bunch traveling through the PolariX TDS is first mapped linearly to a transverse one using the X-band RF deflector. The electron bunch is then energetically dispersed by the dipole magnet. If the TDS streak direction and the dipole bending direction are perpendicular, this setup allows for mapping of the longitudinal phase-space density, thereby enhancing the operational capabilities for optimizing the longitudinal bunch parameters that are crucial for the FEL process [13]. As the TDS is installed downstream of the undulators, it measures the phase space after the SASE process has created intense XUV pulses. This has two important consequences, namely, that one can indeed monitor with the TDS exactly the same FEL pulse that is detected with the THz streaking (for SASE every pulse is different) and by analyzing the TDS trace, one can reconstruct which part of the electron pulse was actually lasing.

In the lasing part, the electrons lose energy (which is transferred into the XUV pulse) and the energy spread increases. Figure 2a,b show images acquired by PolariX TDS for a single electron pulse. Especially in Figure 2a, one can see in the center part that the energy distribution is much wider compared to the ends, indicating the enhanced energy spread and the electrons in this part have less energy. By analyzing the image in detail and comparing it to a reference where no SASE process took place, it is possible to infer the shape of the ultrashort XUV photon pulses [15]. Here, we only concentrate on the determination of the lasing part of the electron bunch.

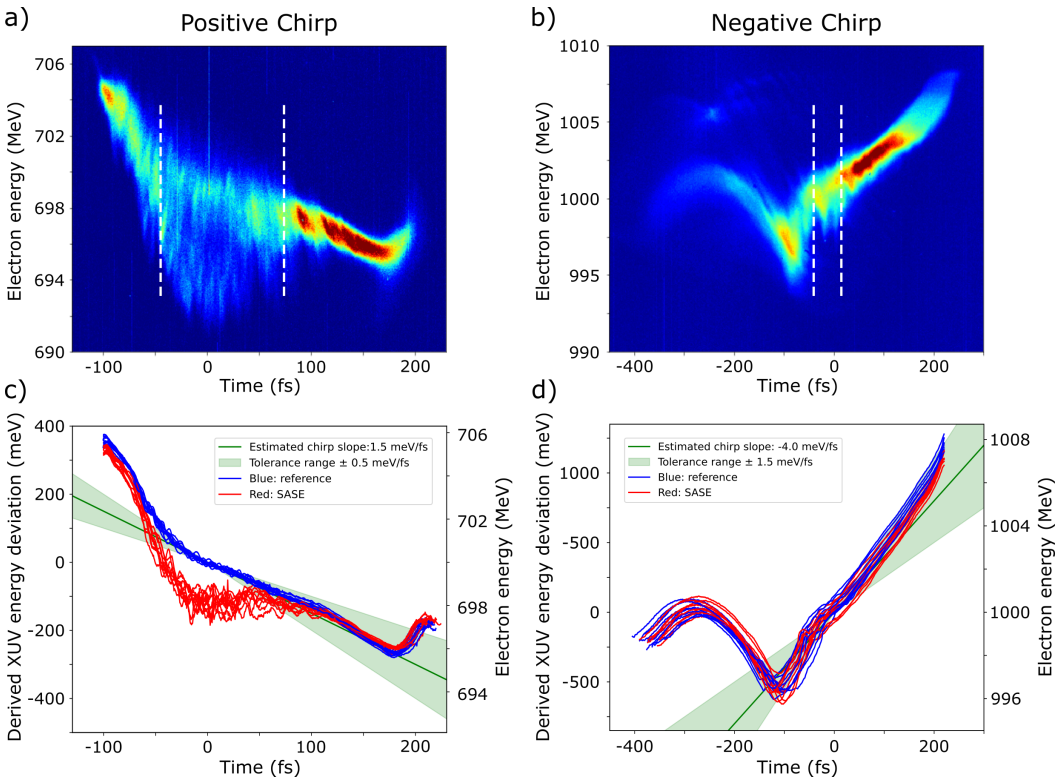

Figure 2. (**a**) A single-shot longitudinal phase space image measured with PolariX, showing a positive energy chirp (low-energy electrons are at the head of the bunch and high-energy electrons are at the tail) on the electron bunch. The white dashed lines show the lasing range on the bunch. (**b**) A single-shot longitudinal phase space image measured with PolariX, showing a negative energy chirp on the electron bunch. (**c**) Computed center of gravity of the phase space images for several images of the FEL setting shown in (**a**). Lasing-on (red) as well as lasing-off (blue) condition is shown. Lasing took place in the ranges where the red and blue curves deviate. The energy chirp of the electron bunch is calculated from a large number of lasing-off measurements and the averaged value is shown as a green line. The green shaded area ("fluctuation range") indicates the variation of the linear fits. (**d**) Center of gravity analyzed for the phase space images with negative chirp as exemplary shown in (**b**). Here, the lasing was rather weak, leading to only a small modulation of the electron bunch. In addition for this setting we find a much larger variation of the slopes fitted to the lasing part as compared to the positive setting.

The effect of an energy chirp on the SASE FEL operation was studied in [29,30], where the so-called energy chirp parameter was introduced. When this parameter is large, it can significantly suppress the FEL gain and should be compensated by a linear undulator taper [30]. In our experiments, the chirp parameter was relatively small, so that the effect on the FEL gain was weak, therefore, no chirp-taper compensation was necessary. The only essential effect of the chirp in the electron beam was photon pulse chirping. For constant undulator settings, the electron energy directly determines the wavelength λ of the FEL pulse as

$$\lambda \propto \frac{1}{\gamma^2}, \tag{3}$$

with the relativistic γ factor representing the electron energy [31].

As the electron pulse energy distribution is strongly modified by the SASE process (at least for XUV pulse energies exceeding 100 µJ), it is difficult to determine an energy chirp from the lasing pulse. Thus, one needs to look at the electron pulse before the lasing sets in to obtain a reliable energy distribution of the electron bunch, influencing the wavelength distribution of the XUV pulse and, thus, determining the chirp. To suppress lasing, a steerer magnet in front of the undulator section is used to slightly deviate the electron bunch

from the lasing trajectory, thus prohibiting lasing but not significantly altering the overall energy distribution.

Figure 2c,d show the center of gravity of the electron bunch calculated from the TDS images for lasing-on and lasing-off conditions. Each red curve represents the center of gravity of a lasing electron bunch with a setup similar to the one shown in Figure 2a,b. The blue curve represents the center of gravity of a non-lasing electron bunch measured separately.

The linear energy chirp of the electron bunch is determined from the lasing-off center of gravity curves by linearly fitting the range where the lasing takes place. Using the independently measured central wavelengths of the XUV pulses and the scaling of Equation (3), we can map the electron energy chirp (in MeV/fs, right axis in Figure 2c,d) to the XUV frequency chirp expressed in meV/fs (left axis). The green line in Figure 2c,d shows the mean value of the linear fits from a large number of analyzed shots, quantifying the electron bunch's initial energy chirp. The green shaded area, referred to as the "fluctuation range" shows the spread of slopes taken from the linear fits.

Since the PolariX results are also influenced by the spatial distribution of the electron bunch, two measurements of opposing streaking field were conducted and the determined XUV chirp (Figure 3a) is the average of the two measurements. For the presented measurements there were only small differences visible, pointing to a not strongly spatially tilted electron bunch.

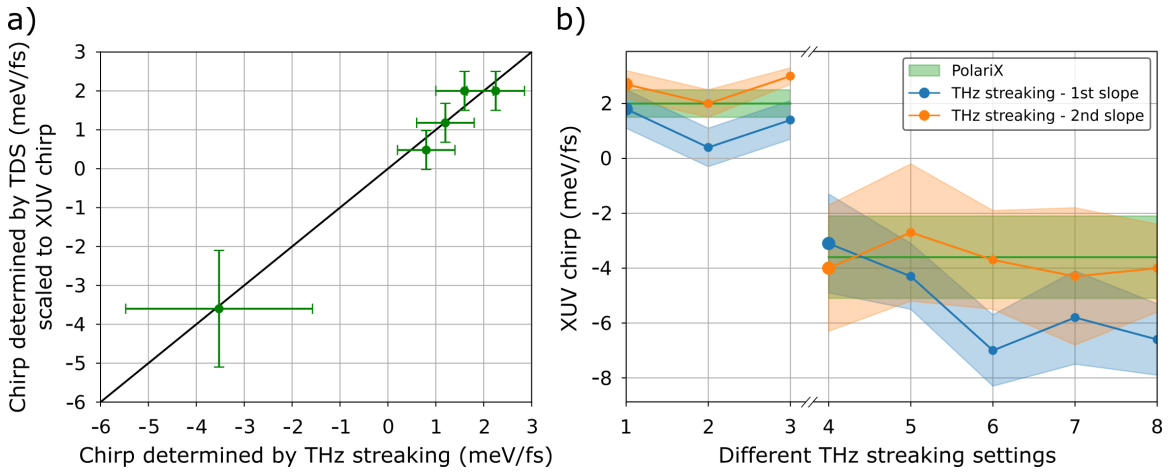

Figure 3. (**a**) Summary of chirp measurements. The linear XUV chirp measured by THz streaking agrees well with the predicted XUV chirp derived from the electron bunch chirp. The shown values are the average and the respective fluctuations of several thousand single shot measurements, simultaneously measured by THz streaking and PolariX TDS. (**b**) Investigation of the influence of the measured chirp values on different settings in the THz streaking setup. The energy resolution of the eTOFs, THz field strength and the number of created photoelectrons were changed significantly. The assignment of the numbers to the different settings is explained in the text. The chirp calculated from TDS data is marked by a green line, with the fluctuation range indicated by a green shade. For the XUV chirp measured using THz streaking, orange denotes the values measured at the second slope and blue, the first slope. Data points 1 and 4 are highlighted with larger points, as they are measured with the standard operation settings of the THz streaking setup. Smaller data points are measured for unfavorable settings.

The next section presents a detailed comparison between the XUV chirp measured using THz streaking and the corresponding XUV chirp calculated from PolariX data. This comparison provides insights into the pros and cons of these measurement techniques.

3. Discussion

The FEL was tuned to several different electron energy chirps with positive as well as negative chirp. For each configuration, single-shot data were acquired simultaneously

using THz streaking and PolariX TDS. To ensure that the XUV chirp measured by THz streaking was independent of the streaking setup parameters, several parameters of the THz detection system were systematically varied, and data were collected for each configuration.

Two different settings of the accelerator were used to cover a larger range for the measurements. Firstly, FLASH2 was operated at an electron bunch energy of ∼1.0 GeV and an electron bunch charge of ∼0.20 nC. This resulted in XUV pulses with ∼16 nm (77 eV) and a pulse duration of ∼80 fs with ∼40 µJ average per FEL pulse for the negative chirp and ∼180 fs with ∼300 µJ for the positive chirp. Secondly, FLASH2 had an electron bunch energy of ∼0.7 GeV and the electron bunch charge was set to 0.26 nC. This configuration resulted in XUV pulses at ∼28 nm (44 eV) with pulse durations around 120 fs and ∼140 µJ pulse energy.

In order to generate a positive chirp (low-energy electrons were at the head of the bunch and high-energy electrons were at the tail), the initially strongly positively chirped electron pulse is under-compressed in magnetic chicanes. To obtain a negative chirp, we had to go to the over-compression regime. We tried to linearize the longitudinal phase space by compensating nonlinearities due to the RF curvature and collective effects in the FLASH accelerator. As the latter are typically strong at FLASH, perfect compensation was not possible, as one can see in Figure 2b. In principle, the chirp can be made larger than what we used in our measurements by compressing the beam stronger. However, collective effects (especially longitudinal space charge) become too strong adding much larger nonlinearities, and can even reverse the sign of the linear part. In this space-charge-dominated regime, the energy chirp at FLASH can exceed our measurements by one or two orders of magnitude due to the short time scale (few femtoseconds) [32]. This regime, however, cannot be studied with the diagnostics described in this paper.

Figure 3a presents the average values of the chirps including the measured fluctuation range indicated by the error bars. The chirp determined by THz streaking (horizontal axis) ranges from −4 meV/fs to 2 meV/fs, meaning that per fs the central energy de- or increases by few meV. Considering a 2 meV/fs chirp for the 180 fs long XUV pulse at 77 eV photon energy, we obtain an energy change of about 0.36 eV within the FWHM of the pulse. Superimposed with the natural FLASH2 bandwidths of about 0.5% [1], we end up at the measured bandwidth of ∼0.7%. The energy changes of the electrons in the accelerator monitored by PolariX were scaled to the expected changes in the XUV pulse, as described above. Despite the different measurement techniques, we obtained a rather good agreement of the measured chirp values for several different settings of FLASH2. This supports the assumption that both diagnostics can be effectively used to determine the chirp of the XUV SASE pulses, at least in its linear part.

For the two extreme cases of positive and negative chirp, a more detailed investigation was conducted. Here, we looked at the dependence of the chirp determined by the THz streaking on different settings of the THz detection setup without altering the FEL pulse intentionally. The aim was to see how sensitive the results of the THz streaking depend on the specific streaking setting and to what extent we can deviate from optimal streaking conditions and still provide reliable chirp measurements. For all measurements we looked at the "first" as well as the "second" slope of the THz field, as shown in Figure 1b. To alter the streaking conditions, the electron spectrometer resolution, the signal level (including space charge effects), and the THz field strength were changed.

In Figure 3b, the blue data points represent the average XUV chirp measured with photoelectrons streaked by the first slope of the THz field, while orange data points show the average XUV chirp value measured with photoelectrons streaked by the second slope. The blue and orange shaded areas indicate the statistical distribution of the XUV chirp measurements for each streaking setup configuration. The green shaded areas show the XUV chirp derived from the electron bunches using PolariX.

Data point **(1)** was measured with optimum streaking conditions (maximum streaking field, best energy resolution, and optimum signal level). To study the impact of the THz streaking field on the measured XUV chirp, the pulse energy of the laser producing the

THz field was reduced to 50% for the second data point **(2)**. This reduced the streaking speed by only about 6%, as the THz production is operated in the saturation regime. For the third data point **(3)**, the pulse energy of the laser was further reduced to 30%. As a result, the streaking speed was reduced by about 30%. Throughout these measurements, the eTOF resolution (i.e., the retardation voltage) was kept constant. For these points, there is a certain variation of the chirp visible that does not seem to depend systematically on changes in the streaking field. The laser generating the THz field shows only 1% rms pulse energy fluctuations, making the resulting fluctuations in the THz field strength negligible compared with other sources of fluctuation. Therefore, these fluctuations may be attributed to drifts and fluctuations during the measurements (about 20 min per setting).

The data points **(4–8)** show measurements with negative chirp. Point **(4)** denotes again the optimum streaking settings. This setting also shows the best agreement between the values measured on both slopes of the THz streaking and the values determined by the PolariX TDS analysis. As the next step, in point **(5)**, the retardation voltage was reduced (increasing E_{kin} from 36 eV to 44 eV), leading to a worse energy resolution of the eTOF. Here, we see indeed less agreement between the two techniques. Reducing the eTOF resolution even further in point **(6)**, the retardation voltage was reduced even more (increasing E_{kin} from 44 eV to 52 eV); therefore, the broadening of the streaking could not be determined accurately, leading to discrepancies between THz streaking and PolariX. For the seventh point **(7)**, the XUV intensity was reduced to one-fourth, decreasing the number of photoelectrons created by the same amount. Thus, the signal-to-noise ratio decreased and statistical fluctuations increased (see, e.g., [10]). Conversely, for the last point **(8)**, the FEL intensity was increased four times higher, showing already signs of space charge broadening by too many photoelectrons created in the small FEL focal volume (see e.g., [10]).

Looking in more detail at Figure 3b, one can see that the fluctuations of the measured chirp differ significantly for different FEL settings. For the negative chirp setting, the SASE level was significantly lower and the electron bunch distribution was much more fluctuating, as shown in Figure 2b, leading to a broader distribution of possible chirp values determined by the TDS analysis. We also see much larger fluctuations in the chirp determined by the THz streaking and, thus, we attribute this mainly to a more unstable electron bunch, as in the positive chirp case. Still, there is a second reason why the chirp values measured by THz streaking show a larger variation. The pulse duration measured at this setting was shorter than the positive chirp case, leading to less broadening in the streaking process and thus the difference between eTOF1 and eTOF2 broadening was less, making it harder to determine the chirp accurately. The measurement at the second slope showed an even broader distribution compared with those with the first slope. This could be attributed to the even lower streaking speed (and thus broadening) of the second compared with the first slope.

For the negative chirp setting, one can see in Figure 3b that the first slope of the streaking field showed a much larger sensitivity to the changes in the streaking setup, while the data from the second slope show a broader distribution but are less sensitive to changes in the setup settings. Up until now, we do not have a solid explanation why the chirp determined for worse streaking conditions on the first slope predicts systematically higher chirps than were present.

Comparing the measurements and data analysis of both techniques, we can explore their specific strengths and drawbacks. An essential difference is that THz streaking measures the actual XUV pulse directly, while PolariX needs a prior assumption about where the lasing occurs within the electron bunch, which is particularly difficult for low-energy pulses where the lasing part within the bunch is uncertain or in cases where different parts of the electron bunch contribute to the lasing. Here, a detailed analysis of the PolariX analysis is needed while THz streaking delivers electron spectra reliably for XUV pulse energies of only ∼1 µJ [10,24]. In addition, Figure 3b shows that even with significantly detuned measurement parameters, the THz streaking technique is still able to reliably

determine both the sign and an approximate value of the chirp. Additionally, THz streaking has the advantage of being able to measure pulse duration parasitically [24], while PolariX requires separate lasing-off measurements, disrupting regular beam operations from time to time.

One limitation of THz streaking is that it can only determine the linear part of the chirp of XUV pulses reliably with the used approach (Equation (2)). Higher orders would alter not only the pulse widths, but also the pulse shape, but within current signal to noise limits an explicit quantitative calculation of higher order contributions is not possible. Still, in principle, complex electron bunch distributions with nonlinear chirp contributions can be tuned at FLASH. For instance, as illustrated in Figure 2b, if the lasing part of the bunch would be larger, strong second and third-order contributions would be present, leading to negative as well as positive chirped parts in one electron bunch. In such a case, THz streaking would lead to incorrect results. Thus, ideally, the combination of both techniques is preferable to ensure a reliable analysis.

Generally, THz streaking based on $LiNbO_3$ as the THz source has a limited range for measuring pulse durations [10]. The typical range in which the pulse duration can be determined with standard analysis is about 30-300 fs (FWHM) for unchirped pulses. For chirped pulses, accurately determining the difference in streaking width requires an even smaller range. Also, the ability to measure XUV pulses below about 30 fs with PolariX is difficult. To overcome these limitations, the future planning for FLASH2 is to rely on the determination of the XUV chirp for pulses longer $\sim$30 fs using PolariX, while for shorter pulses, a new type streaking setup will be implemented based on angular streaking [33,34]. This technique can not only determine the pulse duration in the range of $\sim$30 fs down to the sub fs range, but in addition offers the option to even measure higher-order chirps. By developing and integrating angular streaking techniques into existing FEL facilities, researchers can significantly enhance the precision and control of XUV pulses, leading to more accurate and comprehensive studies of ultrafast phenomena.

4. Conclusions

The frequency chirp of SASE-based free-electron laser XUV pulses at FLASH2 was measured using two entirely different approaches. THz streaking determines the linear chirp of the XUV pulses directly, while the PolariX TDS monitors the phase space of the electrons in the accelerator that produced the XUV radiation. Using simple scaling laws, the XUV chirp can be derived this way as well. Our results show a good agreement between the two methods across a large range of chirp values, including negative as well as positive chirps. In addition, THz streaking seems rather robust against significantly detuned experimental parameters.

Analysis of several years of THz streaking data revealed that XUV pulses often exhibit a remaining chirp, either negative or positive. This highlights the importance of chirp monitoring, especially for experiments sensitive to chirp. Future work will focus on extending these techniques to characterize even shorter pulses and higher-order chirp.

Author Contributions: Measurements, M.M.B., G.G., S.D., E.A.S., I.J.B.M., R.I. and N.M.; writing—original draft preparation, M.M.B. and S.D.; writing—review and editing, M.M.B., S.D., G.G. and E.A.S. All authors have read and agreed to the published version of the manuscript.

Funding: This research was funded by Deutsche Forschungsgemeinschaft (DFG, German Research Foundation) grant number 491245950.

Institutional Review Board Statement: Not applicable.

Informed Consent Statement: Not applicable.

Data Availability Statement: The data presented in this study are available on request from the corresponding authors.

Acknowledgments: We acknowledge DESY (Hamburg, Germany), a member of the Helmholtz Association HGF, for providing the experimental facilities and the financial support necessary to

carry out this research. We also want to acknowledge the work of the scientific and technical team at FLASH, in particular Mathias Vogt and Juliane Rönsch-Schulenburg for helpful discussions and for fulfilling our special wishes during our beamtimes. We also like to thank Ulrike Frühling for useful discussions and suggestions for improving this article.

Conflicts of Interest: The authors declare no conflicts of interest.

References

1. Ackermann, W.; Asova, G.; Ayvazyan, V.; Azima, A.; Baboi, N.; Bähr, J.; Balandin, V.; Beutner, B.; Brandt, A.; Bolzmann, A.; et al. Operation of a free-electron laser from the extreme ultraviolet to the water window. *Nat. Photonics* **2007**, *1*, 336–342. https://doi.org/10.1038/nphoton.2007.76.
2. Emma, P.; Akre, R.; Arthur, J.; Bionta, R.; Bostedt, C.; Bozek, J.; Brachmann, A.; Bucksbaum, P.; Coffee, R.; Decker, F.J.; et al. First lasing and operation of an ångstrom-wavelength free-electron laser. *Nat. Photonics* **2010**, *4*, 641–647. https://doi.org/10.1038/nphoton.2010.176.
3. Ishikawa, T.; Aoyagi, H.; Asaka, T.; Asano, Y.; Azumi, N.; Bizen, T.; Ego, H.; Fukami, K.; Fukui, T.; Furukawa, Y.; et al. A compact X-ray free-electron laser emitting in the sub-ångström region. *Nat. Photonics* **2012**, *6*, 540–544. https://doi.org/10.1038/nphoton.2012.141.
4. Decking, W.; Abeghyan, S.; Abramian, P.; Abramsky, A.; Aguirre, A.; Albrecht, C.; Alou, P.; Altarelli, M.; Altmann, P.; Amyan, K.; et al. A MHz-repetition-rate hard X-ray free-electron laser driven by a superconducting linear accelerator. *Nat. Photonics* **2020**, *14*, 391–397. https://doi.org/10.1038/s41566-020-0607-z.
5. Milne, C.J.; Schietinger, T.; Aiba, M.; Alarcon, A.; Alex, J.; Anghel, A.; Arsov, V.; Beard, C.; Beaud, P.; Bettoni, S.; et al. SwissFEL: The Swiss X-ray Free Electron Laser. *Appl. Sci.* **2017**, *7*, 720. https://doi.org/10.3390/app7070720.
6. Ko, I.S.; Kang, H.S.; Heo, H.; Kim, C.; Kim, G.; Min, C.K.; Yang, H.; Baek, S.Y.; Choi, H.J.; Mun, G.; et al. Construction and Commissioning of PAL-XFEL Facility. *Appl. Sci.* **2017**, *7*, 479. https://doi.org/10.3390/app7050479.
7. Düsterer, S.; Rehders, M.; Al-Shemmary, A.; Behrens, C.; Brenner, G.; Brovko, O.; DellAngela, M.; Drescher, M.; Faatz, B.; Feldhaus, J.; et al. Development of experimental techniques for the characterization of ultrashort photon pulses of extreme ultraviolet free-electron lasers. *Phys. Rev. ST Accel. Beams* **2014**, *17*, 120702. https://doi.org/10.1103/PhysRevSTAB.17.120702.
8. Frühling, U.; Wieland, M.; Gensch, M.; Gebert, T.; Schütte, B.; Krikunova, M.; Kalms, R.; Budzyn, F.; Grimm, O.; Rossbach, J.; et al. Single-shot terahertz-field-driven X-ray streak camera. *Nat. Photonics* **2009**, *3*, 523–528. https://doi.org/10.1038/nphoton.2009.160.
9. Grguraš, I.; Maier, A.R.; Behrens, C.; Mazza, T.; Kelly, T.J.; Radcliffe, P.; Düsterer, S.; Kazansky, A.K.; Kabachnik, N.M.; Tschentscher, Th.; et al. Ultrafast X-ray pulse characterization at free-electron lasers. *Nat. Photonics* **2012**, *6*, 852–857. https://doi.org/10.1038/nphoton.2012.276.
10. Ivanov, R.; Macias, I.J.B.; Liu, J.; Brenner, G.; Roensch-Schulenburg, J.; Kurdi, G.; Frühling, U.; Wenig, K.; Walther, S.; Dimitriou, A.; et al. Single-shot temporal characterization of XUV pulses with duration from ∼10 fs to ∼350 fs at FLASH. *J. Phys. B: At. Mol. Opt. Phys.* **2020**, *53*, 184004. https://doi.org/10.1088/1361-6455/ab9c38.
11. Frühling, U. Light-field streaking for FELs. *J. Phys. B At. Mol. Opt. Phys.* **2011**, *44*, 243001. https://doi.org/10.1088/0953-4075/44/24/243001.
12. Azima, A.; Bödewadt, J.; Becker, O.; Düsterer, S.; Ekanayake, N.; Ivanov, R.; Kazemi, M.M.; Lazzarino, L.L.; Lechner, C.; Maltezopoulos, T.; et al. Direct measurement of the pulse duration and frequency chirp of seeded XUV free electron laser pulses. *New J. Phys.* **2018**, *20*, 013010. https://doi.org/10.1088/1367-2630/aa9b4c.
13. Craievich, P.; Bopp, M.; Braun, H.H.; Citterio, A.; Fortunati, R.; Ganter, R.; Kleeb, T.; Marcellini, F.; Pedrozzi, M.; Prat, E.; et al. Novel *X*-band transverse deflection structure with variable polarization. *Phys. Rev. Accel. Beams* **2020**, *23*, 112001. https://doi.org/10.1103/PhysRevAccelBeams.23.112001.
14. Marchetti, B.; Grudiev, A.; Craievich, P.; Assmann, R.; Braun, H.H.; Catalan Lasheras, N.; Christie, F.; D'Arcy, R.; Fortunati, R.; Ganter, R.; et al. Experimental demonstration of novel beam characterization using a polarizable X-band transverse deflection structure. *Sci. Rep.* **2021**, *11*, 3560. https://doi.org/10.1038/s41598-021-82687-2.
15. Behrens, C.; Decker, F.J.; Ding, Y.; Dolgashev, V.A.; Frisch, J.; Huang, Z.; Krejcik, P.; Loos, H.; Lutman, A.; Maxwell, T.J.; et al. Few-femtosecond time-resolved measurements of X-ray free-electron lasers. *Nat. Commun.* **2014**, *5*, 1–7. https://doi.org/10.1038/ncomms4762.
16. Zewail, A.H. Femtochemistry. Past, present, and future. *Pure Appl. Chem.* **2000**, *72*, 2219–2231. https://doi.org/10.1351/pac200072122219.
17. Brixner, T.; Gerber, G. Quantum Control of Gas-Phase and Liquid-Phase Femtochemistry. *ChemPhysChem* **2003**, *4*, 418–438. https://doi.org/10.1002/cphc.200200581.
18. Gühr, M.; Ibrahim, H.; Schwentner, N. Controlling vibrational wave packet revivals in condensed phase: Dispersion and coherence for Br2 in solid Ar. *Phys. Chem. Chem. Phys.* **2004**, *6*, 5353–5361. https://doi.org/10.1039/B413635G.
19. Ding, T.; Rebholz, M.; Aufleger, L.; Hartmann, M.; Stooß, V.; Magunia, A.; Birk, P.; Borisova, G.D.; Wachs, D.; da Costa Castanheira, C.; et al. Measuring the frequency chirp of extreme-ultraviolet free-electron laser pulses by transient absorption spectroscopy. *Nat. Commun.* **2021**, *12*, 1–7. https://doi.org/10.1038/s41467-020-20846-1.

20. Patterson, B.D.; Abela, R.; Braun, H.H.; Flechsig, U.; Ganter, R.; Kim, Y.; Kirk, E.; Oppelt, A.; Pedrozzi, M.; Reiche, S.; et al. Coherent science at the SwissFEL X-ray laser. *New J. Phys.* **2010**, *12*, 035012. https://doi.org/10.1088/1367-2630/12/3/035012.
21. Ding, T.; Rebholz, M.; Aufleger, L.; Hartmann, M.; Stooß, V.; Magunia, A.; Birk, P.; Borisova, G.D.; da Costa Castanheira, C.; Rupprecht, P.; et al. XUV pump–XUV probe transient absorption spectroscopy at FELs. *Faraday Discuss.* **2021**, *228*, 519–536. https://doi.org/10.1039/D0FD00107D.
22. Dejoie, C.; McCusker, L.B.; Baerlocher, C.; Abela, R.; Patterson, B.D.; Kunz, M.; Tamura, N. Using a non-monochromatic microbeam for serial snapshot crystallography. *J. Appl. Crystallogr.* **2013**, *46*, 791–794. https://doi.org/10.1107/S0021889813005888.
23. Faatz, B.; Plönjes, E.; Ackermann, S.; Agababyan, A.; Asgekar, V.; Ayvazyan, V.; Baark, S.; Baboi, N.; Balandin, V.; von Bargen, N.; et al. Simultaneous operation of two soft x-ray free-electron lasers driven by one linear accelerator. *New J. Phys.* **2016**, *18*, 062002. https://doi.org/10.1088/1367-2630/18/6/062002.
24. Ivanov, R.; Bidhendi, M.M.; Macias, I.J.B.; Macias, I.J.B.; Brachmanski, M.; Kreis, S.; Bonfigt, S.; Degenhardt, M.; Czwalinna, M.K.; Pergament, M.; et al. Free-electron laser temporal diagnostic beamline FL21 at FLASH. *Opt. Express* **2023**, *31*, 19146–19158. https://doi.org/10.1364/OE.492228.
25. Ivanov, R.; Liu, J.; Brenner, G.; Brachmanski, M.; Düsterer, S. FLASH free-electron laser single-shot temporal diagnostic: terahertz-field-driven streaking. *J. Synchrotron Radiat.* **2018**, *25*, 26–31. https://doi.org/10.1107/S160057751701253X.
26. Oelze, T.; Kulyk, O.; Schütte, B.; Frühling, U.; Frühling, U.; Klimešová, E.; Jagielski, B.; Dittrich, L.; Drescher, M.; Drescher, M.; et al. THz streak camera performance for single-shot characterization of XUV pulses with complex temporal structures. *Opt. Express* **2020**, *28*, 20686–20703. https://doi.org/10.1364/OE.393547.
27. Christie, F.; Rönsch-Schulenburg, J.; Vogt, M. A PolariX TDS for the FLASH2 Beamline. In Proceedings of the 39th International Free Electron Laser Conference (FEL2019), Hamburg, Germany, 26–30 August 2019; pp. 328–331. https://doi.org/10.18429/JACoW-FEL2019-WEP006.
28. Craievich, P.; Aßmann, R.; Bopp, M.; Braun, H.H.; Lasheras, N.C.; Christie, F.; Citterio, A.; D'Arcy, R.; Dorda, U.; Foese, M.; et al. The PolariX-TDS Project: Bead-Pull Measurements and High-Power Test on the Prototype. In Proceedings of the 39th International Free Electron Laser Conference (FEL2019), Hamburg, Germany, 26–30 August 2019; pp. 396–399. https://doi.org/10.18429/JACoW-FEL2019-WEP036.
29. Krinsky, S.; Huang, Z. Frequency chirped self-amplified spontaneous-emission free-electron lasers. *Phys. Rev. Spec. Top. Accel. Beams* **2003**, *6*, 050702. https://doi.org/10.1103/PhysRevSTAB.6.050702.
30. Saldin, E.L.; Schneidmiller, E.A.; Yurkov, M.V. Self-amplified spontaneous emission FEL with energy-chirped electron beam and its application for generation of attosecond x-ray pulses. *Phys. Rev. Spec. Top. Accel. Beams* **2006**, *9*, 050702. https://doi.org/10.1103/PhysRevSTAB.9.050702.
31. Saldin, E.L.; Schneidmiller, E.A.; Yurkov, M.V. *The Physics of Free Electron Lasers*; Springer: Berlin, Germany, 2000.
32. Schneidmiller, E.; Dreimann, M.; Kuhlmann, M.; Rönsch-Schulenburg, J.; Zacharias, H. Generation of Ultrashort Pulses in XUV and X-ray FELs via an Excessive Reverse Undulator Taper. *Photonics* **2023**, *10*, 653. https://doi.org/10.3390/photonics10060653.
33. Hartmann, N.; Hartmann, G.; Heider, R.; Wagner, M.S.; Ilchen, M.; Buck, J.; Lindahl, A.O.; Benko, C.; Grünert, J.; Krzywinski, J.; et al. Attosecond time–energy structure of X-ray free-electron laser pulses. *Nat. Photonics* **2018**, *12*, 215–220. https://doi.org/10.1038/s41566-018-0107-6.
34. Heider, R.; Wagner, M.S.; Hartmann, N.; Ilchen, M.; Buck, J.; Hartmann, G.; Shirvanyan, V.; Lindahl, A.O.; Grünert, J.; Krzywinski, J.; et al. Megahertz-compatible angular streaking with few-femtosecond resolution at x-ray free-electron lasers. *Phys. Rev. A* **2019**, *100*, 053420. https://doi.org/10.1103/PhysRevA.100.053420.

A.4 Characterization of Free-Electron Laser Third Harmonic Radiation at FLASH

Research Article | Vol. 33, No. 5 / 10 Mar 2025 / Optics Express 10981
Optics EXPRESS

Characterization of free-electron laser third harmonic radiation at FLASH

M. M. Bidhendi,[1,*] I. J. Bermudez Macias,[1,2] R. Ivanov,[1,2] M. V. Yurkov,[1] and S. Düsterer[1]

[1] Deutsches Elektronen-Synchrotron DESY, Notkestr. 85, 22607 Hamburg, Germany
[2] Currently with the European XFEL GmbH, Holzkoppel 4, D-22869 Schenefeld, Germany
[*] mahdi.mohammadi-bidhendi@desy.de

Abstract: The Free-electron LASer in Hamburg - FLASH - generates intense ultrashort pulses with femtosecond duration in the range of 3.3 – 90 nm in the fundamental. In addition, higher harmonic contributions are always present in the spectral distribution, extending this range to much shorter wavelengths. This study presents a detailed exploration of the evolution of the radiation properties of the third harmonic contribution in the self-amplified spontaneous emission (SASE) amplification process. Utilizing a terahertz streaking setup, we measured and analyzed the pulse durations and energies of the fundamental and third harmonic during the amplification process under various operational configurations and compared these with results from the 3D time-dependent free electron laser (FEL) simulation code FAST.

1. Introduction

The interaction of the electron bunch with the extreme ultraviolet (XUV) and x-ray light generated in the undulator of a free electron laser (FEL) leads to the modulation of the electron bunch at the resonant wavelength. This in turn leads to the emission of a powerful, coherent radiation pulse at the fundamental [1–7] as well as small contributions at higher order harmonics ($2\hbar\omega$, $3\hbar\omega, \ldots n\hbar\omega$) mainly due to nonlinearities in the bunching [8–10]. For FELs with planar undulators, harmonics are typically present on the few per mill level [1,11–14].

By now the mechanism of the creation of the harmonic radiation content in FELs and their properties have been extensively studied, both theoretically [8,9,11–13,15] and experimentally [1,10,16–24] in quite some detail. However, a comprehensive experimental comparison of the fundamental and harmonic pulse durations, including their evolution during the amplification process has not been performed to the best of our knowledge. Using the THz streaking setup at FLASH [25] we can measure the pulse duration of the fundamental wavelength as well as the second and third harmonic contribution. In addition, simulations have been performed to get insight into the contributing effects.

Understanding the properties of harmonic radiation is not only of theoretical interest, as many experiments performed at FELs are influenced by higher harmonic radiation. It either generates undesired background or even mimics nonlinear multi-photon interactions [26–28]. On the other hand, many experiments are utilizing the harmonics as they significantly extend the short-wavelength range of the FEL. In particular, investigations in solid samples suffer easily from space-charge effects induced by intense FEL radiation and therefore typically only a fraction of the possible FEL pulse energy is used [29]. In these cases, the flux provided by the harmonics is well sufficient and is frequently used [17,30–33]. Knowing the pulse duration of the harmonic radiation is especially important, as most experiments at FELs are time-resolved studies.

#551587 https://doi.org/10.1364/OE.551587
Journal © 2025 Received 10 Dec 2024; revised 27 Jan 2025; accepted 5 Feb 2025; published 3 Mar 2025

Optics EXPRESS

2. Overview of the radiation properties of the harmonics

For the theoretical study, we consider the case of a free-electron laser with a planar undulator driven by an axisymmetric electron beam. The radiation of the electron beam in the planar undulator contains a rich harmonic spectrum. This refers to both coherent and incoherent radiation. Since odd harmonics of the radiation are resonant on-axis, their intensities are pronounced, while even harmonics are strongly suppressed for the case of axisymmetric electron beams [11,34,35]. The amplification process in a SASE FEL starts from the shot noise in the electron beam, and the radiation at the initial stage is just incoherent undulator radiation. Resonant harmonics are amplified independently in the so-called "linear" (exponential gain) regime [8,36]. This process is referred to as the linear harmonic generation mechanism (LHG).

Figure 1 presents simulations performed using the three-dimensional, time-dependent code FAST [37], illustrating the evolution of radiation power for the fundamental and the third harmonic. The simulation is based on typical FLASH parameters (the same as used in Ref. [38]) including a chirped electron beam as described below. In Fig. 1(a) we see that in the parameter space of FLASH, the fundamental has a much larger gain than the third harmonic. As the amplification of the fundamental approaches the onset of the nonlinear stage (maximum fluctuations in the radiation pulse energy), the density modulation in the electron beam at the higher harmonics becomes more pronounced. This results in a much stronger 3rd harmonic radiation than produced by the LHG mechanism. Starting from the undulator length $z \gtrsim 0.65 z_{sat}$ (where z_{sat} is the saturation length) the nonlinear harmonic generation mechanism (NHG) completely controls the generation of the radiation at higher harmonics. Radiation powers at this point are on the level of $E/E_{sat} \simeq 0.01$ for the fundamental, and $E/E_{sat} \simeq 0.001$ for the third harmonic, respectively (with E_{sat} as the pulse energy emitted at saturation). In practical units, these radiation energies are in the sub-microjoule range for the fundamental, and in the nanojoule range for the third harmonic.

The fluctuations observed in the radiation pulse energy curves reflect the inherent statistical nature of SASE FEL radiation. In the linear stage of amplification, all harmonics are amplified independently, and the statistical properties of the radiation of all frequency harmonics correspond to those of completely chaotic polarized light and are described by Gaussian statistics [39–41]. When an electron beam enters the undulator, its radiation consists of a large number of longitudinal and transverse modes. The mode selection process takes place along the undulator, and radiation energy fluctuations start to grow as $\sigma_E^2 = 1/M$, where M is the number of modes in the radiation pulse. Since the evolution of the fundamental is only slightly disturbed by the harmonics, we can state that its statistical properties are governed by Gaussian statistics up to the undulator length of $z \simeq 0.75 z_{sat}$. In this case, the probability distribution of the instantaneous radiation intensity W follows a negative exponential distribution, and any integral of the radiation intensity (such as radiation power P, or radiation pulse energy E), fluctuates in accordance with the gamma distribution [40,41]:

$$p(W) = \frac{1}{\langle W \rangle} \exp\left(-\frac{W}{\langle W \rangle}\right), \qquad p(E) = \frac{M^M}{\Gamma(M)} \left(\frac{E}{\langle E \rangle}\right)^{M-1} \frac{1}{\langle E \rangle} \exp\left(-M \frac{E}{\langle E \rangle}\right), \tag{1}$$

where $\Gamma(M)$ is the gamma function, with argument $M = 1/\sigma_E^2$, and $\sigma_E^2 = \langle (E - \langle E \rangle)^2 \rangle / \langle E \rangle^2$ is the relative dispersion of the radiation energy. For completely chaotic polarized light, the parameter M has a clear physical interpretation - it is the number of modes in the radiation pulse [40,41].

As depicted in Fig. 1(b), the behavior of the radiation energy fluctuations for the third harmonic differs from that of the fundamental. It is governed by Gaussian statistics up to $z \simeq 0.65 z_{sat}$, after which a rapid increase in fluctuations between $0.65 z_{sat}$ and $0.75 z_{sat}$ is observed. This occurs because the nonlinear harmonics of electron density modulation, driven by the amplification of the fundamental, start to dominate over those generated in the LHG mechanism.

The stage of the amplification process at the onset of the nonlinear regime is a very interesting range, since the third harmonic is produced by the NHG mechanism, while the radiation of

Optics EXPRESS

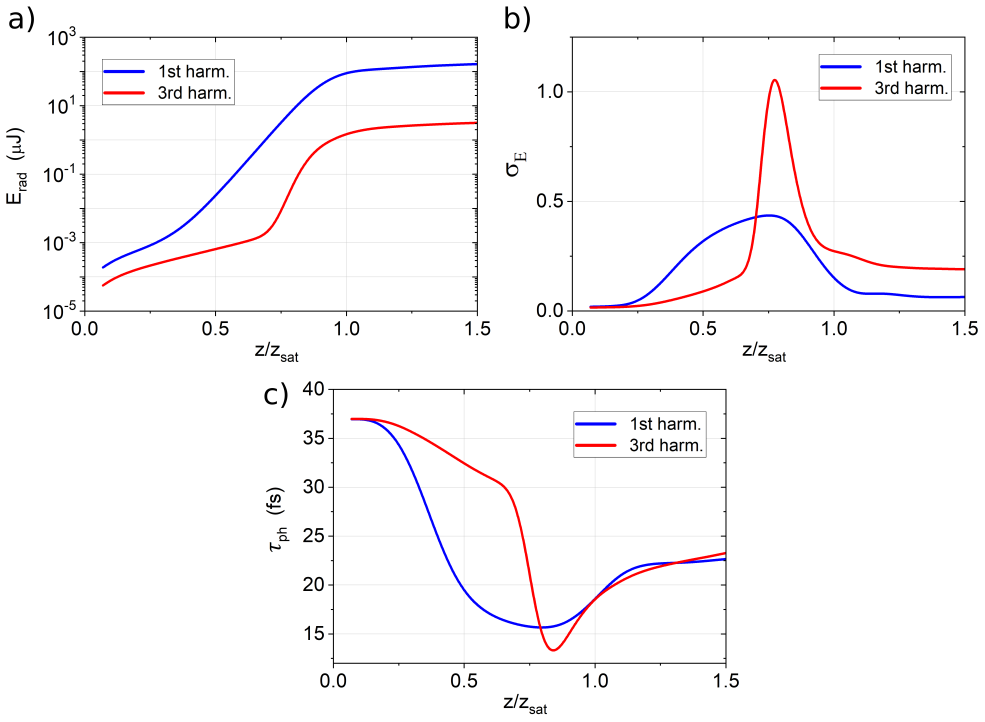

Fig. 1. Simulated gain curves for typical FLASH parameters (details provided in the text). a) Average radiation energy. b) Fluctuations of the radiation pulse energy. c) Evolution of the radiation pulse duration along the undulator. Blue and red colors correspond to the fundamental and the third harmonic, respectively. Results are obtained with the FEL simulation code FAST for an electron bunch with a 5 MeV peak-to-peak energy chirp.

the fundamental is described by Gaussian statistics. It has been noted in Ref. [12] that the statistical properties of harmonic radiation from a SASE FEL change significantly with respect to the fundamental (e.g., with respect to Gaussian statistics). In fact, the radiation intensity of a higher harmonic generated in the NHG process results from the nonlinear transformation of the fundamental intensity, expressed as $z = W^n$. Thus, the negative exponential distribution (Eq. (1)) transforms to [12,42]:

$$p(z) = \frac{z}{n\langle W\rangle} z^{(1-n)/n} \exp(-z^{1/n}/\langle W\rangle)\,. \tag{2}$$

In the nonlinear regime near the saturation point, the probability distributions for both, the fundamental and the 3rd harmonic, change significantly from those in the linear regime. For instance, at saturation, the 3rd harmonic radiation exhibits a much noisier behavior (a nearly negative exponential) for instantaneous intensities, while the fluctuations of the fundamental begin to stabilize [12].

Figure 1(c) shows the evolution of the radiation pulse duration along the undulator for both the fundamental and the third harmonic. In the initial stage of amplification, the radiation is incoherent, thus the radiation pulse profile mimics the electron beam axial profile for all harmonics. As the FEL amplification progresses, the radiation pulse duration begins to shorten since the core of the electron bunch exhibits a higher modulation and produces more radiation power. The minimum pulse duration of the fundamental is achieved at the end of the high gain exponential regime at $z \simeq 0.75 z_{sat}$. After this point, the gain in the central part of the electron

Optics EXPRESS

bunch is saturated while the tail of the bunch (where the amplification process is still in the exponential gain regime) starts to contribute more, leading to the increase of the pulse length by about 40% at the saturation point.

The evolution of the third harmonic pulse duration exhibits a different behavior. When the generation of the third harmonic is driven by the LHG mechanism (for $z \lesssim 0.65 z_{sat}$), the radiation pulse duration is reduced, but at a much slower rate than that of the fundamental. The reason for this is the significantly smaller FEL gain. When the NHG mechanism starts to dominate the harmonic generation, the pulse durations of the fundamental and third harmonic become quite comparable.

Practical estimates of SASE FEL parameters are well described in the framework of the one-dimensional model. We start with the fundamental. The amplification process in SASE FELs starts from shot noise in the electron beam. Radiation power and electron beam modulation grow exponentially until the amplification process reaches the saturation regime. The coherence time grows as well in the exponential gain regime. The saturation point corresponds to the maximum brilliance of the radiation [43]. The saturation length can be described in terms of the FEL parameter ρ and number of cooperating electrons N_c [41,44,45]:

$$z_{sat} \simeq \frac{\lambda_W}{4\pi\rho}\left(3 + \frac{\ln N_c}{\sqrt{3}}\right) \quad , \tag{3}$$

where $N_c = I/(e\rho\omega)$, ω is the radiation frequency, I is the beam current, $-e$ is the charge of electron, and λ_W is undulator period. The coherence time at saturation is given by

$$(\tau_c)_{max} \simeq \frac{1}{\rho\omega}\sqrt{\frac{\pi \ln N_c}{18}} \, . \tag{4}$$

A practical estimate for the parameter ρ can be made based on the observation that in the parameter range of SASE FELs operating in the XUV and x-ray wavelength range, the number of field gain lengths to reach saturation is about 10 [43]. Thus, the parameter ρ and the coherence time τ_c relate to the saturation length as:

$$\rho \simeq \lambda_W / z_{sat}, \quad \tau_c \simeq \lambda z_{sat}/(2\sqrt{\pi} c \lambda_W). \tag{5}$$

We consider an electron beam with a longitudinal Gaussian profile with an rms duration τ_{el}. The radiation pulse duration is mainly determined by the length of the lasing fraction of the electron bunch with additional corrections related to the slippage effect. The minimum pulse duration (τ_{ph}^{min} in FWHM) is reached at the end of the high-gain linear regime [46]:

$$\tau_{ph}^{min} \simeq 0.4\tau_{el} \simeq 0.7 \times M \times \tau_c \, . \tag{6}$$

The figure of merit for describing the radiation properties of the higher harmonics is the coupling factor K_h:

$$K_h = K(-1)^{(h-1)/2}[J_{(h-1)/2}(Q) - J_{(h+1)/2}(Q)] \, , \tag{7}$$

where $Q = K^2/[2(1+K^2)]$, K is the undulator parameter, and J is the Bessel function. In the saturation point, the radiation powers for the 3rd and 5th harmonics are related to the power of the fundamental as [12]:

$$\frac{\langle W_3 \rangle}{\langle W_1 \rangle}|_{\text{sat}} = 0.094 \times \frac{K_3^2}{K_1^2} \, , \qquad \frac{\langle W_5 \rangle}{\langle W_1 \rangle}|_{\text{sat}} = 0.03 \times \frac{K_5^2}{K_1^2} \, . \tag{8}$$

with relevant corrections for emittance and energy spread effects.

Optics EXPRESS

At the saturation point, the coherence time for higher harmonics decreases approximately in inverse proportion to the harmonic number n, while the relative spectral bandwidth remains nearly the same for all harmonics.

This model describes the SASE process in FLASH rather well. Experimental results of extended studies of harmonic generation at FLASH have been presented e.g. in Ref. [1]. In these studies, the fundamental wavelength was 13.7 nm. The contribution of the odd harmonics was in agreement with theoretical expectations, of approximately 0.6% and 0.03% for the 3rd (4.6 nm) and the 5th (2.75 nm) harmonics, respectively.

Looking at even harmonics, it is to note that the harmonic bunching factor is highest for the second harmonic, but due to the symmetry of the planar undulators, the on-axis radiation at even harmonics is strongly suppressed, since the contributions from neighboring periods are out of phase and cancel each other out due to destructive interference. Consequently, the radiation of even harmonics is significantly suppressed in a SASE FEL with a planar undulator driven by an axisymmetric electron beam [11,34,35]. The measurements of even harmonics presented in Ref. [1] have shown that they were indeed much weaker compared to the odd harmonics, since these measurements have been performed with careful tuning of the machine parameters such as the beam formation system, orbit, optics, dispersion, etc. However, sometimes measurements show non-negligible levels of the 2nd harmonic [20] as well as in the present work. This happens when not all machine parameters are tuned in a controlled way leading to an asymmetry in the radiating system. Due to a finite electron beam size, betatron motion inside the undulators as well as a not perfectly straight trajectory (and possibly other reasons) the destructive interference is limited, leading to significant second harmonic radiation. Unfortunately, the properties of the 2nd harmonic cannot be described quantitatively due to insufficient knowledge of imperfections, allowing only a qualitative discussion of potential effects [11,35,36,47].

The statistical properties of the 2nd harmonic are governed by the NHG mechanism similar to those of odd harmonics. Regarding the radiation pulse duration, within the NHG-controlled range it should evolve similarly to the fundamental. A quantitative description is only possible with precise knowledge of the asymmetries. Detailed experimental studies of the 2nd harmonic radiation are a delicate subject and require dedicated setups that also account for the specific angular distribution of the radiation.

3. Simulation of the SASE process

The analysis of the FLASH2 operation indicates that the value of the normalized rms emittance of the electron beam is in the range between 1 and 1.4 mm-mrad. Typically, at 13.5 nm, the machine reaches saturation after seven undulator modules when operating with a 1 GeV electron beam energy. This corresponds to the value of the peak electron beam current in the range from 1 to 1.5 kA. Based on multiple spectral measurements conducted at FLASH, the measured FEL bandwidth is typically around 1% FWHM [1,48–50], which is notably wider than the natural FEL bandwidth of approximately 0.4–0.5% for the given parameter space. This doubling of the natural bandwidth arises from the energy chirp along the electron bunch. Using the frequency chirp characterization method based on THz streaking, outlined in Ref. [51], we measured a chirp for the data shown in this publication that resulted in a broadening factor ranging from 1.8 to 2.3 times the natural bandwidth, which is in good agreement with the spectral measurements. Building on these findings, the the chirp in the simulation was adjusted such that the natural line width is doubled leading to a spectral width of approximately 1%.

There are several mechanisms of chirp generation. Long pulse, low current electron beam produced in the electron gun is compressed in several stages by a large factor (up to about one hundred), and the peak current is increased correspondingly [52]. To achieve such a compression, an energy chirp along the electron bunch is applied in the accelerating sections. This energy chirp leads to bunch compression when the electron bunch moves through dedicated magnetic

Optics EXPRESS

bunch compressors. The RF-induced energy chirp can be minimized such that it only slightly changes the FEL properties with respect to a monoenergetic beam. On the other hand, different kinds of wakefields and collective effects also generate an energy chirp along the electron bunch. In particular, the longitudinal space-charge field (LSC) [52] has a strong effect on the energy chirp. An important feature of the LSC wake is that the energy of the electrons in the lasing fraction of the electron bunch is increased from the tail to the head of the electron bunch. This feature results in a visible increase in FEL efficiency in the nonlinear regime, at the cost of an increase in the FEL radiation bandwidth. The radiation pulse duration is also affected by this kind of energy chirp. During the experiments discussed in this paper, the beam formation system was typically tuned such that the LSC produced a significant energy chirp, resulting in the increase of the radiation spectrum bandwidth by about a factor of 2 compared to the natural FEL bandwidth.

Thus, the simulations have been performed with the three-dimensional, time-dependent simulation code FAST [37] for an electron energy of 1 GeV including a 5 MeV peak-to-peak energy chirp, an rms energy spread of 0.2 MeV and a rms normalized emittance of 1.4 mm mrad. The lasing fraction of the electron bunch is approximated with a Gaussian distribution of about 16 fs rms pulse duration and a 1.5 kA peak current, resulting in a radiation wavelength of 13.5 nm. The same simulation parameters have already been used in Ref. [38], where a good agreement between simulation and experiment has been shown over a rather large experimental parameter range.

4. Experiment

4.1. Setup description

To obtain information on the XUV pulse duration and pulse energy for both the fundamental and its third harmonic (and to some extent the second harmonic), we used THz streaking [53,54]. The THz streaking technique employs a noble gas target, which is photoionized by the FEL pulses. The resulting photoelectrons carry the temporal and spectral characteristics of the ionizing XUV radiation. These photoelectrons propagate within the time-varying electric field of a co-propagating THz radiation and the final photoelectron kinetic energy distribution is measured by an electron time-of-flight (eTOF) spectrometer. Depending on the time of ionization with respect to the THz field, the photoelectrons change their momentum component in the polarization plane of the THz field. If the electron wave packet is short compared to the period length of the THz field, the temporal structure of the electron wave packet will be mapped onto the kinetic energy distribution of the emitted electrons and thus can be used to determine the pulse duration (details are described e.g. in Ref. [55,56]). Since the number of detected photoelectrons was proportional to the XUV photons interacting with the gas target, we could use the photoelectron spectra as the pulse energy monitor as well, similar to the approach outlined in Refs. [57,58].

The measurements were performed at the dedicated photon diagnostic beamline FL21, which is equipped with a permanently installed THz streaking setup [25]. The setup consists of an interaction chamber in which the XUV and the THz beams are focused co-linearly to the interaction point that is monitored by two eTOFs opposing each other perpendicular to the propagation direction of the XUV pulses. A dedicated laser system delivers about 1 ps long pulses at 1030 nm with a pulse energy of 3.5 mJ at a repetition rate of 10 Hz. These laser pulses are used to generate the THz radiation based on optical rectification using a nonlinear crystal ($LiNbO_3$) (for details see e.g. [56,59]).

To accurately determine the streaking effect for each XUV pulse while avoiding space-charge-induced spectral broadening, the single-shot streaked photoelectron signal must be sufficiently intense, but not excessive to avoid a too large amount of ions created in the FEL focal volume. Because of the large collection efficiency of the eTOF (Kaessdorf ETF11) and the high cross section of noble gases in the XUV regime, only few 100 nJ of pulse energy are needed to

Optics EXPRESS

accurately measure the kinetic energy distribution of the photoelectrons [56]. The low pulse energy requirement allows the measurement of even the weak harmonic content of the FEL radiation. Since the harmonics typically only contain a fraction of a percent of the fundamental radiation, the latter one has to be suppressed substantially to be able to monitor the harmonic signal without tremendous space-charge effects of the fundamental. Therefore, thin metal filters (such as 200 nm zirconium in the present case) must be used to reduce the intensity of the fundamental wavelength significantly (see Fig. 2). This ensures an accurate measurement of the higher harmonics alongside the fundamental. Due to the strongly attenuated fundamental and a rather large XUV focal spot of ~ 100 µm, we can exclude the possibility of multiphoton processes contributing to the observed signals.

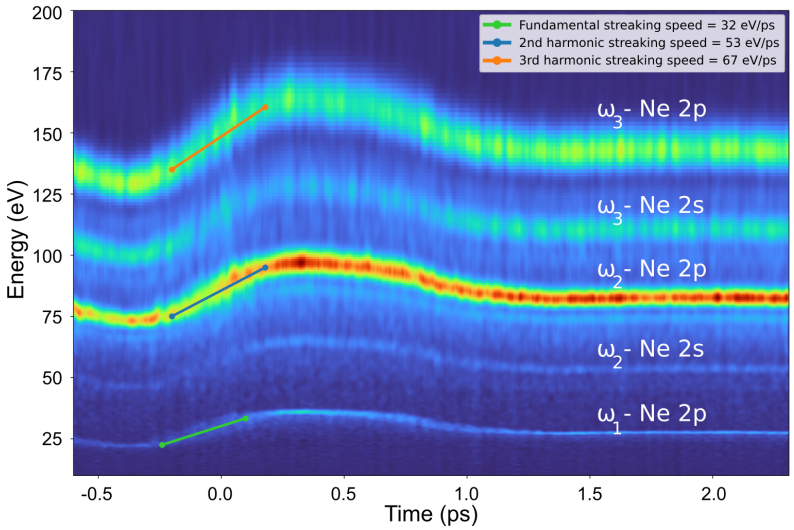

Fig. 2. Kinetic energy of neon 2p and 2s photoelectrons induced by the fundamental, second and third harmonic radiation of FLASH. The photoelectrons are created in the presence of the THz streaking field, plotted as a function of the time delay between the FEL and THz pulses. The fundamental FEL wavelength was set to 24 nm (52 eV), leading to a second harmonic of 12 nm (104 eV) and a third harmonic of 8 nm (155 eV). The fundamental radiation is strongly suppressed by a 200 nm thick Zr filter. The 'streaking speed' is derived from the slope of the linear segment in each streaking trace.

4.2. Pulse duration measurements

In Fig. 2, the kinetic energy spectra of photoelectrons created by the fundamental, second and third harmonic are plotted as a function of the temporal delay between the XUV and THz pulses. This delay scan, often called the 'streaking trace,' is directly proportional to the vector potential of the THz field. The streaking trace provides the maximum energy shift of photoelectrons for a given THz field and electron kinetic energy. By fitting the linear segment of the streaking trace (shown as solid lines in Fig. 2), we can determine the 'streaking speed', a parameter that connects the energy shift with the emission time [56,60]. Note, that the streaking speed increases (for the same THz field) with the kinetic energy of the electrons as $\sqrt{E_{kin}}$ [55]. The pulse durations were analyzed following the method described in Ref. [51], with the chirp taken into account.

FLASH can be operated in a large range of parameters regarding wavelength, pulse energy, pulse duration, etc. Thus, the pulse durations of the fundamental and the third harmonic were not only measured for a specific setting but utilizing the benefit of a permanently installed diagnostics

Optics EXPRESS

endstation [25] several different FEL configurations were used. As illustrated in Fig. 3 the fundamental (blue points) and the third harmonic (red points) pulse durations were measured as a function of the amplification along the undulator.

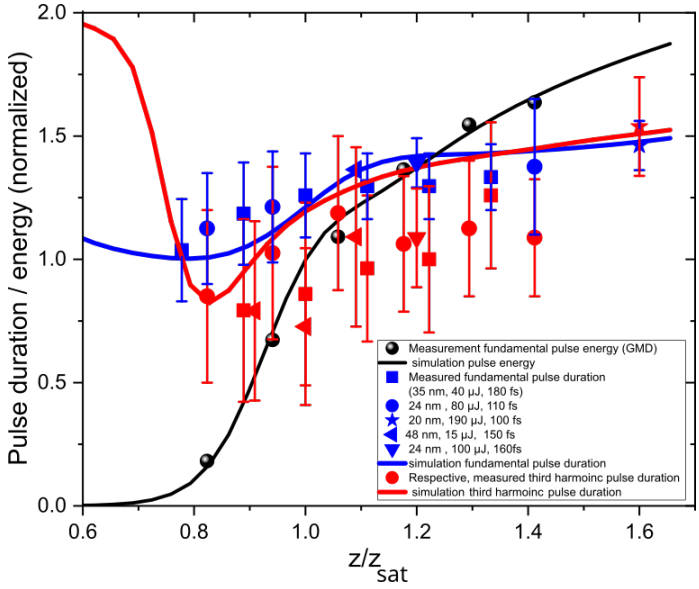

Fig. 3. Evolution of the measured pulse duration for the fundamental and the third harmonic for various FEL settings compared to the simulation. The experimental data was acquired over a period of several years for different FEL settings (see legend). For each data point ~ 3000 pulses of τ_{ph}^{1st} and τ_{ph}^{3rd} have been measured with THz streaking. To compare the individual measurements the fundamental pulse durations of each setting have been scaled to the simulation and the same scaling factor was applied to the third harmonic durations. The 'error bars' do not show the experimental uncertainty, but rather the rms width of the observed pulse duration distribution caused by SASE-based fluctuations, 'technical' fluctuations as well as measurement errors to demonstrate how much the FEL pulse duration changes for a particular setting. The simulated values (lines) are the 3D FAST simulations for a chirped electron pulse, as shown in Fig. 1.

Analog to the scheme outlined in Ref. [38] the undulators were opened one by one and the experimental conditions (XUV pulse energy and suppression of the fundamental) were optimized for each setting. In total, we measured the complete gain curve or at least parts of it in several different measurement campaigns distributed over few years. Thus, we cover a large range of FEL settings with fundamental wavelengths from 20 to 48 nm, for pulse durations in the range of 100 fs to 180 fs and saturation energies of 15 μJ to almost 200 μJ.

The experimentally determined pulse durations of the third harmonic (red points) and the fundamental (blue points) for a large parameter range are presented in Fig. 3 together with the simulation result as solid lines. To compare the different settings, the pulse durations of the fundamental and the pulse energies were scaled to the FAST simulation. The scaling process followed the method described in Ref. [38], as the simulation result for the fundamental provides a reasonably accurate description of the evolution of the pulse duration along the undulators, despite differences between the experimental and simulated parameters.

The number of undulators was scaled to the undulator coordinate z, ensuring that the onset of measurable SASE (>0.5 μJ) aligns with the z range in which the energy gain becomes visible in the simulated energy gain curve ($z/z_{sat} \sim 0.7$). This establishes the scaling for the undulator axis

Optics EXPRESS

and defines the saturation length z_{sat}. Subsequently, the pulse energy was scaled such that at $z = z_{sat}$, the pulse energy was defined as the saturation pulse energy E_{sat}, and all energies were normalized to this value. Since we typically have fewer measurements for the pulse duration than we have for the pulse energy, we cannot normalize the pulse durations as systematically as the pulse energy. Thus, we chose the approach to scale the pulse durations of the fundamental for each experimental setting to minimize the deviation to the simulation and use this factor to subsequently scale the third harmonic duration.

Due to the lack of theoretical predictions for comparison, the second harmonic pulse duration was not systematically studied. However, for a few cases second harmonic data was taken, showing that the second harmonic pulse duration had about the same pulse duration as the third harmonic, thus slightly shorter than the fundamental.

4.3. Pulse energy in the harmonic

Typical XUV pulse energies for the fundamental are in the range of tens to hundreds of μJ for FLASH while the second and third harmonic radiation is expected to be on the order of 0.2-2%, thus in the nJ or low μJ range [12]. See also Ref. [21] for a comprehensive analysis of the second and third harmonic at the European XFEL.

The determination of the actual pulse energy ratios of the harmonics and the fundamental radiation at the exit of the undulator is indeed not as easy as it may look at first glance at Fig. 2. Here one can rather easily determine the different signal amplitudes for the fundamental, second and third harmonic. However one has to consider several factors that influence this ratio on the way between the undulator exit to the detector of the eTOF.

First of all the fundamental radiation is attenuated by the so-called gas attenuator, in order to reduce the amount of FEL photons that reach the THz streaking setup. The attenuator consists of a $\sim$ 15 m long part of the XUV beamline which can be filled with up to few times 10^{-2} mbar of gas (noble gas or, as in the present case, nitrogen) that typically has significantly different cross-sections for the fundamental and the harmonics (here we consider the wavelength range of 25 nm- 35 nm). Following the Lambert-Beer law we can determine the attenuation which can be many times higher for the fundamental than for the harmonics for high gas pressures in the attenuator. The second influence to consider is the presence of 5 mirrors in the beam path (3x carbon coated + 2x gold coated) with only a small wavelength dependence in the measured range but significant influence for shorter wavelengths.

An additional source of influence is the wavelength-dependent cross-section of the target gas (Ne), which is about 2-4 times larger for the fundamental than for the harmonics [62]. In addition, the asymmetry parameter β, indicating the angular distribution of the photoelectrons, changes over the considered wavelengths range by a factor of about 2 [62]. Electrons ejected by shorter wavelength radiation are more predominately emitted along the polarization axis of the XUV and thus are more efficiently collected by the eTOF.

Finally, to get a sufficient eTOF signal for the harmonic radiation, the electrostatic lens in the eTOF has to be optimized for a good transmission for faster electrons, which leads again to a change of the fundamental to harmonic signal ratio in the range of 10. This enhancement factor can be determined by measuring the ratio with and without a lens for a strong harmonic signal (in deep saturation). Furthermore one has to consider that the measured signal by the eTOF is proportional to the number of photons present in the harmonic or the fundamental. Thus, to get the ratio in pulse energy (μJ) one has to multiply the determined ratios by 2 for the second and 3 for the third harmonic. Using all corrections leads to rather a large uncertainty which we estimate to be about $\pm$ 50%.

We do not consider the possible difference in pointing and divergence of the fundamental and the harmonics, since typically most of the radiation propagating along the beamline is collected by the focusing mirror and is focused on the interaction point.

Optics EXPRESS

4.3.1. Pulse energy measurement

The second and third harmonic ratios vary a lot each time the FEL is set up for a new operation point (different pulse duration, wavelengths, pulse energy, etc.). Looking at the large number of measurements taken over a period of several years, we find the second harmonic ratio range at ~ 0.1-0.6% and the third harmonic ratio at ~ 0.2-0.6% compared to the fundamental pulse energy. Measurements with a grating spectrometer have determined values up to 1% for FEL settings specifically optimized for the third harmonic. The determined third harmonic range is also in agreement with Eq. (8), predicting a maximum third harmonic contribution between 0.9% (for $K \sim 1$) and 1.8% (for $K \sim 2$) within the K (undulator parameter) range used in the experiments (see Ref. [8]). Here one has to take into account that the typical energy spread suppresses the third harmonic up to a factor of 3 in the practical case [12] decreasing the maximum values to the range of the experimentally determined ratios. In the future, a third harmonic afterburner undulator will further enhance the radiation output at the third harmonic at FLASH2 [63].

The development of the FEL pulse energy along the undulators is illustrated in Fig. 4(a). The simulation (solid lines) suggests that, at the end of the linear amplification regime of the fundamental, NHG mechanism governs the generation of the third harmonic such that the power of the third harmonic increases more rapidly than the power of the fundamental. Therefore, according to the simulation, to achieve a high-intensity third harmonic, the FEL likely needs to be tuned for saturation or even better deep saturation regime. Experimental data suggest a similar trend to that indicated by the simulation. However, the absolute values of the harmonic energies are lower than predicted by the simulation. A possible reason is that the measurement was taken for a standard FEL setup that was not tailored for harmonic emission. The second harmonic radiation is in addition to the third harmonic signal also recorded in the eTOF traces. Thus, we can present the measured values, which are typically rather similar to the third harmonic, but due to limited knowledge about non-symmetry in the radiating system that leads to the generation of the second harmonic, no simulation was performed.

4.3.2. Pulse energy fluctuations

Since the pulse energy is measured for each FEL pulse, we extended the analysis from the average pulse energies shown in Fig. 4(a), to the pulse-to-pulse energy fluctuations as shown in Fig. 4(b). The fluctuation (rms of the pulse energy normalized to the average pulse energy) of the fundamental and third harmonic pulse energy are plotted along the undulators and compared with the simulation. The simulation predicts that the fluctuation increases in the linear regime to a maximum at about $z/z_{sat} \sim 0.8$, where the fundamental and third harmonic reach their maximum fluctuation and subsequently the fluctuations are strongly suppressed in saturation [12,40]. While the third harmonic shows lower fluctuations than the fundamental in the very early part of the amplification it has a much stronger increase and exceeds the fluctuations of the fundamental by factor ~ 2.5 at $z/z_{sat} \sim 0.8$. The fluctuations of the third harmonic, however, stay about 2.5 higher than the fundamental fluctuations in deep saturation, since in this regime the third harmonic is governed by the NHG while the fundamental radiation follows Gaussian statistical behavior. Thus, to obtain a third harmonic pulse with reduced fluctuations, the FEL should operate in the saturation and deep saturation regime. The measured fluctuations exceed the theoretically predicted values, mainly due to measurement uncertainties and additional technical fluctuations during the acceleration process, as discussed in detail in Ref. [61].

4.4. Single-pulse correlations

4.4.1. Pulse energy correlation

Recording the pulse energies for each FEL pulse at the fundamental and the third harmonic enables the investigation of any correlation between them. The pulse energy of the fundamental radiation

Optics EXPRESS

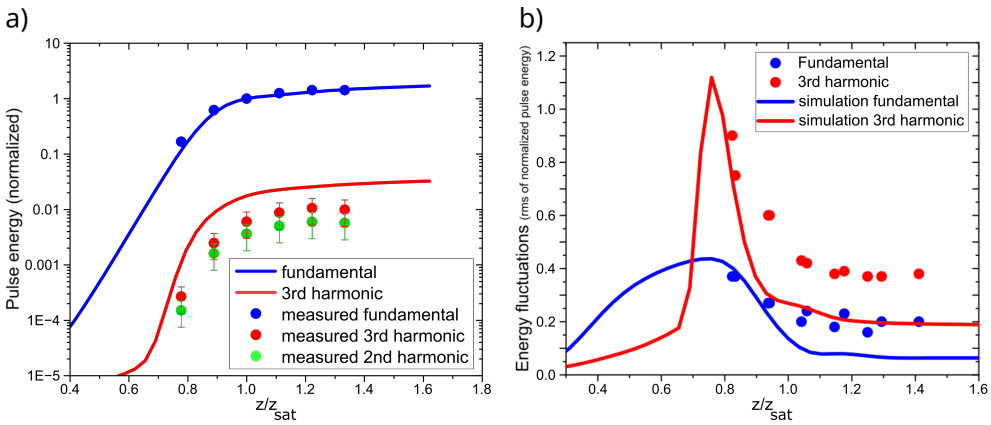

Fig. 4. a) Evolution of the pulse energy for the fundamental, second and third harmonic, displayed on a logarithmic scale, as a function of the undulator length on a linear scale (symbols are experimental data, lines are from the FAST simulation). All data points were normalized on the fundamental pulse energy at the onset of saturation ($z/z_{sat} = 1$). The estimated error for the harmonic experimental data is ±50% - see text. b) Fluctuations of the pulse energy for the fundamental and the third harmonic as a function of undulator length, comparing experimental data with simulation results. The experimental data shows larger fluctuations than the theoretically expected values, which can be attributed to measurement uncertainty and additional technical fluctuations in the accelerator, as discussed in Ref. [61]. The third harmonic shows about a factor of 2.5 larger energy fluctuation than the fundamental at $z/z_{sat} = 0.8$ and beyond. This difference arises in the saturation regime, as the third harmonic is produced by the NHG mechanism, while the fundamental is described by Gaussian statistics.

was measured using a gas monitor detector (GMD) [57,64] upstream of the THz streaking (which has a measurement precision of ~ ±5%). The energy of the third harmonic is derived from the signal intensity measured by the eTOFs. The single-shot energies of the fundamental and third harmonic along the undulators are shown in Fig. 5(a) to (d). The experimental data shows no correlation between the pulse energy of the third harmonic and fundamental. Still, one can see the decrease of the fluctuations as the amplification process advances (as shown in Fig. 4(b)). The simulation predicts a linear correlation between the pulse energies of the fundamental and third harmonic in the linear regime. However, this linear correlation was not observed experimentally, probably due to the larger measurement uncertainties in this regime.

4.4.2. Pulse duration correlation

Additionally, the pulse duration of the third harmonic was measured pulse resolved with THz streaking and, thus, can be compared with the pulse energy of the third harmonic. The result together with the simulation is shown in Fig. 5(e) to (h) at different stages of the amplification process. The simulation suggests that fluctuations in pulse energy are approximately twice as large as those in pulse duration. The experimental data confirm this but with broader fluctuations as seen in Fig. 4(b). The simulation as well as the experimental results indicate no clear correlation between the pulse duration and pulse energy of the third harmonic in or close to saturation. On the other hand, the simulation predicts an interesting relation for the early amplification stage ($z/z_{sat} = 0.76$) for which we unfortunately do not have sufficient experimental data due to the low signal level at $z/z_{sat} = 0.76$.

Optics EXPRESS

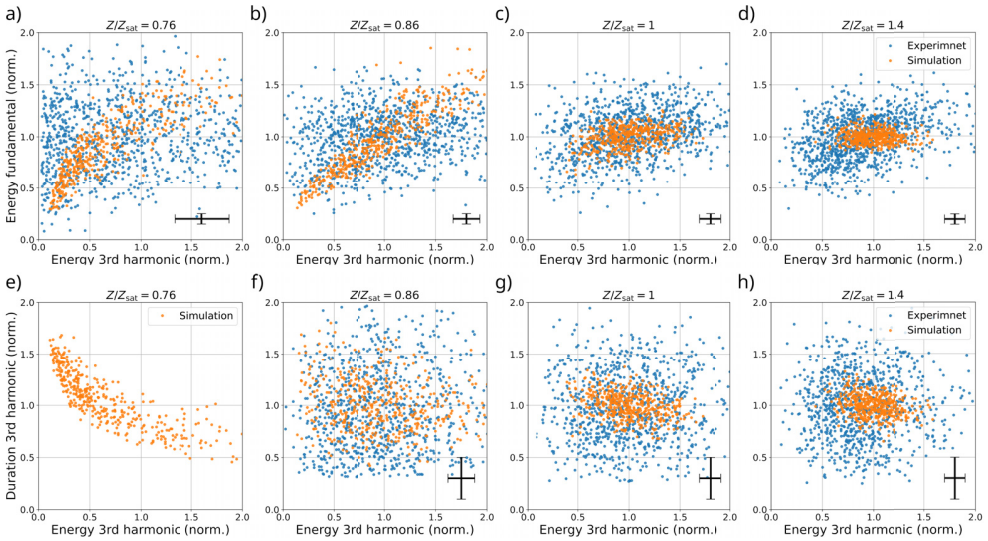

Fig. 5. The upper row shows the experimental and simulated data the for single-shot pulse energy of the fundamental and third harmonic, at different stages of amplification. All shown data is normalized to the respective mean value. The experimental data does not show a correlation. The lower row shows experimental and simulated data for the pulse duration and pulse energy of the third harmonic. In e), the experimental result is not shown since the third harmonic signal was too low for a reliable pulse duration measurement.

5. Discussion

In Ref. [38] we compared the evolution of the fundamental pulse duration and energy along the undulator with predictions from a 3D FEL simulation (FAST code), using standard FLASH settings including a chirped electron beam. There was a remarkable agreement of the measurements with the simulation despite the simulation being performed for one specific case and the measurements spanned over a rather large parameter range (wavelengths from 8 nm to 34 nm). As shown in Ref. [38] the addition of a chirp in the electron bunch simulation leads to much better agreement with the experimental data. Here we extended the approach by including the pulse duration and energy of the third harmonic content of the FEL radiation. And again we find a reasonable agreement between the simulation results and the measurements.

Figure 3 shows the photon pulse duration for the fundamental and the third harmonic radiation as a function of the undulator coordinate z. The simulation shows that the pulse duration of the fundamental is rather constant in the linear regime (z/z_{sat}<0.8) and increases towards the end of the linear regime by only $\sim$ 30% and stays almost constant in saturation (in contrast to the unchirped simulation where the pulse duration strongly increases in saturation [38]). The third harmonic pulse duration has a more interesting behavior. In the linear regime it is actually longer than the fundamental. In this regime, the generation of the third harmonic is primarily driven by the LHG mechanism (up to $z \approx 0.65 z_{sat}$). Therefore, the third harmonic pulse duration remains longer than that of the fundamental. This slower reduction in duration is attributed to the smaller FEL gain for the third harmonic compared to the fundamental. However, as the NHG mechanism begins to dominate (around $z \gtrsim 0.65 z_{sat}$), the third harmonic experiences enhanced amplification driven by nonlinear density modulation effects. After the saturation point, the simulation predicts that the pulse duration of the fundamental and the third harmonic are about identical. This is indeed surprising if one compares this with seeded FELs where the nth harmonic of the seed laser leads to an FEL pulse duration scaling (in the simplest approach) as $1/\sqrt{n}$ [65] and the same

Optics EXPRESS

scaling applies for the harmonic generation of optical pulses in a nonlinear crystal (again in a simple approach) [66].

The experimental data shows a large variation of the third harmonic pulse durations which can be attributed to the widely different experimental settings for each experimental campaign. Still, it shows a similar trend as the simulation, namely a slight pulse duration elongation from linear range to deep saturation. However, looking at the actual third harmonic pulse durations, they are on average $\sim 20\%$ shorter as compared to the fundamental, and thus slightly shorter than anticipated by the simulation. This may be due to a not fully optimized electron bunch phase space for the standard operation.

Looking at the pulse energy, the simulation result shown in Fig. 4(a) predicts that in the linear regime, the third harmonic's energy rises significantly faster compared to the fundamental. Upon reaching the saturation regime, the increase in pulse energy for both the fundamental and the third harmonic slows down. The experimental data follows a similar trend but with lower overall energy values, which again can be caused by unoptimized FEL settings.

Utilizing the third harmonic in FEL experiments it is not only important to know the pulse energy but also its fluctuations. The energy fluctuations shown in Fig. 4(b) indicate that the fundamental and third harmonic reach their maximum fluctuation at the end of the linear regime at $z/z_{sat} = 0.8$ [12]. Both theory and experiment show that the fluctuation decreases strongly afterwards. It is to be noted that the energy fluctuations of the third harmonic are at the end of the linear regime till deep saturation about 2.5 times larger than the ones for the fundamental, thus making measurements using the third harmonic more challenging.

Summarizing the findings so far, the best operation point (not considering transverse beam properties) for decent third harmonic radiation at FLASH is in deep saturation. The pulse energy is still growing in saturation for a (negatively) chirped electron bunch while the fluctuations are constantly low and the pulse duration only increases slightly.

Since the THz streaking measures the pulse energy and pulse duration for each photon pulse, we can also look for correlations between different radiation properties. In Ref. [61] we looked at correlations between various properties of the fundamental radiation and found no significant correlations in saturation either in the simulation or in the experimental data. Looking at Fig. 5 we also find no defined correlation for the pulse energy or pulse duration of the third harmonic in saturation. However, the simulation predicts a strong correlation between the fundamental and the third harmonic pulse energy in the linear regime, which is not represented in the experimental data. Even having the large error bars, we should be able to see a certain degree of correlation in the data and it is up to now not understood why it was not observed. Looking at the exponential gain regime there is a negative correlation between the third harmonic pulse energy and pulse duration (analog to the simulations for the fundamental presented in Ref. [61]) as shown in Fig. 5(e). The pulse duration tends to be shorter for pulses with larger energy. Unfortunately, due to the low signal-to-noise ratio at $z/z_{sat} = 0.76$, we were not able to measure the pulse duration and compare with the prediction.

Generally, the absence of correlation for the saturated pulses is advantageous for data analysis. When sorting the experimental dataset according to one radiation property there is no undesired spurious correlation with another property which could lead to false correlations in the sorted experimental data.

Considering that the simulation was performed for quite different FEL parameters the agreement is rather remarkable. In several cases, the measured performance was less than in the (perfect) simulations which we attribute to not fully optimized FEL settings. This may sound like a drawback for the comparison with the theoretical predictions, but we deliberately measured with the standard settings that are present for all-day operation, to document the parameters available for experiments without dedicated optimization of certain parameters. This way we get a good

Optics EXPRESS

estimation of the variation of parameters and how well the theoretical predictions can be used for the planning of future experiments.

6. Conclusion

We analyzed the evolution of the pulse duration and pulse energy of the fundamental and third harmonic radiation of FLASH during the amplification process. Using THz streaking as a detection method, measurements were taken for a large range of FEL parameters from 20 nm to 48 nm, for pulse durations in the range of 100 fs to 180 fs and saturation energies of 15 μJ to almost 200 μJ for the fundamental radiation. The experimental results were compared to 3D simulations (FAST code) simulating a chirped electron bunch, similar as described in Ref. [38]. Due to the large parameter range, the measurements show some variation, but in general we can state that the third harmonic pulse duration is about 20% shorter as compared to the fundamental, with a pulse energy ratio to the fundamental ranging from 0.2% to 0.6%. The pulse durations of fundamental and third harmonic increase from the onset of saturation to deep saturation only slightly due to the electron chirp which is typically present at FLASH. The energy fluctuations of the third harmonic decrease from the end of the linear regime to deep saturation but stay for the whole range about 2.5 times higher than the fluctuations of the fundamental. Looking at correlations between pulse energy and pulse duration we found experimentally no significant correlations between the properties (similar to investigations in Ref. [61]). In contrast, the simulations predict correlations in the early stage of the amplification which are experimentally not easily accessible. Despite the differing FEL parameters used in the simulation and the experiments, the agreement between the measured data and the simulations is decent. Thus, the predictions of the simulation can be used for a large parameter range to guide future FEL experiments.

Funding. Deutsche Forschungsgemeinschaft (491245950).

Acknowledgments. We acknowledge DESY (Hamburg, Germany), a member of the Helmholtz Association HGF, for the provision of experimental facilities. This research was carried out at FLASH. Particularly, we want to acknowledge the work of the scientific and technical team at FLASH for helpful discussions and for fulfilling our special wishes during our beamtimes. We also like to acknowledge Ulrike Frühling for useful discussions and suggestions for improving this article. We also thank Marion Kuhlmann for providing information on spectral measurements of higher harmonics. This work was partially funded by the Helmholtz Association IVF fund under project InterLabs-0002 "HELPFEL."

Disclosures. The authors declare no conflicts of interest.

Data availability. The data presented in this study are available on request from the corresponding authors.

References

1. W. Ackermann, G. Asova, V. Ayvazyan, *et al.*, "Operation of a free-electron laser from the extreme ultraviolet to the water window," Nat. Photonics **1**(6), 336–342 (2007).
2. P. Emma, R. Akre, J. Arthur, *et al.*, "First lasing and operation of an ångstrom-wavelength free-electron laser," Nat. Photonics **4**(9), 641–647 (2010).
3. D. Pile, "First light from SACLA," Nat. Photonics **5**(8), 456–457 (2011).
4. T. Ishikawa, H. Aoyagi, T. Asaka, *et al.*, "A compact X-ray free-electron laser emitting in the sub-ångström region," Nat. Photonics **6**(8), 540–544 (2012).
5. E. Allaria, R. Appio, L. Badano, *et al.*, "Highly coherent and stable pulses from the FERMI seeded free-electron laser in the extreme ultraviolet," Nat. Photonics **6**(10), 699–704 (2012).
6. M. Altarelli, "The European X-ray free-electron laser facility in Hamburg," Nucl. Instrum. Methods Phys. Res., Sect. B **269**(24), 2845–2849 (2011).
7. B. D. Patterson, R. Abela, H.-H. Braun, *et al.*, "Coherent science at the SwissFEL x-ray laser," New J. Phys. **12**(3), 035012 (2010).
8. Z. Huang and K.-J. Kim, "Three-dimensional analysis of harmonic generation in high-gain free-electron lasers," Phys. Rev. E **62**(5), 7295–7308 (2000).
9. H. P. Freund, S. G. Biedron, and S. V. Milton, "Nonlinear harmonic generation and proposed experimental verification in SASE FELs," Nucl. Instrum. Methods Phys. Res., Sect. A **445**(1-3), 53–58 (2000).
10. S. G. Biedron, R. J. Dejus, Z. Huang, *et al.*, "Measurements of nonlinear harmonic generation at the Advanced Photon Source's SASE FEL," Nucl. Instrum. Methods Phys. Res., Sect. A **483**(1-2), 94–100 (2002).
11. G. Geloni, E. Saldin, E. Schneidmiller, *et al.*, "Exact solution for second harmonic generation in XFELs," Opt. Commun. **271**(1), 207–218 (2007).

Optics EXPRESS

12. E. L. Saldin, E. A. Schneidmiller, and M. V. Yurkov, "Properties of the third harmonic of the radiation from self-amplified spontaneous emission free electron laser," Phys. Rev. Spec. Top.–Accel. Beams **9**(3), 030702 (2006).
13. E. A. Schneidmiller and M. V. Yurkov, "Harmonic lasing in x-ray free electron lasers," Phys. Rev. Spec. Top.–Accel. Beams **15**(8), 080702 (2012).
14. E. A. Schneidmiller and M. V. Yurkov, "Coherence Properties of the Odd Harmonics of the Radiation from SASE FEL with Planar Undulator," *Proceedings of the 34th International Free Electron Laser Conference* (2012).
15. J. B. Murphy, C. Pellegrini, and R. Bonifacio, "Collective instability of a free electron laser including space charge and harmonics," Opt. Commun. **53**(3), 197–202 (1985).
16. E. Schneidmiller and M. Yurkov, *Background-free Harmonic Production in XFELs via a Reverse Undulator Taper* (JACOW, Geneva, Switzerland, 2017).
17. R. Y. Engel, P. S. Miedema, D. Turenne, *et al.*, "Parallel Broadband Femtosecond Reflection Spectroscopy at a Soft X-Ray Free-Electron Laser," Appl. Sci. **10**(19), 6947 (2020).
18. R. Kato, M. Fujimoto, T. Igo, *et al.*, "Characteristic measurements of higher harmonics generated in the SASE-FEL process," Nucl. Instrum. Methods Phys. Res., Sect. A **507**(1-2), 409–412 (2003).
19. A. Tremaine, X. J. Wang, M. Babzien, *et al.*, "Measurements of nonlinear harmonic radiation and harmonic microbunching in a visible SASE FEL," Nucl. Instrum. Methods Phys. Res., Sect. A **507**(1-2), 445–449 (2003).
20. S. DÜsterer, P. Radcliffe, G. Geloni, *et al.*, "Spectroscopic characterization of vacuum ultraviolet free electron laser pulses," Opt. Lett. **31**(11), 1750–1752 (2006).
21. T. M. Baumann, R. Boll, A. De Fanis, *et al.*, "Harmonic radiation contribution and X-ray transmission at the Small Quantum Systems instrument of European XFEL," J. Synchrotron Radiat. **30**(4), 662–670 (2023).
22. A. Tremaine, X. J. Wang, M. Babzien, *et al.*, "Experimental Characterization of Nonlinear Harmonic Radiation from a Visible Self-Amplified Spontaneous Emission Free-Electron Laser at Saturation," Phys. Rev. Lett. **88**(20), 204801 (2002).
23. G. Penco, G. Perosa, E. Allaria, *et al.*, "Nonlinear harmonics of a seeded free-electron laser as a coherent and ultrafast probe to investigate matter at the water window and beyond," Phys. Rev. A **105**(5), 053524 (2022).
24. C. Spezzani, A. Ravindran, E. Allaria, *et al.*, "Circular dichroism experiments at the *L* edge of magnetic transition metals enabled by elliptically polarized pulses from a seeded free-electron laser," Phys. Rev. B **110**(17), 174409 (2024).
25. R. Ivanov, M. M. Bidhendi, I. J. B. Macias, *et al.*, "Free-electron laser temporal diagnostic beamline FL21 at FLASH," Opt. Express **31**(12), 19146–19158 (2023).
26. M. Straub, T. Ding, M. Rebholz, *et al.*, "Differential Measurement of Electron Ejection after Two-Photon Two-Electron Excitation of Helium," Phys. Rev. Lett. **129**(18), 183204 (2022).
27. S. M. Durkan, V. Richardson, L. Varvarezos, *et al.*, "Multiphoton single and double ionization of neon in the EUV," J. Phys. B: At., Mol. Opt. Phys. **58**(1), 015601 (2025).
28. V. Richardson, J. T. Costello, D. Cubaynes, *et al.*, "Two-Photon Inner-Shell Ionization in the Extreme Ultraviolet," Phys. Rev. Lett. **105**(1), 013001 (2010).
29. D. Kutnyakhov, R. P. Xian, M. Dendzik, *et al.*, "Time- and momentum-resolved photoemission studies using time-of-flight momentum microscopy at a free-electron laser," Rev. Sci. Instrum. **91**(1), 013109 (2020).
30. A. P. Mancuso, T. Gorniak, F. Staier, *et al.*, "Coherent imaging of biological samples with femtosecond pulses at the free-electron laser FLASH," New J. Phys. **12**(3), 035003 (2010).
31. T. Gorniak, R. Heine, A. P. Mancuso, *et al.*, "X-ray holographic microscopy with zone plates applied to biological samples in the water window using 3rd harmonic radiation from the free-electron laser FLASH," Opt. Express **19**(12), 11059–11070 (2011).
32. C. Gutt, L.-M. Stadler, S. Streit-Nierobisch, *et al.*, "Resonant magnetic scattering with soft x-ray pulses from a free-electron laser operating at 1.59 nm," Phys. Rev. B **79**(21), 212406 (2009).
33. S. Hellmann, C. Sohrt, M. Beye, *et al.*, "Time-resolved x-ray photoelectron spectroscopy at FLASH," New J. Phys. **14**(1), 013062 (2012).
34. Z. Huang and K.-J. Kim, "Review of x-ray free-electron laser theory," Phys. Rev. Spec. Top.–Accel. Beams **10**(3), 034801 (2007).
35. D. Ratner, A. Brachmann, F. J. Decker, *et al.*, "Second and third harmonic measurements at the linac coherent light source," Phys. Rev. Spec. Top.–Accel. Beams **14**(6), 060701 (2011).
36. Z. Huang and K.-J. Kim, "Nonlinear harmonic generation of coherent amplification and self-amplified spontaneous emission," Nucl. Instrum. Methods Phys. Res., Sect. A **475**(1-3), 112–117 (2001).
37. E. L. Saldin, E. A. Schneidmiller, and M. V. Yurkov, "FAST: a three-dimensional time-dependent FEL simulation code," Nucl. Instrum. Methods Phys. Res., Sect. A **429**(1-3), 233–237 (1999).
38. M. M. Bidhendi, I. J. Bermudez Macias, R. Ivanov, *et al.*, "FEL Pulse Duration Evolution along Undulators at FLASH," Appl. Sci. **12**(14), 7048 (2022).
39. J. W. Goodman, *Statistical Optics*, 2nd Edition (Wiley, 2015).
40. E. L. Saldin, E. A. Schneidmiller, and M. V. Yurkov, "Statistical properties of radiation from VUV and X-ray free electron laser," Opt. Commun. **148**(4-6), 383–403 (1998).
41. E. L. Saldin, E. A. Schneidmiller, and M. V. Yurkov, *The Physics of Free Electron Lasers* (Springer, 2000).
42. E. L. Saldin, E. A. Schneidmiller, and M. V. Yurkov, "Scheme for attophysics experiments at a X-ray SASE FEL," Opt. Commun. **212**(4-6), 377–390 (2002).

Optics EXPRESS

43. E. L. Saldin, E. A. Schneidmiller, and M. V. Yurkov, "Coherence properties of the radiation from X-ray free electron laser," Opt. Commun. **281**(5), 1179–1188 (2008).
44. R. Bonifacio, C. Pellegrini, and L. M. Narducci, "Collective instabilities and high-gain regime in a free electron laser," Opt. Commun. **50**(6), 373–378 (1984).
45. R. Bonifacio, L. De Salvo, P. Pierini, *et al.*, "Spectrum, temporal structure, and fluctuations in a high-gain free-electron laser starting from noise," Phys. Rev. Lett. **73**(1), 70–73 (1994).
46. E. A. Schneidmiller and M. V. Yurkov, "Coherence Properties of the Radiation from X-ray Free Electron Lasers," CERN YR School Proc. **1**, 539 (2018).
47. H. P. Freund, S. G. Biedron, and S. V. Milton, "Nonlinear harmonic generation in free-electron lasers," IEEE J. Quantum Electron. **36**(3), 275–281 (2000).
48. C. Gerth, G. Brenner, M. Caselle, *et al.*, "Linear array detector for online diagnostics of spectral distributions at MHz repetition rates," J. Synchrotron Radiat. **26**(5), 1514–1522 (2019).
49. C. von Korff Schmising, F. Willems, S. Sharma, *et al.*, "Element-Specific Magnetization Dynamics of Complex Magnetic Systems Probed by Ultrafast Magneto-Optical Spectroscopy," Appl. Sci. **10**(21), 7580 (2020).
50. D. Mayer, F. Lever, D. Picconi, *et al.*, "Following excited-state chemical shifts in molecular ultrafast x-ray photoelectron spectroscopy," Nat. Commun. **13**(1), 198 (2022).
51. M. M. Bidhendi, G. Goetzke, I. J. Bermudez Macias, *et al.*, "Determination of the XUV Frequency Chirp at the Free-Electron Laser FLASH via THz Streaking and Electron Beam Diagnostics," Photonics **11**(12), 1153 (2024).
52. I. Zagorodnov and M. Dohlus, "Semianalytical modeling of multistage bunch compression with collective effects," Phys. Rev. Spec. Top.–Accel. Beams **14**(1), 014403 (2011).
53. U. FrÜhling, M. Wieland, M. Gensch, *et al.*, "Single-shot terahertz-field-driven X-ray streak camera," Nat. Photonics **3**(9), 523–528 (2009).
54. I. Grguraš, A. R. Maier, C. Behrens, *et al.*, "Ultrafast X-ray pulse characterization at free-electron lasers," Nat. Photonics **6**(12), 852–857 (2012).
55. U. Frühling, "Light-field streaking for FELs," J. Phys. B: At. Mol. Opt. Phys. **44**(24), 243001 (2011).
56. R. Ivanov, I. J. B. Macias, J. Liu, *et al.*, "Single-shot temporal characterization of XUV pulses with duration from ~10 fs to ~350 fs at FLASH," J. Phys. B: At. Mol. Opt. Phys. **53**(18), 184004 (2020).
57. K. Tiedtke, J. Feldhaus, U. Hahn, *et al.*, "Gas detectors for x-ray lasers," J. Appl. Phys. **103**(9), 094511 (2008).
58. M. Braune, J. Buck, M. Kuhlmann, *et al.*, "Non-invasive online wavelength measurements at FLASH2 and present benchmark," J. Synchrotron Radiat. **25**(1), 3–15 (2018).
59. R. Ivanov, J. Liu, G. Brenner, *et al.*, "FLASH free-electron laser single-shot temporal diagnostic: terahertz-field-driven streaking," J. Synchrotron Radiat. **25**(1), 26–31 (2018).
60. A. Azima, J. Bödewadt, O. Becker, *et al.*, "Direct measurement of the pulse duration and frequency chirp of seeded XUV free electron laser pulses," New J. Phys. **20**(1), 013010 (2018).
61. I. J. B. Macias, S. Düsterer, R. Ivanov, *et al.*, "Study of temporal, spectral, arrival time and energy fluctuations of SASE FEL pulses," Opt. Express **29**(7), 10491–10508 (2021).
62. U. Becker and D. A. Shirley, *VUV and Soft X-Ray Photoionization*, Physics of Atoms and Molecules (Springer, 1996), 1st ed.
63. M. Mehrjoo, B. Faatz, G. Paraskaki, *et al.*, *Expected Radiation Properties of the Harmonic Afterburner at FLASH2* (JACOW Publishing, 2019).
64. A. A. Sorokin, Y. Bican, S. Bonfigt, *et al.*, "An X-ray gas monitor for free-electron lasers," J. Synchrotron Radiat. **26**(4), 1092–1100 (2019).
65. P. Finetti, H. Höppner, E. Allaria, *et al.*, "Pulse Duration of Seeded Free-Electron Lasers," Phys. Rev. X **7**(2), 021043 (2017).
66. J. C. Diels and W. Rudolph, *Ultrashort Laser Pulse Phenomena* (Elsevier, Academic Press, 2006).

7 7 0 123 41 2025-03-06 06:03:47

A.5 Single-Shot Temporal Characterization with the Transverse Deflecting Structure PolariX and THz Streaking at FLASH

Single-shot temporal characterization with the transverse deflecting structure PolariX and THz streaking at FLASH

G. Goetzke[1], M. Bidhendi[1], C. Gerth[1], C. Behrens[1], P. Amstutz[2], C. Mai[2], G. Hartmann[3], S. Düsterer[1]

[1]Deutsches Elektronen-Synchrotron DESY, Hamburg, Germany
[2]TU Dortmund, Dortmund, Germany
[3]Helmholtz-Zentrum Berlin für Materialien und Energie GmbH, Berlin, Germany

E-mail: gesa.goetzke@desy.de

Abstract. At the free electron laser FLASH at DESY pulse length measurements can be performed with e.g. THz streaking or an analysis using the PolariX TDS. Since THz streaking examines the XUV pulse directly whereas the PolariX TDS focuses on the energy distribution of the (XUV pulse generating) electron bunch, both techniques are capable of analyzing the same XUV pulse simultaneously. We used a newly installed laser heater to shape the electron bunch and therefore influence the XUV pulse profile and compare the resulting pulse shapes measured by THz streaking and the PolariX TDS. We compare average pulse profiles as well as single-shot examples and discuss the challenges of both types of analysis.

1 Introduction

Free electron lasers (FELs) play an important role across diverse scientific disciplines. Still, experiments benefit significantly from non-destructive online photon diagnostics of the delivered XUV pulses. In particular, determining the pulse duration has proven challenging. Insights into the longitudinal pulse profile can be gained by direct photon-based diagnostics or indirectly by analyzing the energy distribution of the electron bunch after it passed the undulator. For the former a THz streaking method [1, 2] can be applied, where the XUV pulse profile is measured by mapping its temporal structure to the kinetic energy distribution of photoelectrons. The latter can be achieved by using a Polarizable X-Band Transverse Deflection Structure (PolariX TDS) [3, 4], which enables the measurement of the longitudinal phase space of the electron bunch, in combination with a magnet that acts as an energy spectrometer. For the first time at FLASH, reconstructed XUV pulse shapes from both TDS analysis and THz streaking are compared. For this comparison we used a FEL setup delivering double pulses. In addition, we were able to influence the electron distribution with a laser heater [5, 6] in order to suppress the FEL lasing process in some parts of the electron bunch [7, 8].

1.1 Methodology and data analysis

To carry out a photon pulse profile reconstruction utilizing a TDS, the electron bunch energy distribution is compared to the energy distribution without lasing. Comparing the current distributions from lasing-on data and lasing-off references isolates the FEL lasing effects. The difference in the center of mass (COM) or the energy spread (RMS) can be compared [9] in order to reconstruct the XUV pulse shape. Lasing-off references are typically recorded by detuning a corrector magnet upstream of the first undulator, which forces the electron bunch on a path that does not overlap with the photon beam sufficiently to lead to a lasing process. Ideally, this detuning minimally alters the electron path, preserving the initial distribution. In particular the current profile should not change. In reality, the slightly different electron path through the undulators sometimes lead to a different electron distribution and different current profiles. These effects have to be investigated in more detail in the future. For an accurate pulse profile it is required to have a lasing-off reference with a phase space similar to the lasing-on data, aside from the FEL lasing effects. Also, it is critical to correctly match the time and energy axes of the lasing image and the reference. In our work we find the reference the same way as described in reference [10], which uses a hierarchical clustering method (AgglomerativeClustering from sklearn) to group similar electron current profiles and use the Pearson correlation coefficient to identify the best match between lasing-on current profiles and lasing-off group averages. For aligning time axes, one of two methods is usually applied: interpolation of the signal region to a defined number of slices (as in ref. [10]) or overlapping the centers of mass of the electron bunches. Energy axis alignment, affected by jitter and drift, often involves adjusting y-positions so that the integrated XUV pulse profiles match with independent pulse energy measurements using a gas monitor detector (GMD) [11]. We instead set a non-lasing region of the pulse profiles to zero, gaining useful insights from data even when the signal surpasses the fluorescent screen's energy range.

In the THz streaking setup, the FEL XUV pulse ionizes a noble gas target leading to a photoelectron distribution with the same temporal shape. When the ionization region is superimposed with the electric field of a THz pulse, the temporal structure of the XUV pulse is mapped into kinetic energies of the photoelectrons, as long as the electron bunch is significantly shorter than the period length of the Terahertz field [1, 2]. The electron kinetic energy distribution is recorded by electron time-of-flight (eTOF) detectors. The setup used was installed at the beamline FL21 and is described in detail in the reference [12]. Depending on the time window of interest, we used different ramps of the THz streaking field. Here we can choose between a large time window with low temporal resolution of a short window with better resolution. Extracting the correct pulse shape with this method can be challenging; however, a complete absence of a photoelectron signal during a specific time window unambiguously indicates that no XUV pulse was present at that time.

1.2 Comparison of pulse profiles from THz streaking and TDS analysis

We compare XUV pulse profiles from three different FEL setups. Here, we focus on comparing the reconstructed XUV pulse shape, specifically addressing whether one or two XUV pulses are present. Different electron bunch and XUV pulse characteristics are achieved by changing the set undulator wavelength and by modifying the electron bunch with the laser heater. With increasing intensity, the laser heater initially enhances the FEL lasing process by suppressing the accelerator microbunching instabilities. As the intensity increases further, however, it hinders the FEL lasing process by increasing the initial energy spread, a phenomenon also referred to as 'overheating' of the electron bunch [8]. To create distinct temporal features for the comparison, we used a beam setup with a non linear compression to obtain an electron bunch with two current spikes. The TDS images and current profiles of one example each of lasing-on and lasing-off from each of our three setups are depicted in Figure 1. For all three setups, two current spikes are clearly visible, whereas it is important to remember that a high current does not automatically correspond to an XUV pulse, especially for large energy chirps. We collected approximately 3000 lasing-on samples and around 2000 lasing-off samples for each dataset. For all setups the electron beam energy was 965 MeV.

The resulting pulse shapes for the TDS and THz streaking analysis for all three setups are depicted in Figure 2. In setup1 the undulator was set to deliver an XUV wavelength of 11 nm. The laser heater was attenuated just enough to maximize the FEL lasing intensity, resulting in a XUV pulse energy of approximately 140 μJ. The different ratios of the current spikes at 0 fs and 320 fs indicate that (probably due to a too much altered electron trajectory) we do not have well-matched lasing-off references. Com-

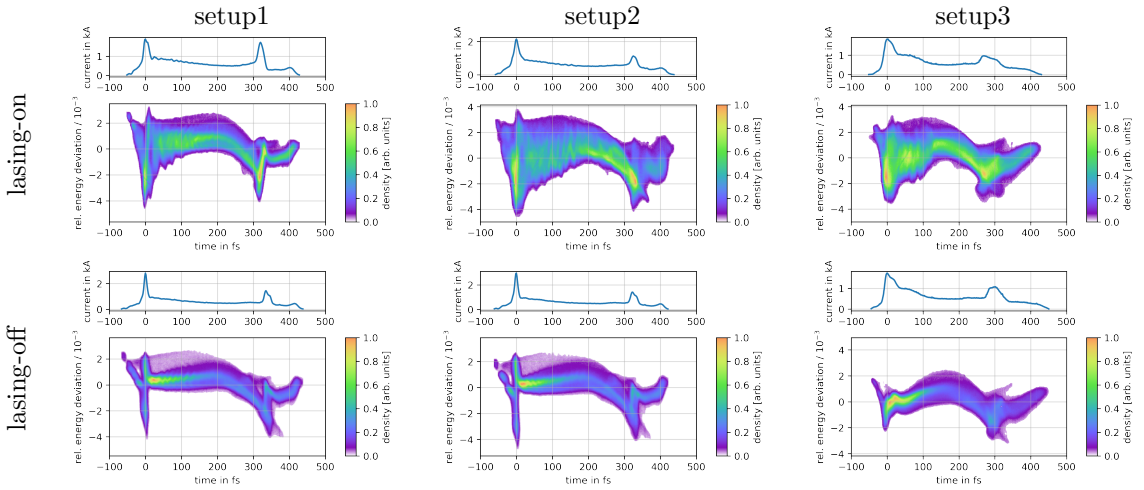

Figure 1: One example of TDS images and their corresponding current profiles of lasing-on and lasing-off for each setup. From setup1 to setup2 we increased the undulator wavelength, from setup2 to setup3 we applied overheating with the laser heater. Each setup clearly shows two current spikes with a time gap of approximately 320 fs. The time zero is defined as the center of the larger current spike, the head of the electron bunch is on the right. All images have individual color-code intensity scales.

parison of the current profiles of the entire lasing-on and lasing-off datasets (not shown here) reveals that the arrival time differences between the two current spikes vary but are, on average, about 20 fs larger for the lasing-off data. In an attempt to account for these effects, we adjust the time axis such that the current spikes overlap rather than simply matching the entire signal region. However, this does not give us a perfect reference, which limits the accuracy of our results. When we compare the COM and RMS profiles of setup1 in Figure 2, which should be identical, we find that the shapes differ significantly around 320 fs (at the position of the second current spike). We even observe a negative signal. This strongly indicates a not matching reference, and problems to reconstruct the shape of this part of the pulse. Here we can compare to the direct measurement of the XUV pulses by THz streaking. Due to the relatively large influence of the eTOF spectrometer instrument function, THz streaking analysis has a limited temporal resolution for reconstructing of the exact pulse shape. However, the fact that no photoelectrons are measured in the region of the second current peak around 320,fs for setup1 (Figure 2 setup1), combined with the ability of THz streaking to detect and resolve such peaks (Figure 2 setup2), provides clear evidence against the existence of a second XUV pulse.

For the next setup (setup2) the undulator wavelength was set to 17 nm (without changing the accelerator settings). Here we obtain a mean FEL pulse energy of $\sim$280 μJ and the lasing-on data of Figure 1 setup2 shows an increased energy spread compared to the lasing-on of setup1. For this setup, the current profiles of lasing-off and lasing-on are in good agreement, and the different matching approaches described above do not lead to different profiles. Both the COM and RMS method indicate the presence of two XUV pulses. In order to cover a time span of approximately 400 fs with THz streaking, a streaking setting with a long THz ramp had to be used. The smaller time window streaking setting used for setup 1 and 3 clearly detects the 2 pulses but due to the short THz ramp lengths the temporal axis is strongly nonlinear. To avoid this artifact we used a longer ramp leading to a much larger influence of the spectrometer resolution as previously reported [13]. Due to the resolution limit we could not determine the rather short pulse duration of the individual pulses with the THz streaking. However, the distances and intensity of both XUV pulses align with the TDS measurements. To enable direct comparison of the XUV pulse shape reconstructed by THz streaking to the TDS measurements, we convoluted the XUV pulse shapes reconstructed from the TDS images with the THz streaking instrument function (namely the photoelectron spectrum without THz streaking field). The convoluted pulse profile obtained from the TDS COM method aligns closely with the predicted pulse profiles from the THz streaking measurements. For the TDS RMS analysis, the pulse intensity of the smaller XUV pulse is underestimated in comparison

to the THz streaking results. Notably, for this setup, where we have a reliable reference, both methods agree with the THz streaking measurements in identifying a second pulse.
In the third setup we aim to eliminate the weaker XUV pulse using the laser heater by setting its intensity to maximum and therefore overheat the electron bunch (setup3). This leads to a reduction of the average XUV pulse energy to around 90 μJ. As we have some TDS reconstructions where parts of the reconstructed pulse profiles are negative, we exclude examples with a minimum of the pulse profiles less than -0.1 GW of the further evaluation. This is again due to a missing reference and excludes about 80% of the dataset obtained from the TDS measurements. The COM and RMS method of the TDS analysis both suggest some minor signal in a second XUV pulse, showing the limitations of the TDS reconstruction for complex electron pulse shapes, but they do not agree or show a distinctly pronounced second peak. In contrast, the THz streaking analysis clearly indicates the absence of a second pulse. This shows that we have succeeded in eliminating the weaker XUV pulse using the laser heater. The wrongly predicted signal of the TDS analysis appears in a region where the electron bunch chirp changes rapidly (at around 320 fs in Figure 1), and we also observe strong variations of low energy electron densities, which results in artifacts in the TDS analysis.

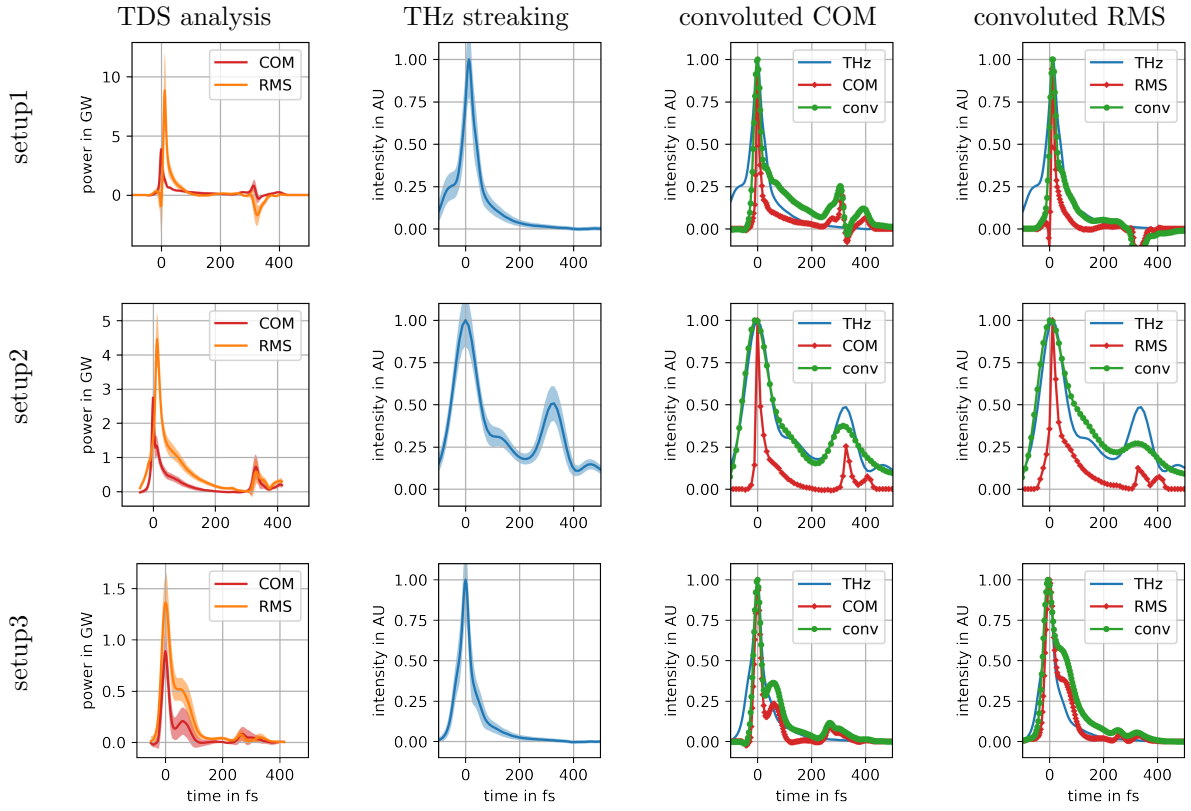

Figure 2: Comparison of XUV pulse shapes from TDS analysis (COM and RMS method) and THz streaking for setups $1-3$. Solid lines are averaged values, shaded areas indicate the standard deviation. The green 'conv' profiles show the respective TDS profiles convoluted with the THz instrument function and hence should ideally agree with the measured THz streaking results. For setup1 COM and RMS profiles differ for the prediction of a second peak around 320 fs, whereas THz steaking results clearly show no photon intensity at this position. For setup2 COM and RMS are in good agreement and all methods predict a second pulse. For setup3 we see different profiles for COM and RMS again, however both indicate that there is no large second pulse. From THz streaking it is clear that no second pulse is present.

1.2.1 Single-shot evaluation

Both methods, TDS analysis and THz streaking can be used for single-shot analysis. Since the PolariX TDS is positioned downstream of the undulator, both methods can evaluate data from the same electron bunch / XUV pulse. For the single-shot pulse profiles, examples illustrating both good and poor agreements are depicted in Figure 3. For profiles of setup2 the relative pulse intensities measured by THz streaking and the TDS reconstruction do not match well in all examples. The TDS COM analysis tends to predict lower intensities for the weaker, pulse (at around 200 fs in Figure 3). However, the TDS analysis remains consistent in predicting a second XUV pulse.
In the TDS profiles from setup3 some individual examples show a second, pronounced pulse. This might be connected to strong fluctuations in electron energies in this region, most likely induced by the laser heater. Since the reference matching algorithm does not specifically focus on this small part of the electron bunch, the assigned reference might not be sufficiently accurate.

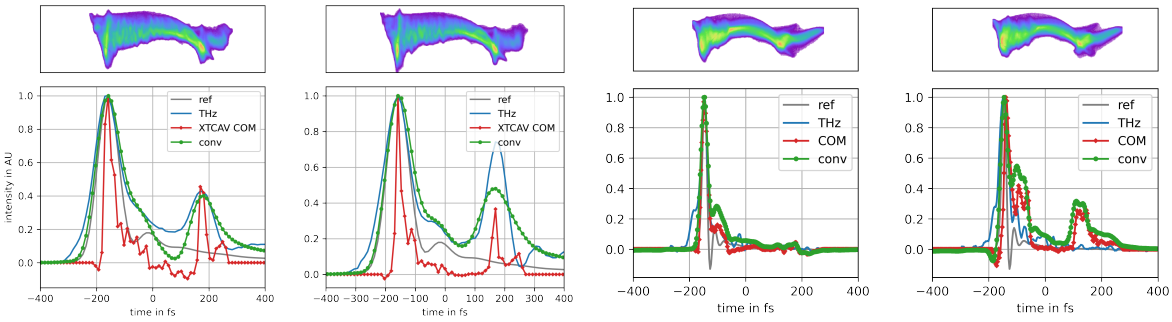

(a) setup2, good agreement

(b) setup2, inaccurate pulse intensity ratio

(c) setup3, good agreement

(d) setup3, additional pulse

Figure 3: Four single-shot examples. Here, time zero is defined as the horizontal center of mass of the TDS image. The THz streaking curves are shifted accordingly. 'ref' is the the photoelectron spectrum without THz streaking field and is convoluted with the TDS profiles to compare both curves with a similar resolution (conv). We see two examples where the methods agree well (a,c), and two where we get an artefact in the analysis (b,d).

1.3 Conclusion

We have compared the results of reconstructed XUV photon pulse profiles obtained with TDS analysis, based on longitudinal phase space measurements of the electron bunch, with pulse profiles obtained by THz streaking, based on photo-ionization by the FEL XUV pulse. Whereas measuring the longitudinal phase space with a TDS is relatively straightforward, obtaining the XUV pulse profiles can be challenging, particularly for complex phase spaces. When the resulting pulse profiles of the center of mass (COM) and root mean square (RMS) TDS analyzing methods align, information regarding the temporal XUV pulse structure can be considered reliable, although small features in the regions of strongly varying energy chirp and/or strong laser heater regions can be falsely predicted. While the TDS analysis provides detailed pulse shape information with high temporal resolution, in the order of few fs, our THz streaking method measures directly the (general) XUV intensity and hence can facilitate interpretation of pulse shape features, especially when discrepancies arise between COM and RMS results. On the other hand, the absence of photoelectrons in a specific time window can clearly confirm that no XUV signal was present during this period. By combining TDS with THz streaking techniques, we have successfully demonstrated that we could utilize the laser heater to shape the electron bunch and effectively suppress one of two XUV pulses.
Monitoring lasing-off current profiles throughout the measurement is crucial for managing drift effects and in order to ensure that the reference method does not alter the electron trajectory too much. In case of strong overheating a single-shot analysis with the TDS might not be sufficiently accurate. Inaccurate second pulse predictions from PolariX TDS for some single-shots highlight the need for careful analysis given the uncertainties inherent in both methods.

1.4 Acknowledgement

We acknowledge DESY (Hamburg, Germany), a member of the Helmholtz Association HGF, for providing the experimental facilities and the financial support necessary to carry out this research. The authors acknowledge the support through the Maxwell computational resources operated at DESY. This work has in part been funded by the IVF project InternLabs-0011 (HIR3X). One of the authors (P. Amstutz) is grateful for financial support by the BMBF under grant No. 05K22PE1. We also want to acknowledge the work of the scientific and technical team at FLASH in particular Mathias Vogt, Juliane Rönsch-Schulenburg and Najmeh Mirian for support during our beamtimes and helpful discussions.

References

[1] Frühling U, Wieland M, Gensch M, Gebert T, Schütte B, Krikunova M, et al. Single-shot terahertz-field-driven X-ray streak camera. Nature Photonics. 2009 Aug;3(9):523-8. Available from: https://doi.org/10.1038/nphoton.2009.160.

[2] Grguraš I, Maier AR, Behrens C, Mazza T, Kelly TJ, Radcliffe P, et al. Ultrafast X-ray pulse characterization at free-electron lasers. Nature Photonics. 2012 Nov;6(12):852-7. Available from: https://doi.org/10.1038/nphoton.2012.276.

[3] Craievich P, Bopp M, Braun HH, Citterio A, Fortunati R, Ganter R, et al. Novel X-band transverse deflection structure with variable polarization. Physical Review Accelerators and Beams. 2020 Nov;23(11). Available from: https://doi.org/10.1103/physrevaccelbeams.23.112001.

[4] Christie F, Rönsch-Schulenburg J, Vogt M. A PolariX TDS for the FLASH2 Beamline. Proceedings of the 39th Free Electron Laser Conference. 2019;FEL2019:Germany. Available from: https://doi.org/10.18429/JACOW-FEL2019-WEP006.

[5] Gerth C, Schöps A, Winkelmann L, Zemella J, Schaper L, Mahnke C, et al. First beam heating with the laser heater for FLASH2020+. JACoW Publishing; 2023. Available from: https://doi.org/10.18429/JACOW-IPAC2023-TUPL098.

[6] Gerth C, Allaria E, Choudhuri A, Schaper L, Schneidmiller E, Schreiber S, et al. Layout of the Laser Heater for FLASH2020+. Proceedings of the 12th International Particle Accelerator Conference. 2021;IPAC2021:Brazil. Available from: https://doi.org/10.18429/JACOW-IPAC2021-TUPAB111.

[7] Marinelli A, Coffee R, Vetter S, Hering P, West GN, Gilevich S, et al. Optical Shaping of X-Ray Free-Electron Lasers. Physical Review Letters. 2016 Jun;116(25):254801. Available from: https://doi.org/10.1103/physrevlett.116.254801.

[8] Amstutz P, Mai C, Mahnke C, Behrens C, Gerth C, Schneidmiller E, et al. Towards short-pulse generation at FLASH via laser-assisted electron bunch manipulation. JACoW Publishing; 2024. Available from: https://doi.org/10.18429/JACOW-IPAC2024-MOPG65.

[9] Behrens C, Decker FJ, Ding Y, Dolgashev VA, Frisch J, Huang Z, et al. Few-femtosecond time-resolved measurements of X-ray free-electron lasers. Nature Communications. 2014 Apr;5(1). Available from: https://doi.org/10.1038/ncomms4762.

[10] SLAC. xtcav processing code;. Available from: https://github.com/slaclab/xtcav2/tree/master.

[11] Sorokin AA, Bican Y, Bonfigt S, Brachmanski M, Braune M, Jastrow UF, et al. An X-ray gas monitor for free-electron lasers. Journal of Synchrotron Radiation. 2019 Jul;26(4):1092-100. Available from: https://doi.org/10.1107/S1600577519005174.

[12] Ivanov R, Bidhendi MM, Macias IJB, Brachmanski M, Kreis S, Bonfigt S, et al. Free-electron laser temporal diagnostic beamline FL21 at FLASH. Opt Express. 2023 Jun;31(12):19146-58. Available from: https://opg.optica.org/oe/abstract.cfm?URI=oe-31-12-19146.

[13] Ivanov R, Bermúdez Macias IJ, Liu J, Brenner G, Roensch-Schulenburg J, Kurdi G, et al. Single-shot temporal characterization of XUV pulses with duration from ∼10 fs to ∼350 fs at FLASH. Journal of Physics B: Atomic, Molecular and Optical Physics. 2020 Jul;53(18):184004. Available from: https://doi.org/10.1088/1361-6455/ab9c38.

Bibliography

[1] J. M. J. Madey, "Stimulated Emission of Bremsstrahlung in a Periodic Magnetic Field," *Journal of Applied Physics*, vol. 42, pp. 1906–1913, Apr. 1971.

[2] W. Ackermann *et al.*, "Operation of a free-electron laser from the extreme ultraviolet to the water window," *Nature Photonics*, vol. 1, pp. 336–342, June 2007.

[3] P. Emma *et al.*, "First lasing and operation of an ångstrom-wavelength free-electron laser," *Nature Photonics*, vol. 4, pp. 641–647, Sept. 2010.

[4] T. Shintake *et al.*, "A compact free-electron laser for generating coherent radiation in the extreme ultraviolet region," *Nature Photonics*, vol. 2, pp. 555–559, Sept. 2008.

[5] T. Ishikawa *et al.*, "A compact X-ray free-electron laser emitting in the sub-ångström region," *Nature Photonics*, vol. 6, pp. 540–544, Aug. 2012.

[6] E. Allaria *et al.*, "Highly coherent and stable pulses from the FERMI seeded free-electron laser in the extreme ultraviolet," *Nature Photonics*, vol. 6, pp. 699–704, Oct. 2012.

[7] M. Altarelli, "The European X-ray free-electron laser facility in Hamburg," *Nuclear Instruments and Methods in Physics Research Section B: Beam Interactions with Materials and Atoms*, vol. 269, pp. 2845–2849, Dec. 2011.

[8] B. D. Patterson *et al.*, "Coherent science at the SwissFEL x-ray laser," *New Journal of Physics*, vol. 12, p. 035012, Mar. 2010.

[9] H.-S. Kang *et al.*, "Hard X-ray free-electron laser with femtosecond-scale timing jitter," *Nature Photonics*, vol. 11, pp. 708–713, Nov. 2017.

[10] J.-D. Fan *et al.*, "First commissioning results of the coherent scattering and imaging endstation at the Shanghai soft X-ray free-electron laser facility," *Nuclear Science and Techniques*, vol. 33, pp. 1–11, Sept. 2022.

[11] L. Young *et al.*, "Femtosecond electronic response of atoms to ultra-intense X-rays," *Nature*, vol. 466, pp. 56–61, July 2010.

[12] B. Rudek *et al.*, "Ultra-efficient ionization of heavy atoms by intense X-ray free-electron laser pulses," *Nature Photonics*, vol. 6, pp. 858–865, Dec. 2012.

[13] M. Hoener *et al.*, "Ultraintense X-Ray Induced Ionization, Dissociation, and Frustrated Absorption in Molecular Nitrogen," *Physical Review Letters*, vol. 104, p. 253002, June 2010.

[14] L. Fang *et al.*, "Multiphoton Ionization as a clock to Reveal Molecular Dynamics with Intense Short X-ray Free Electron Laser Pulses," *Physical Review Letters*, vol. 109, p. 263001, Dec. 2012.

[15] N. Berrah *et al.*, "Multiphoton ionization and fragmentation of molecules with the LCLS X-ray FEL," *Journal of Electron Spectroscopy and Related Phenomena*, vol. 196, pp. 34–37, Oct. 2014.

[16] S. Schorb *et al.*, "Size-Dependent Ultrafast Ionization Dynamics of Nanoscale Samples in Intense Femtosecond X-Ray Free-Electron-Laser Pulses," *Physical Review Letters*, vol. 108, p. 233401, June 2012.

[17] H. Thomas *et al.*, "Explosions of Xenon Clusters in Ultraintense Femtosecond X-Ray Pulses from the LCLS Free Electron Laser," *Physical Review Letters*, vol. 108, p. 133401, Mar. 2012.

[18] T. Gorkhover *et al.*, "Nanoplasma Dynamics of Single Large Xenon Clusters Irradiated with Superintense X-Ray Pulses from the Linac Coherent Light Source Free-Electron Laser," *Physical Review Letters*, vol. 108, p. 245005, June 2012.

[19] J. Carnis *et al.*, "Demonstration of Feasibility of X-Ray Free Electron Laser Studies of Dynamics of Nanoparticles in Entangled Polymer Melts," *Scientific Reports*, vol. 4, pp. 1–8, Aug. 2014.

[20] V. Richardson *et al.*, "Two-Photon Inner-Shell Ionization in the Extreme Ultraviolet," *Physical Review Letters*, vol. 105, p. 013001, June 2010.

[21] M. Meyer *et al.*, "Two-Photon Excitation and Relaxation of the $3d-4d$ Resonance in Atomic Kr," *Physical Review Letters*, vol. 104, p. 213001, May 2010.

[22] A. Barty *et al.*, "Molecular Imaging Using X-Ray Free-Electron Lasers," *Annual Review of Physical Chemistry*, pp. 415–435, Apr. 2013.

[23] L. Wenthaus *et al.*, "Insights into the laser-assisted photoelectric effect from solid-state surfaces," *Phys. Rev. B*, vol. 110, p. 235406, Dec 2024.

[24] L. Giannessi, "FERMI: the first externally seeded Free Electron Laser in the extreme ultraviolet and soft X-ray spectral regions," *Optica Publishing Group*, p. EM4B.1, Mar. 2018.

[25] J. Feldhaus *et al.*, "Possible application of X-ray optical elements for reducing the spectral bandwidth of an X-ray SASE FEL," *Optics Communications*, vol. 140, pp. 341–352, Aug. 1997.

[26] C. Pellegrini *et al.*, "X-ray free-electron lasers—principles, properties and applications," *Nuclear Instruments and Methods in Physics Research Section A: Accelerators, Spectrometers, Detectors and Associated Equipment*, vol. 500, pp. 33–40, Mar. 2003.

[27] S. Krinsky *et al.*, "Analysis of statistical correlations and intensity spiking in the self-amplified spontaneous-emission free-electron laser," *Physical Review Special Topics - Accelerators and Beams*, vol. 6, p. 050701, May 2003.

[28] S. Düsterer *et al.*, "Development of experimental techniques for the characterization of ultrashort photon pulses of extreme ultraviolet free-electron lasers," *Physical Review Special Topics - Accelerators and Beams*, vol. 17, p. 120702, Dec. 2014.

[29] V. A. Dolgashev *et al.*, "Design and application of multimegawatt X-band deflectors for femtosecond electron beam diagnostics," *Physical Review Special Topics - Accelerators and Beams*, vol. 17, p. 102801, Oct. 2014.

[30] P. Craievich *et al.*, "Novel X-band transverse deflection structure with variable polarization," *Physical Review Accelerators and Beams*, vol. 23, p. 112001, Nov. 2020.

[31] S. Casalbuoni *et al.*, "Ultrabroadband terahertz source and beamline based on coherent transition radiation," *Physical Review Special Topics - Accelerators and Beams*, vol. 12, p. 030705, Mar. 2009.

[32] S. Wesch *et al.*, "A multi-channel THz and infrared spectrometer for femtosecond electron bunch diagnostics by single-shot spectroscopy of coherent radiation," *Nuclear Instruments and Methods in Physics Research Section A: Accelerators, Spectrometers, Detectors and Associated Equipment*, vol. 665, pp. 40–47, Feb. 2011.

[33] G. L. Orlandi, "Absolute and non-invasive determination of the electron bunch length in a free electron laser using a bunch compressor monitor," *Scientific Reports*, vol. 14, pp. 1–14, Mar. 2024.

[34] R. Mitzner *et al.*, "Direct autocorrelation of soft-x-ray free-electron-laser pulses by time-resolved two-photon double ionization of He," *Physical Review A*, vol. 80, p. 025402, Aug. 2009.

[35] Y. H. Jiang *et al.*, "Temporal coherence effects in multiple ionization of N_2 via XUV pump-probe autocorrelation," *Physical Review A*, vol. 82, p. 041403, Oct. 2010.

[36] C. Gahl *et al.*, "A femtosecond X-ray/optical cross-correlator," *Nature Photonics*, vol. 2, pp. 165–169, Mar. 2008.

[37] M. Beye *et al.*, "X-ray pulse preserving single-shot optical cross-correlation method for improved experimental temporal resolution," *Applied Physics Letters*, vol. 100, p. 121108, Mar. 2012.

[38] O. Krupin *et al.*, "Temporal cross-correlation of x-ray free electron and optical lasers using soft x-ray pulse induced transient reflectivity," *Optics Express*, vol. 20, pp. 11396–11406, May 2012.

[39] U. Frühling *et al.*, "Single-shot terahertz-field-driven X-ray streak camera," *Nature Photonics*, vol. 3, pp. 523–528, Sept. 2009.

[40] U. Frühling, "Light-field streaking for FELs," *Journal of Physics B: Atomic, Molecular and Optical Physics*, vol. 44, p. 243001, Nov. 2011.

[41] B. Schütte *et al.*, "Electron wave packet sampling with laser-generated extreme ultraviolet and terahertz fields," *Optics Express*, vol. 19, pp. 18833–18841, Sept. 2011.

[42] N. Hartmann *et al.*, "Attosecond time–energy structure of x-ray free-electron laser pulses," *Nature Photonics*, vol. 12, p. 215–220, Mar 2018.

[43] R. Heider *et al.*, "Megahertz-compatible angular streaking with few-femtosecond resolution at x-ray free-electron lasers," *Phys. Rev. A*, vol. 100, p. 053420, Nov 2019.

[44] I. Grguraš *et al.*, "Ultrafast x-ray pulse characterization at free-electron lasers," *Nature Photonics*, vol. 6, p. 852–857, Nov 2012.

[45] P. Schmüser *et al.*, "Ultraviolet and Soft X-Ray Free-Electron Lasers," Berlin, Germany: Springer, 2009.

[46] E. J. Jaeschke *et al.*, "Synchrotron Light Sources and Free-Electron Lasers," Cham, Switzerland: Springer International Publishing, 2020.

[47] Z. Huang *et al.*, "Review of x-ray free-electron laser theory," *Physical Review Special Topics - Accelerators and Beams*, vol. 10, p. 034801, Mar. 2007.

[48] E. L. Saldin, E. A. Schneidmiller, and M. V. Yurkov, "The Physics of Free Electron Lasers," Berlin, Germany: Springer, 2000.

[49] P. Schmüser *et al.*, "Free-Electron Lasers in the Ultraviolet and X-Ray Regime," Cham, Switzerland: Springer International Publishing, 2014.

[50] W. A. Barletta *et al.*, "Free electron lasers: Present status and future challenges," *Nuclear Instruments and Methods in Physics Research Section A: Accelerators, Spectrometers, Detectors and Associated Equipment*, vol. 618, pp. 69–96, June 2010.

[51] R. Bonifacio, L. De Salvo, P. Pierini, N. Piovella, and C. Pellegrini, "Spectrum, temporal structure, and fluctuations in a high-gain free-electron laser starting from noise," *Physical Review Letters*, vol. 73, pp. 70–73, July 1994.

[52] E. L. Saldin *et al.*, "Statistical properties of radiation from VUV and X-ray free electron laser," *Optics Communications*, vol. 148, pp. 383–403, Mar. 1998.

[53] E. L. Saldin, E. A. Schneidmiller, and M. V. Yurkov, "Coherence properties of the radiation from X-ray free electron laser," *Opt. Commun.*, vol. 281, pp. 1179–1188, Mar. 2008.

[54] E. Schneidmiller and M. Yurkov, "Application of Statistical Methods for Measurements of the Coherence Properties of the Radiation from SASE FEL," JACOW, Geneva, Switzerland, June 2016.

[55] H. P. Freund, S. G. Biedron, and S. V. Milton, "Nonlinear harmonic generation in free-electron lasers," *IEEE J. Quantum Electron.*, vol. 36, pp. 275–281, Mar. 2000.

[56] Z. Huang *et al.*, "Three-dimensional analysis of harmonic generation in high-gain free-electron lasers," *Physical Review E*, vol. 62, pp. 7295–7308, Nov. 2000.

[57] E. L. Saldin, E. A. Schneidmiller, and M. V. Yurkov, "Scheme for attophysics experiments at a X-ray SASE FEL," *Optics Communications*, vol. 212, pp. 377–390, Nov. 2002.

[58] E. L. Saldin, E. A. Schneidmiller, and M. V. Yurkov, "Properties of the third harmonic of the radiation from self-amplified spontaneous emission free electron laser," *Phys. Rev. Spec. Top. Accel. Beams*, vol. 9, p. 030702, Mar. 2006.

[59] G. Geloni *et al.*, "Exact solution for second harmonic generation in XFELs," *Opt. Commun.*, vol. 271, pp. 207–218, Mar. 2007.

[60] D. Ratner *et al.*, "Second and third harmonic measurements at the linac coherent light source," *Phys. Rev. Spec. Top. Accel. Beams*, vol. 14, p. 060701, June 2011.

[61] E. L. Saldin *et al.*, "FAST: a three-dimensional time-dependent FEL simulation code," *Nuclear Instruments and Methods in Physics Research Section A: Accelerators, Spectrometers, Detectors and Associated Equipment*, vol. 429, pp. 233–237, June 1999.

[62] R. Ivanov *et al.*, "FLASH free-electron laser single-shot temporal diagnostic: terahertz-field-driven streaking," *Journal of Synchrotron Radiation*, vol. 25, pp. 26–31, Jan. 2018.

[63] R. Ivanov *et al.*, "Single-shot temporal characterization of XUV pulses with duration from ∼10 fs to ∼350 fs at FLASH," *J. Phys. B: At. Mol. Opt. Phys.*, vol. 53, p. 184004, July 2020.

[64] M. Drescher *et al.*, "X-ray Pulses Approaching the Attosecond Frontier," *Science*, vol. 291, pp. 1923–1927, Feb. 2001.

[65] E. Goulielmakis *et al.*, "Direct Measurement of Light Waves," *Science*, vol. 305, pp. 1267–1269, Aug. 2004.

[66] J. Itatani *et al.*, "Attosecond Streak Camera," *Physical Review Letters*, vol. 88, p. 173903, Apr. 2002.

[67] R. Kienberger *et al.*, "Single sub-fs soft-X-ray pulses: generation and measurement with the atomic transient recorder," *Journal of Modern Optics*, Jan. 2005.

[68] T. Oelze *et al.*, "THz streak camera performance for single-shot characterization of XUV pulses with complex temporal structures," *Opt. Express*, vol. 28, pp. 20686–20703, July 2020.

[69] A. Azima *et al.*, "Direct measurement of the pulse duration and frequency chirp of seeded XUV free electron laser pulses," *New Journal of Physics*, vol. 20, p. 013010, Jan. 2018.

[70] I. Robinson *et al.*, "Focus on X-ray Beams with High Coherence," *New Journal of Physics*, vol. 12, p. 035002, Mar. 2010.

[71] A. Bharti and N. Goyal, "Fundamental of synchrotron radiations," in *Synchrotron Radiation* (D. Joseph, ed.), ch. 2, Rijeka: IntechOpen, 2019.

[72] B. Faatz *et al.*, "Simultaneous operation of two soft x-ray free-electron lasers driven by one linear accelerator," *New Journal of Physics*, vol. 18, p. 062002, June 2016.

[73] J. Rönsch-Schulenburg *et al.*, "Experience with Multi-Beam and Multi-Beamline FEL-Operation," *Journal of Physics: Conference Series*, vol. 874, p. 012023, July 2017.

[74] M. Vogt *et al.*, "Status of the Soft X-ray Free Electron Laser FLASH," JACOW, Geneva, Switzerland, June 2015.

[75] M. Scholz, B. Faatz, S. Schreiber, and J. Zemella, "First Simultaneous Operation of Two Sase Beamlines in FLASH," in *Proc. FEL'15*, pp. 297–300, JACoW Publishing, Geneva, Switzerland.

[76] S. Schreiber *et al.*, *Update on the Lifetime of Cs2Te Photocathodes Operated at FLASH.*
JACOW, Geneva, Switzerland, Feb. 2018.

[77] J. Wei *et al.*, "Transverse diagnostics based on dipole mode signal fitting method in TESLA-type accelerating cavities at the free-electron laser FLASH," *Physical Review Accelerators and Beams*, vol. 22, p. 082804, Aug. 2019.

[78] B. R. Steffen, "Electro-optic methods for longitudinal bunch diagnostics at FLASH." Ph.D. dissertation, Universität Hamburg, July 2007.

[79] E. Plönjes *et al.*, "FLASH2: Operation, beamlines, and photon diagnostics," *AIP Conference Proceedings*, vol. 1741, July 2016.

[80] S. Schreiber and B. Faatz, "First Lasing at FLASH2," in *Proc. FEL'14*, pp. 7–8, JACoW Publishing, Geneva, Switzerland.

[81] K. Honkavaara *et al.*, "FLASH: First Soft X-ray FEL Operating Two Undulator Beamlines Simultaneously," in *Proc. FEL'14*, pp. 635–639, JACoW Publishing, Geneva, Switzerland.

[82] J. Rönsch-Schulenburg *et al.*, "FLASH - Status and Upgrades," JACOW Publishing, Geneva, Switzerland, Nov. 2019.

[83] R. Ivanov *et al.*, "Free-electron laser temporal diagnostic beamline FL21 at FLASH," *Optics Express*, vol. 31, pp. 19146–19158, June 2023.

[84] J. Hebling *et al.*, "Velocity matching by pulse front tilting for large-area THz-pulse generation," *Optics Express*, vol. 10, pp. 1161–1166, Oct. 2002.

[85] K. Ravi *et al.*, "Theory of terahertz generation by optical rectification using tilted-pulse-fronts," *Optics Express*, vol. 23, pp. 5253–5276, Feb. 2015.

[86] I. J. B. Macias, "Free electron laser pulse characterization by thz streaking." Ph.D. dissertation, Universität Hamburg, 2022.

[87] F. Christie, J. Rönsch-Schulenburg, and M. Vogt, "A PolariX TDS for the FLASH2 Beamline," in *Proc. FEL'19*, no. 39 in Free Electron Laser Conference, pp. 328–331, JACoW Publishing, Geneva, Switzerland, nov 2019.

[88] C. Behrens *et al.*, "Few-femtosecond time-resolved measurements of X-ray free-electron lasers," *Nature Communications*, vol. 5, pp. 1–7, Apr. 2014.

[89] A. Angelovski *et al.*, "Evaluation of the cone-shaped pickup performance for low charge sub-10 fs arrival-time measurements at free electron laser facilities,"

Physical Review Special Topics - Accelerators and Beams, vol. 18, p. 012801, Jan. 2015.

[90] M. Dreimann *et al.*, "The soft X-ray and XUV split-and-delay unit at beamlines FL23/24 at FLASH2," *Journal of Synchrotron Radiation*, vol. 30, pp. 479–489, Mar. 2023.

[91] M. Kuhlmann *et al.*, "FLASH2 photon diagnostics and beamline concepts," in *Proceedings Volume 8778, Advances in X-ray Free-Electron Lasers II: Instrumentation*, vol. 8778, pp. 180–185, SPIE, May 2013.

[92] C. Gerth *et al.*, "Layout of the Laser Heater for FLASH^{22}," in *Proc. IPAC'21*, no. 12 in International Particle Accelerator Conference, pp. 1647–1650, JACoW Publishing, Geneva, Switzerland, 08 2021.

[93] C. Gerth *et al.*, "First beam heating with the laser heater for flash2020+," in *Proc. IPAC'23*, no. 14 in IPAC'23 - 14th International Particle Accelerator Conference, pp. 1950–1953, JACoW Publishing, Geneva, Switzerland, 05 2023.

[94] T. Ding *et al.*, "Measuring the frequency chirp of extreme-ultraviolet free-electron laser pulses by transient absorption spectroscopy," *Nature Communications*, vol. 12, pp. 1–7, Jan. 2021.

[95] T. Ding *et al.*, "XUV pump–XUV probe transient absorption spectroscopy at FELs," *Faraday Discussions*, vol. 228, no. 0, pp. 519–536, 2021.

[96] C. Dejoie *et al.*, "Using a non-monochromatic microbeam for serial snapshot crystallography," *Journal of Applied Crystallography*, vol. 46, pp. 791–794, June 2013.

[97] A. H. Zewail, "Femtochemistry. Past, present, and future," *Pure and Applied Chemistry*, vol. 72, pp. 2219–2231, Jan. 2000.

[98] T. Brixner *et al.*, "Quantum Control of Gas-Phase and Liquid-Phase Femtochemistry," *ChemPhysChem*, vol. 4, pp. 418–438, May 2003.

[99] M. Gühr *et al.*, "Controlling vibrational wave packet revivals in condensed phase: Dispersion and coherence for Br2 in solid Ar," *Physical Chemistry Chemical Physics*, vol. 6, pp. 5353–5361, Nov. 2004.

[100] F. Richter *et al.*, "Strong-field quantum control in the extreme ultraviolet domain using pulse shaping," *Nature*, vol. 636, pp. 337–341, Dec. 2024.

[101] M. Yan, "Online diagnostics of time-resolved electron beam parameters with femtosecond resolution for x-ray fels."
Ph.D. dissertation, Universität Hamburg, 2015.

[102] Z. Huang and K.-J. Kim, "Nonlinear harmonic generation of coherent amplification and self-amplified spontaneous emission," *Nucl. Instrum. Methods Phys. Res., Sect. A*, vol. 475, pp. 112–117, Dec. 2001.

Acknowledgement

I want to start by saying a big thank you to everyone who supported me along the way. First, I sincerely thank my supervisor, Stefan Düsterer, for his invaluable guidance, and unwavering support throughout my doctoral studies and the writing of this thesis. His expertise, insights, and dedication have shaped this work and greatly contributed to my growth as a researcher. I'm also very grateful to Kai Tiedtke for his support and leadership, which helped create a positive environment for this work. A special thank you goes to my university supervisor, Ulrike Früling, for her essential guidance and helpful feedback. I also appreciate Tim Laarmann for agreeing to review my thesis.

I want to thank all the wonderful colleagues at DESY, especially the FLASH team, for creating such a supportive and inspiring environment. I'm particularly thankful to Gesa Goetzke for proofreading this thesis and for her patience in listening to my "broken" German every day. I also thank Amir Kotobi, Valerija Music and Masoud Mehrjoo for their friendship and valuable insights. I also want to thank Jan Schunk, Simon Marotzke, Dennis Mayer, Rosen Ivanov, Nikolay Kabachnik, Jia Liu, Ivette Bermudez and the many other colleagues for their help and support along the way.

I am especially thankful to Mikhail Yurkov for sharing his profound knowledge of FEL physics and for explaining complex concepts in an engaging way that deepened my understanding. I also want to acknowledge the incredible accelerator physicists in the FLASH control room, especially Evgeny Schneidmiller, whose expert tuning of the machine ensured smooth operations and allowed us to carry out our measurements reliably.

Last but not least, I want to thank my mom and dad, even from far away, your love, patience, and endless support kept me going through it all. To my sister, my lifelong partner in crime—your unconditional support has been a constant source of strength and joy. And most importantly, I want to thank my better half, Niusha. Your endless patience and unwavering support made all the difference. I am forever grateful to have you by my side.

Eidesstattliche Versicherung

Hiermit versichere ich an Eides statt, die vorliegende Dissertationsschrift selbst verfasst und keine anderen als die angegebenen Hilfsmittel und Quellen benutzt zu haben.

Sofern im Zuge der Erstellung der vorliegenden Dissertationsschrift generative K¨unstliche Intelligenz (gKI) basierte elektronische Hilfsmittel verwendet wurden, versichere ich, dass meine eigene Leistung im Vordergrund stand und dass eine vollst¨andige Dokumentation aller verwendeten Hilfsmittel gem¨aß der Guten wissenschaftlichen Praxis vorliegt. Ich trage die Verantwortung f¨ur eventuell durch die gKI generierte fehlerhafte oder verzerrte Inhalte, fehlerhafte Referenzen, Verst¨oße gegen das Datenschutz- und Urheberrecht oder Plagiate.

Datum

Unterschrift des Doktoranden